

ARTICLE

Received 27 Nov 2012 | Accepted 8 Mar 2013 | Published 16 Apr 2013

DOI: 10.1038/ncomms2727

Dynamic switching of calmodulin interactions underlies Ca^{2+} regulation of $\text{Ca}_v1.3$ channels

Manu Ben Johny¹, Philemon S. Yang¹, Hojjat Bazzazi¹ & David T. Yue^{1,2}

Calmodulin regulation of Ca_v channels is a prominent Ca^{2+} feedback mechanism orchestrating vital adjustments of Ca^{2+} entry. The long-held structural correlation of this regulation has been Ca^{2+} -bound calmodulin, complexed alone with an IQ domain on the channel carboxy terminus. Here, however, systematic alanine mutagenesis of the entire carboxyl tail of an L-type $\text{Ca}_v1.3$ channel casts doubt on this paradigm. To identify the actual molecular states underlying channel regulation, we develop a structure-function approach relating the strength of regulation to the affinity of underlying calmodulin/channel interactions, by a Langmuir relation (individually transformed Langmuir analysis). Accordingly, we uncover frank exchange of Ca^{2+} -calmodulin to interfaces beyond the IQ domain, initiating substantial rearrangements of the calmodulin/channel complex. The N-lobe of Ca^{2+} -calmodulin binds an N-terminal spatial Ca^{2+} transforming element module on the channel amino terminus, whereas the C-lobe binds an EF-hand region upstream of the IQ domain. This system of structural plasticity furnishes a next-generation blueprint for Ca_v channel modulation.

¹ Calcium Signals Laboratory, Department of Biomedical Engineering, The Johns Hopkins University School of Medicine, Ross Building, Room 713, 720 Rutland Avenue, Baltimore, Maryland 21205, USA. ² Department of Neuroscience, The Johns Hopkins University School of Medicine, Ross Building, Room 713, 720 Rutland Avenue, Baltimore, Maryland 21205, USA. Correspondence and requests for materials should be addressed to D.T.Y. (email: dyue@jhmi.edu).

Calmodulin (CaM) regulation of the $\text{Ca}_v1\text{-}2$ family of Ca^{2+} channels ranks among the most consequential of biological Ca^{2+} decoding systems^{1,2}. In this regulation, the Ca^{2+} -free form of CaM (apoCaM) already pre-associates with channels³⁻⁵, ready for ensuing Ca^{2+} -driven modulation of channel opening. Upon elevation, intracellular Ca^{2+} binds to this indwelling CaM, driving conformational changes that enhance opening in some channels⁶⁻⁸ (positive-feedback ‘facilitation’) and inhibit opening in others^{9,10} (negative-feedback ‘inactivation’). Intriguingly, Ca^{2+} binding to the individual carboxy- and amino-terminal lobes of CaM can semiautonomously induce distinct components of channel regulation^{7,9,11}, where the C-lobe responds well to Ca^{2+} entering through the channel on which the corresponding CaM resides (‘local Ca^{2+} selectivity’), and the N-lobe may, in some channels, require the far weaker Ca^{2+} signal from distant Ca^{2+} sources^{6,7,12-14} (‘global Ca^{2+} selectivity’). Such Ca^{2+} -feedback regulation influences many biological functions^{1,15-17} and furnishes mechanistic lessons for Ca^{2+} decoding¹⁴. Indeed, CaM regulation of L-type ($\text{Ca}_v1.2$) channels strongly influences cardiac electrical stability^{15,18}, and pharmacological manipulation of such regulation looms as a future antiarrhythmic strategy^{18,19}.

Crucial for understanding and manipulating this CaM regulatory system is the identification of the conformations that underlie such Ca^{2+} modulation. Figure 1a summarizes the

currently accepted conceptual framework, with specific reference to L-type $\text{Ca}_v1.3$ channels for concreteness. Configuration *E* (‘empty’ of CaM) represents channels lacking preassociated apoCaM. Such channels can open normally, but do not exhibit Ca^{2+} /CaM-dependent inactivation (CDI) over the typical ~ 300 ms duration of channel-activity measurements²⁰. Over this period, Ca^{2+} /CaM from the bulk solution cannot appreciably access a channel in configuration *E* to produce CDI²⁰⁻²³. ApoCaM preassociation with configuration *E* yields channels in configuration *A*, where opening can also proceed normally, but subsequent CDI can now ensue. *A* thereby denotes channels that are ‘active’ and capable of CDI. Switching between configurations *E* and *A* occurs slowly (>10 s of seconds²⁴), and almost exclusively involves apoCaM, because typical experiments only briefly activate Ca^{2+} channels every 20–30 s. Thus, there is negligible exchange with configuration *E* during typical measurements of current. Regarding CDI, Ca^{2+} binding to both lobes of CaM yields configuration I_{CN} (both C- and N-lobes of CaM engaged towards CDI), corresponding to a fully inactivated channel with strongly reduced opening^{2,25}. As for intermediate configurations^{7,9,11,14,26}, Ca^{2+} binding only to the C-lobe induces configuration I_C , representing a C-lobe inactivated channel with reduced opening; Ca^{2+} binding only to the N-lobe yields an analogous N-lobe-inactivated configuration (I_N), also with reduced opening. Subsequent entry into configuration I_{CN}

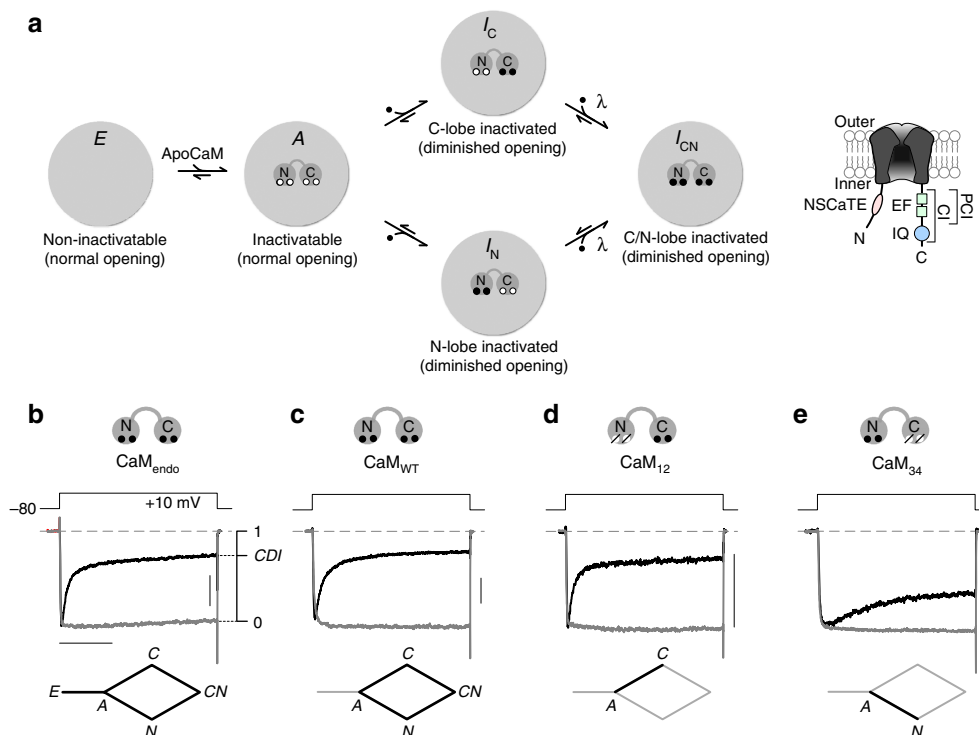


Figure 1 | General schema for CaM regulation of representative L-type $\text{Ca}_v1.3$ channels. (a) Primary configurations of CaM/channel complex with respect to CaM-regulatory phenomena (*E*, *A*, I_C , I_N and I_{CN}). Inset at far right, cartoon of main channel landmarks involved in CaM regulation, with only the pore-forming α_1D subunit of $\text{Ca}_v1.3$ diagrammed. Ca^{2+} -inactivation (CI) region, in the proximal channel C terminus (~ 160 amino acids (aa)), contains elements potentially involved in CaM regulation. IQ domain (IQ), comprising the C-terminal ~ 30 aa of the CI segment, long proposed as preeminent for CaM/channel binding. Dual vestigial EF-hand (EF) motifs span the proximal ~ 100 aa of the CI module; these have been proposed to play a transduction role in channel regulation. Proximal CI (PCI) region constitutes the CI element exclusive of the IQ domain. NSCaTE on channel N terminus of $\text{Ca}_v1.2\text{-}1.3$ channels may be the N-lobe Ca^{2+} /CaM effector site. (b) Whole-cell $\text{Ca}_v1.3$ currents expressed in HEK293 cell, demonstrating CDI in the presence of endogenous CaM only. CDI observed here can reflect properties of the entire system diagrammed in **a**, as schematized by the stick-figure diagram at the bottom of **b**. Here and throughout, the vertical scale bar pertains to 0.2 nA of Ca^{2+} current (black); and the Ba^{2+} current (gray) has been scaled ~ 3 -fold downward to aid comparison of decay kinetics, here and throughout. Horizontal scale bar, 100 ms. (c) Currents during overexpression of CaM_{WT} , isolating the behaviour of the diamond-shaped subsystem at bottom. (d) Currents during overexpression of CaM_{12} , isolating C-lobe form of CDI. (e) Currents during overexpression of CaM_{34} , isolating N-lobe form of CDI. (c–e) Vertical bar, 0.2 nA Ca^{2+} current. Timebase as in **b**.

likely involves cooperative interactions denoted by a λ symbol. Overall, CDI reflects redistribution from configuration A into I_C , I_N and I_{CN} . Of note, we exclude cases where one Ca^{2+} binds a lobe of CaM, because binding within lobes is highly cooperative²⁷. Moreover, only one CaM is included, based on multiple lines of evidence^{22,23}.

The structural basis of this conceptual foundation is less certain, but has been dominated by an IQ-centric hypothesis, where an IQ domain, present on the C termini of all Ca_V1-2 channels² (Fig. 1a, far right, blue circle), serves as the dominant CaM-binding locus on the channel. By this hypothesis, not only does this element comprise much of the preassociation surface for apoCaM^{4,5,20} (Fig. 1a, configuration A), it also constitutes the primary effector site^{2,5,7,9,10,25,28} for $\text{Ca}^{2+}/\text{CaM}$ rebinding to induce Ca^{2+} regulation (for example, Fig. 1a, I_{CN}). The predominance of the IQ-centric paradigm² has prompted resolution of several crystal structures of $\text{Ca}^{2+}/\text{CaM}$ complexed with IQ-domain peptides of various Ca_V1-2 channels²⁹⁻³².

Nonetheless, certain findings fit poorly with this viewpoint. First, crystal structures of $\text{Ca}^{2+}/\text{CaM}$ complexed with wild-type (WT) and mutant IQ peptides of $\text{Ca}_V1.2$ indicate that a signature isoleucine in the IQ element is deeply buried within the C-lobe of $\text{Ca}^{2+}/\text{CaM}$, and that alanine substitution at this isoleucine negligibly perturbs structure³⁰. Moreover, $\text{Ca}^{2+}/\text{CaM}$ affinities for analogous WT and mutant IQ peptides are nearly identical²⁸. How then does alanine substitution at this well-encapsulated locus influence the rest of the channel to strongly disrupt functional regulation³⁰? Second, in $\text{Ca}_V1.2/1.3$ channels we have demonstrated that the effector interface for the N-lobe of $\text{Ca}^{2+}/\text{CaM}$ resides within an N-terminal spatial Ca^{2+} transforming element (NSCaTE) element of the channel N terminus^{13,14,33} (Fig. 1a, far right), separate from the IQ element. Third, analysis of the atomic structure of $\text{Ca}^{2+}/\text{CaM}$ bound to an IQ peptide of $\text{Ca}_V2.1$ channels hints that the C-lobe effector site also resides somewhere outside the IQ module³¹. In all, the long disconnect between challenges like these and IQ-centric theory represents a critical impasse in the field.

A major concern with prior IQ-domain analyses is that function was mostly characterized with only endogenous CaM present^{5,10,25,28,31}. This regime is problematic, as IQ-domain mutations could alter CaM regulation via perturbations at multiple steps within Fig. 1a, whereas interpretations mainly ascribe effects to altered $\text{Ca}^{2+}/\text{CaM}$ binding with an IQ effector site. Serious interpretive challenges thus include the following: (1) although the high apoCaM affinity of most WT channels^{4,20} renders configuration E unlikely (Fig. 1a), this may not hold true for mutant channels, just as observed for certain $\text{Ca}_V1.3$ splice variants²⁰. Mutations weakening apoCaM preassociation could thereby reduce CDI by favouring configuration E (Fig. 1a, incapable of CDI), without affecting $\text{Ca}^{2+}/\text{CaM}$ binding. (2) Mutations that do weaken interaction with one lobe of $\text{Ca}^{2+}/\text{CaM}$ may have their functional effects masked by cooperative steps (λ in Fig. 1a).

This study systematically investigates the IQ-centric hypothesis, minimizing the above challenges by focusing on $\text{Ca}_V1.3$ channels, a representative L-type channel whose CDI is particularly robust and separable into distinct C- and N-lobe components^{11,13,14}. These attributes simplify analysis as follows. For orientation, Fig. 1b illustrates the CDI of $\text{Ca}_V1.3$ channels expressed in HEK293 cells, with only endogenous CaM present. Strong CDI is evident from the rapid decay of whole-cell Ca^{2+} current (black trace) compared with the nearly absent decline of Ba^{2+} current (gray trace). As Ba^{2+} binds negligibly to CaM³⁴, the fractional decline of Ca^{2+} versus Ba^{2+} current after 300 ms depolarization quantifies the steady-state extent of CDI (Fig. 1b, right, CDI parameter). The CDI here reflects the operation of the

entire Fig. 1a system, as schematized at the bottom of Fig. 1b. We can formally isolate the diamond-shaped subsystem lacking configuration E (Fig. 1c, bottom), by using mass action and strong overexpression of WT CaM (CaM_{WT}). The resulting CDI (Fig. 1c) is indistinguishable from that with only endogenous CaM present (Fig. 1b), owing to the high apoCaM affinity of WT $\text{Ca}_V1.3$ channels. Full deconstruction of CDI arises upon strong coexpression of channels with a mutant CaM that only allows Ca^{2+} binding to its C-terminal lobe⁹ (Fig. 1d, CaM_{12}). With reference to Fig. 1a, this manoeuvre depopulates configuration E by mass action, and forbids access into configurations I_N and I_{CN} . Thus, the isolated C-lobe component of CDI^{11,14} is resolved (Fig. 1d), with its signature rapid timecourse of current decay. Importantly, this regime avoids interplay with cooperative λ steps in Fig. 1a. Likewise, strongly coexpressing mutant CaM exhibiting Ca^{2+} binding to its N-lobe alone⁹ (CaM_{34}) isolates the slower N-lobe form of CDI^{11,14} (Fig. 1e), with attendant simplifications. Thus armed, we here exploit selective monitoring of $\text{Ca}_V1.3$ subsystems (Fig. 1b–e), combined with alanine, scanning mutagenesis of the entire carboxyl tail of $\text{Ca}_V1.3$ channels. In doing so, we argue against the IQ-centric paradigm and propose a new framework for the CaM regulation of Ca^{2+} channels.

Results

Individually transformed Langmuir analysis of CaM/channel regulation. Identifying channel effector interfaces for $\text{Ca}^{2+}/\text{CaM}$ is challenging. The main subunit of Ca_V channels alone spans about 2,000 amino acids or more; and peptide assays indicate that $\text{Ca}^{2+}/\text{CaM}$ can bind to multiple segments of uncertain function^{25,35-39}. Even if mutating these segments alters CaM regulation, the observed functional effects could reflect perturbations of apoCaM preassociation, $\text{Ca}^{2+}/\text{CaM}$ binding or transduction. To address these challenges, we initially consider an expanded conceptual layout believed valid for either isolated N- or C-lobe CDI¹⁴ (Fig. 2a), then deduce from this arrangement a simple quantitative analysis to identify *bona fide* effector interfaces. An apoCaM lobe begins prebound to a channel preassociation surface (state 1). Ca^{2+} binding to CaM in this prebound state is considered rare^{14,40}. However, after apoCaM releases (state 2), it may bind Ca^{2+} to produce $\text{Ca}^{2+}/\text{CaM}$ (state 3), or return to state 1. The transiently dissociated lobe of CaM (state 2 or 3) remains within a channel alcove over the usual timescale of CaM regulation (\leq seconds). Finally, $\text{Ca}^{2+}/\text{CaM}$ binds a channel effector site (state 4, square pocket), ultimately inducing regulation via transduction to state 5. Emergent behaviours of this scheme rationalize local and global Ca^{2+} selectivities, as argued previously¹⁴.

Despite the multiple transitions present even for this reduced CDI subsystem (Fig. 2a, left schematics), a straightforward relationship emerges that will aid detection of $\text{Ca}^{2+}/\text{CaM}$ interfaces on the channel, as follows. Suppose we can introduce point alanine mutations into the channel that selectively perturb the $\text{Ca}^{2+}/\text{CaM}$ -binding equilibrium association constant γ_1 (Fig. 2a). Moreover, suppose we can measure $\text{Ca}^{2+}/\text{CaM}$ binding to a corresponding channel peptide, and the affiliated association constant $K_{a,\text{EFF}}$ is proportional to γ_1 in the channel. It then turns out that our metric of inactivation (CDI in Fig. 1b) will always be given by the Langmuir function

$$CDI = CDI_{\text{max}} \cdot K_{a,\text{EFF}} / (K_{a,\text{EFF}} + \Lambda) \quad (1)$$

where CDI_{max} is the value of CDI if $K_{a,\text{EFF}}$ becomes exceedingly large, and Λ is a constant comprised of other association constants in the layout (Supplementary Note S1). Figure 2b plots this function, where the green symbol marks a hypothetical WT

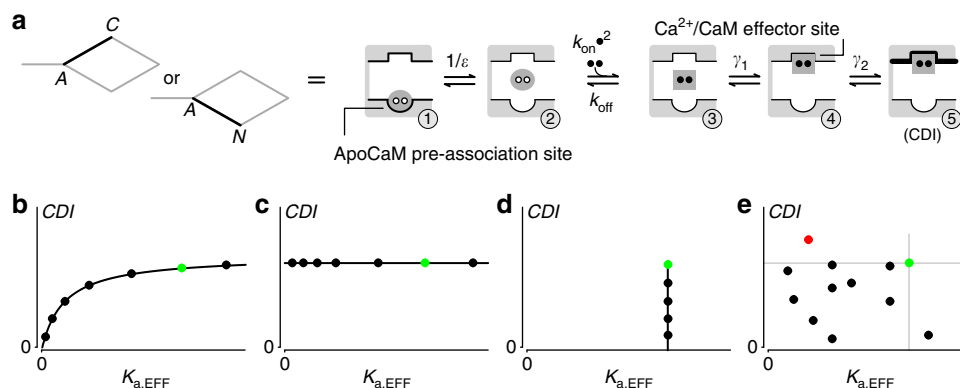


Figure 2 | Probing functionally relevant CaM regulatory interactions via iTL analysis. (a) Isolated C- or N-lobe regulatory system (denoted by stick-figure diagrams on left) can be coarsely represented by a five-state scheme on right. A single lobe of apoCaM begins preassociated to channel (state 1). Following disassociation (state 2), CaM may bind two Ca²⁺ ions (state 3, black dots). Ca²⁺/CaM may subsequently bind to channel effector site (state 4). From here, transduction step leads to state 5, equivalent to CDI. Association constant for lobe of apoCaM binding to preassociation site is ϵ ; whereas γ_1 and γ_2 are association constants for respective transitions from states 3 to 4, and states 4 to 5. (b) Unique Langmuir relation (equation 1) that will emerge upon plotting channel *CDI* (defined Fig. 1b, right) as a function of $K_{a,EFF}$ (association constant measured for isolated channel peptide), if $K_{a,EFF}$ is proportional to one of the actual association constants in the scheme as in a. Black symbols, hypothetical results for various channel/peptide mutations; green symbol, hypothetical WT. (c) Predicted outcome if peptide association constant $K_{a,EFF}$ has no bearing on association constants within holochannels. (d) Outcome if mutations affect holochannel association constants, but not peptide association constants. (e) Outcome if mutations affect holochannel association constant(s) and peptide association constant, but in ways that are poorly correlated.

channel position, and mutations should create data symbols that decorate the remainder of the curve. Importantly, the requirement that peptide $K_{a,EFF}$ need only be proportional to (not equal to) holochannel γ_1 increases the chances that tagged peptides may suffice to correlate with holochannel function. In addition, equation 1 will hold true only if these two suppositions are satisfied (Supplementary Note S2). For example, if mutations alter two transitions within the holochannel, a function with different shape will result. Alternatively, if mutations change the peptide interaction with Ca²⁺/CaM ($K_{a,EFF}$), but not any of the actual association constants within the channel, the outcome in Fig. 2c will emerge. In this case, though the channel peptide can bind Ca²⁺/CaM in isolation, this reaction has no bearing on transitions within the intact holochannel (Fig. 2a). By contrast, Fig. 2d diagrams a scenario where mutations actually do affect transition(s) governing CDI within the holochannel, yet altogether fail to perturb Ca²⁺/CaM binding to a peptide segment of the channel. It is also possible that mutations could affect transition(s) governing CDI within the holochannel, but in ways that are uncorrelated with mutational perturbations of Ca²⁺/CaM binding to a corresponding peptide segment (Fig. 2e). The red symbol denotes a specific subset of this scenario, where a mutation affects transition(s) within the holochannel so as to enhance CDI, whereas the same mutation produces uncorrelated diminution of Ca²⁺/CaM binding to a peptide segment of the channel. Yet other deviations from equation 1 are possible, including those arising from the existence of effector sites beyond our alanine scan (Supplementary Note S3). Importantly, these outcomes will pertain, regardless the size and complexity of the scheme in Fig. 2a (Supplementary Note S4). Because of this generality, we term the analysis individually transformed Langmuir (iTTL) analysis.

Given this insight, we undertook alanine-scanning mutagenesis of Ca_v1.3 channel domains, and screened electrophysiologically for altered CaM regulatory hotspots. In parallel, we introduced hotspot mutations into peptides overlapping scanned regions, and estimated $K_{a,EFF}$ of potential CaM binding. For this purpose, we utilized live-cell fluorescence resonance energy transfer (FRET) two-hybrid assays^{3,4,41}, which have the resolution and throughput

for the task. If such binding truly reflects holochannel function, then *CDI* should vary with $K_{a,EFF}$ as a Langmuir function (equation 1, Fig. 2b). By contrast, if $K_{a,EFF}$ changes in a manner unrelated to holochannel *CDI*, data would diverge from equation 1 (Fig. 2c–e, or otherwise). CaM effector interfaces could thus be systematically resolved.

iTTL analysis of IQ domain as Ca²⁺/CaM effector site. We first addressed whether the Ca_v1.3 IQ domain serves as a Ca²⁺/CaM effector site for CDI, as IQ-centric theory postulates. Single alanines were substituted at each position of the entire IQ domain of Ca_v1.3 channels, whose sequence appears atop Fig. 3a, with the signature isoleucine bolded at position '0'. Naturally occurring alanines were changed to threonine. CDI of these mutants was then characterized for the isolated N- and C-lobe CDI subsystems described above (Fig. 3a,b, left schematics), thus minimizing potential complications from diminished preassociation with apoCaM (Fig. 1a, configuration E), or masking of CDI effects by cooperative λ steps (Fig. 1a). Whereas little deficit in N-lobe CDI was observed (Fig. 3a), the C-lobe CDI was strongly attenuated by alanine substitutions at I[0]A (Fig. 3b, red bar, exemplar traces) and nearby positions (rose). To test for correspondence between reductions in C-lobe CDI and altered Ca²⁺/CaM binding, we performed FRET two-hybrid assays of Ca²⁺/CaM binding to alanine-substituted IQ peptides, with substitutions encompassing sites associated with the strongest CDI effects (Fig. 3b, red and rose bars). Hatched bars denote additional sites chosen at random. The left aspect of Fig. 3c cartoons the FRET interaction partners, and the right portion displays the resulting binding curve for the WT IQ peptide (Fig. 3c, right, black). *FR-1* is proportional to FRET efficiency, as indicated by the efficiency E_A scale bar on the right. D_{free} is the free concentration of donor-tagged molecules (cyan fluorescent protein (CFP)–CaM), where 200 nM is approximately 6,100 D_{free} units^{4,42}. At odds with a Ca²⁺/CaM effector role of the IQ domain, the binding curve for the I[0]A substitution (Fig. 3c, right, red) resembled that for the WT peptide (black), whereas C-lobe CDI was strongly decreased (Fig. 3b). Figure 3c (middle) displays a bar-graph summary of the

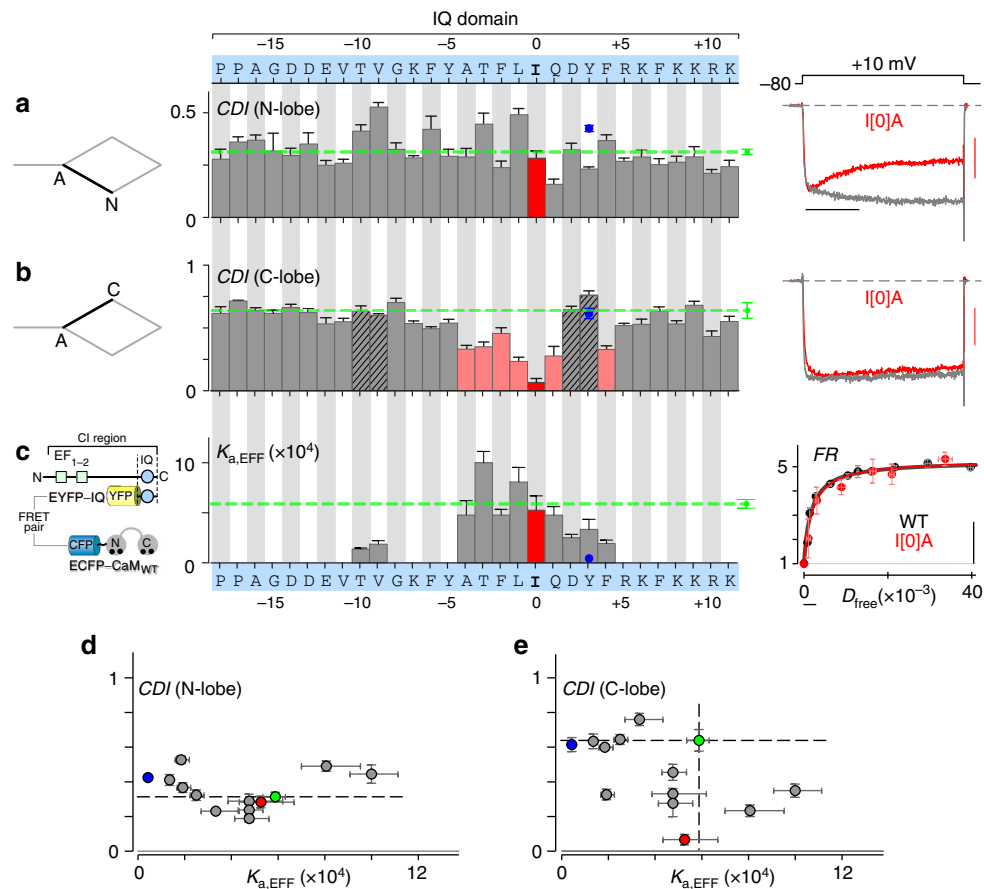


Figure 3 | Inconsistencies with IQ domain role as $\text{Ca}^{2+}/\text{CaM}$ effector site. (a) No appreciable deficit in isolated N-lobe CDI upon point alanine substitutions across the IQ domain (sequence at top with bolded isoleucine at '0' position). Left, corresponding subsystem schematic. Middle, bar-graph summary of CDI metric, as defined in Fig. 1b. Bars, mean \pm s.e.m. for ~ 6 cells each. Green dashed line, WT profile; red bar, I[0]A; blue symbol in all panels, Y[3]D. Right, exemplar currents, demonstrating no change in N-lobe CDI upon I[0]A substitution. Horizontal scale bar, 100 ms; vertical scale bar, 0.2 nA Ca^{2+} current. Red, Ca^{2+} current; gray, Ba^{2+} current. (b) Isolated C-lobe CDI (corresponding subsystem schematized on left) exhibits significant attenuation by mutations surrounding the central isoleucine (coloured bars). Format as in a. I[0]A shows the strongest attenuation (red bar and exemplar currents at right). Bars average ~ 5 cells \pm s.e.m. Dashed green line, WT profile. Timebase as in b; vertical scale bar, 0.2 nA Ca^{2+} current. (c) Bar-graph summary of association constants ($K_{a, \text{EFF}} = 1/K_{d, \text{EFF}}$) for $\text{Ca}^{2+}/\text{CaM}$ binding to IQ, evaluated for constructs exhibiting significant effects in b (coloured bars, with I[0]A in red), or chosen at random (hashed in b). Error bars, non-linear s.d. estimates. FRET partners schematized on the left, and exemplar binding curves on the right for I[0]A (red) and WT (black). Symbols average ~ 7 cells. Smooth curve fits, 1:1 binding model. Calibration to efficiency $E_A = 0.1$, far right vertical scale bar. Horizontal scale bar corresponds to 100 nM. (d) Plots of N-lobe CDI versus $K_{a, \text{EFF}}$ deviate from equation 1, much as in Fig. 2c. Green, WT; red, I[0]A; blue, Y[3]D. (e) Plots of C-lobe CDI versus $K_{a, \text{EFF}}$ also diverge from Langmuir, as in Fig. 1e. This result further argues against the IQ *per se* acting as an effector site for the C-lobe of $\text{Ca}^{2+}/\text{CaM}$. Symbols as in d. (d,e) Y[3]D (blue symbol, CDI mean of four cells) yields poor $\text{Ca}^{2+}/\text{CaM}$ binding, but unchanged CDI. Supplementary Note S7, further FRET data.

resulting association constants ($K_{a, \text{EFF}}$); the WT value is shown as a dashed green line, and that for I[0]A as a red bar (Supplementary Note S5). If the IQ domain were the effector site for the C-lobe of $\text{Ca}^{2+}/\text{CaM}$, C-lobe CDI over various substitutions should correlate with association constants according to equation 1 (Supplementary Notes S1 and S6). However, plots of our data markedly deviate from such a relation (Fig. 3e), much as in Fig. 2e. The green symbol denotes the WT IQ case. Likewise, plots of N-lobe CDI versus $K_{a, \text{EFF}}$ deviated from a Langmuir (Fig. 3d), much as in Fig. 2c. These outcomes fail to support the IQ domain as an effector site for either lobe of $\text{Ca}^{2+}/\text{CaM}$. The actual role of the IQ domain in CDI will be explored later in Fig. 6.

To undertake a still more stringent test, we investigated a Y[3]D construct, based on a prior analogous mutation in $\text{Ca}_v2.1$ that intensely diminished $\text{Ca}^{2+}/\text{CaM}$ affinity³¹. Indeed, the Y[3]D substitution in $\text{Ca}_v1.3$ resulted in a large 13.5-fold decrement in $K_{a, \text{EFF}}$ (Fig. 3c, blue symbol). However, there was no change in C-

or N-lobe CDI (Fig. 3a,b, blue symbols; Supplementary Note S7). These data deviated yet more strongly from a Langmuir (blue symbols, Fig. 3d,e), arguing further against the IQ domain as a $\text{Ca}^{2+}/\text{CaM}$ effector site.

NSCaTE element upheld as effector site for N-lobe of $\text{Ca}^{2+}/\text{CaM}$. Given the absence of a positive outcome for iTL analysis of the IQ domain (that is, Fig. 2b), we turned to the N-terminal NSCaTE module (Fig. 4a, oval), previously proposed as an effector site for N-lobe CDI^{13,14}. For reference, Fig. 4b displays the WT $\text{Ca}_v1.3$ profile for N-lobe CDI. Single alanines were substituted across the NSCaTE module (Fig. 4d, top), at residues that were not originally alanine. The bar-graph summary below (Fig. 4d) indicates strongly diminished N-lobe CDI upon alanine substitution at three residues, previously identified as critical^{13,14} (W[44]A, I[48]A and R[52]A). For comparison, the

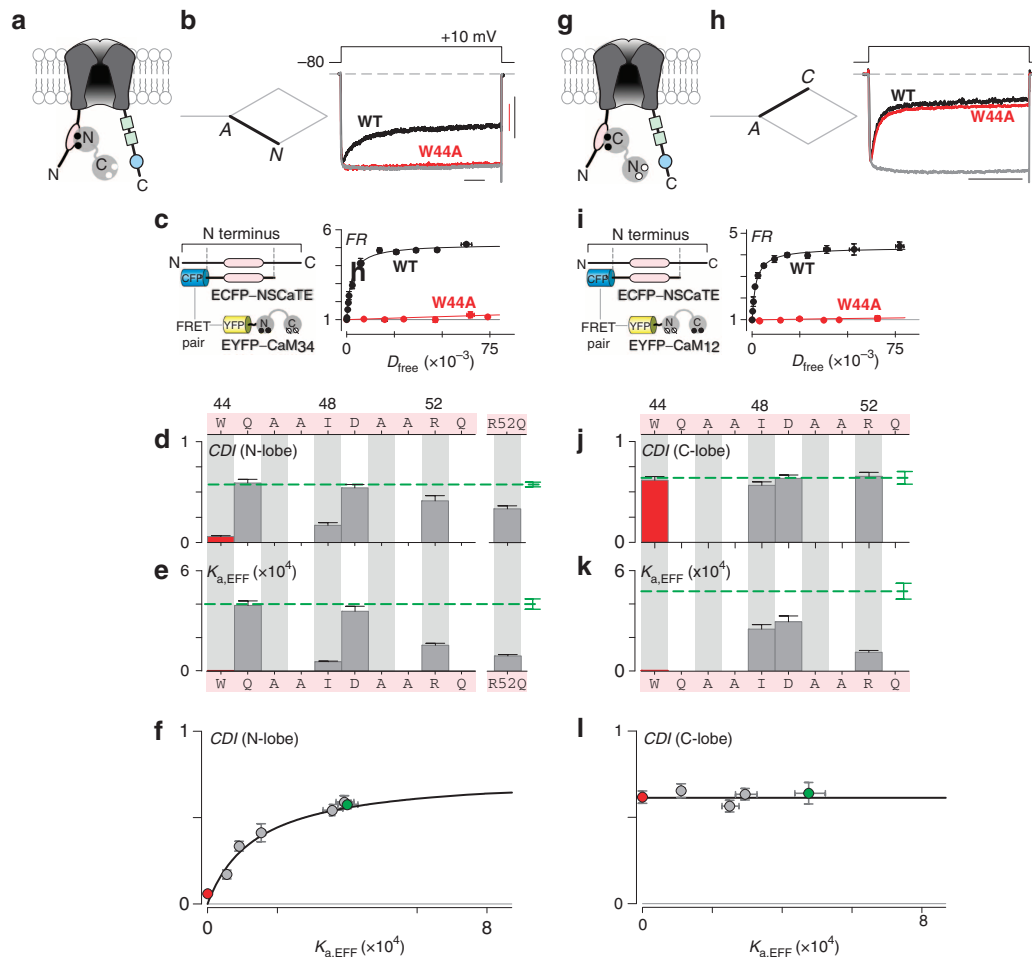


Figure 4 | iTL analysis of Ca^{2+} /CaM effector role of NSCaTE module of $\text{Ca}_v1.3$ channels. (a) Cartoon depicting NSCaTE as putative effector interface for N-lobe of Ca^{2+} /CaM. (b) Exemplar $\text{Ca}_v1.3$ whole-cell currents exhibiting robust isolated N-lobe CDI, as seen from the rapid decay of Ca^{2+} current (black trace). Corresponding stick-figure subsystem appears on the left. W[44]A mutation abolishes N-lobe CDI, as seen from the lack of appreciable Ca^{2+} current decay (red trace). Gray trace, averaged Ba^{2+} trace for WT and W[44]A constructs. Horizontal scale bar, 100 ms; vertical scale bar, 0.2 nA Ca^{2+} current (red, W44A; black, WT). (c) FRET two-hybrid binding curves for Ca^{2+} /CaM₃₄ and NSCaTE segment, with FRET partners schematized on the left. WT pairing in black; W[44]A mutant pairing in red. Each symbol, mean \pm s.e.m. of ~ 5 cells. (d) Bar-graph summary of N-lobe CDI for NSCaTE mutations measured after 800 ms depolarization, with NSCaTE sequence at the top, as numbered by position within $\text{Ca}_v1.3$. Data for W[44]A in red; dashed green line, WT. Bars, mean \pm s.e.m. of ~ 5 cells. (e) Association constants ($K_{a,\text{EFF}} = 1/K_{d,\text{EFF}}$) for Ca^{2+} /CaM₃₄ binding to NSCaTE module evaluated for constructs exhibiting significant effects in panel d. Error bars, non-linear s.d. estimates. Data for W[44]A in red; dashed green line, WT. (f) Plotting N-lobe CDI versus $K_{a,\text{EFF}}$ uncovers a Langmuir, identifying NSCaTE as functionally relevant effector site. W[44]A in red; WT in green. (g–i) iTL fails to uphold NSCaTE as effector site for C-lobe of Ca^{2+} /CaM. Format as in a–f. (h,j) C-lobe CDI at 300 ms, unchanged by NSCaTE mutations. Bars in j, mean \pm s.e.m. of ~ 5 cells. (i,k) Changes in $K_{a,\text{EFF}}$ of NSCaTE module for Ca^{2+} /CaM₁₂ via 3³-FRET. Each symbol in i, mean \pm s.e.m. of ~ 5 cells. (l) C-lobe CDI versus $K_{a,\text{EFF}}$ deviates from Langmuir, as in Fig. 2c.

WT level of CDI is represented by the green dashed line and affiliated error bars. W[44]A featured the strongest CDI decrement, as shown by the Ca^{2+} current (Fig. 4b, red trace) and population data (Fig. 4d, red bar). To pursue iTL analysis, we characterized corresponding binding curves between NSCaTE and Ca^{2+} /CaM₃₄ FRET pairs (Fig. 4c, left; Supplementary Note S8). The WT pairing exhibited a well-resolved binding curve with $K_{a,\text{EFF}} = 4 \times 10^{-4} D_{\text{free}}^{-1}$ units (Fig. 4c, right, black), whereas the W[44]A variant yielded a far lower affinity with $K_{a,\text{EFF}} \sim 0$ (red). A summary of binding affinities is shown for this and additional mutations within NSCaTE in Fig. 4e (Supplementary Note S9), where the dashed green line signifies the WT profile. The crucial test arises by plotting N-lobe CDI as a function of $K_{a,\text{EFF}}$, which resolves the Langmuir relation in Fig. 4f. For reference, WT is shown in green and W[44]A in red. The

particular formulation of equation 1 for this arrangement is given in Supplementary Note S1. Hence, iTL analysis does uphold NSCaTE as a predominate effector site for N-lobe CDI, as argued before by other means^{13,14}. By contrast, analysis of C-lobe CDI (Fig. 4g–k and Supplementary Note S10) reveals deviation from equation 1 (Fig. 4l), much as in Fig. 2c. Thus, NSCaTE mutations have little bearing on C-lobe CDI of the holochannel, though such mutations affect Ca^{2+} /CaM₁₂ binding to an isolated NSCaTE peptide.

Identification of the C-lobe Ca^{2+} /CaM effector interface. Satisfied by proof-of-principle tests of the iTL approach, we turned to identification of the as-yet-unknown effector site for the C-lobe form of CDI. Our screen focused upon the entire carboxy tail of $\text{Ca}_v1.3$ channels upstream of the IQ domain (Fig. 5a,

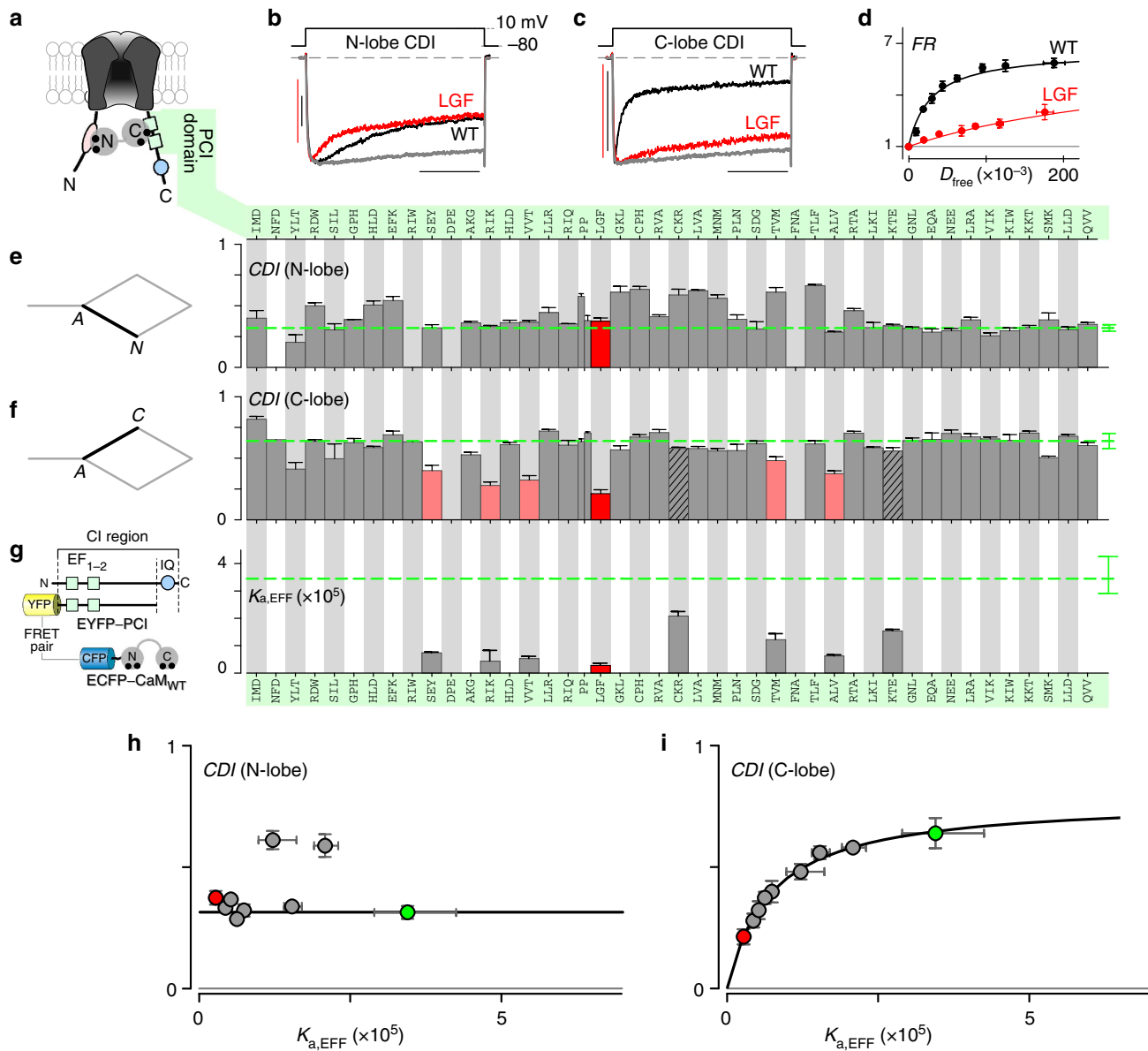


Figure 5 | iTL analysis of PCI segment as C-lobe Ca^{2+} /CaM effector interface. (a) Channel cartoon depicting PCI segment as putative effector site for C-lobe of Ca^{2+} /CaM. (b) Isolated N-lobe CDI for WT and LGF→AAA (LGF) mutant channels. Ca^{2+} current for WT in red, and for LGF in red. Gray, averaged Ba^{2+} trace. Horizontal scale bar, 100 ms; vertical scale bar, 0.2 nA Ca^{2+} current (red, LGF; black, WT). (c) Isolated C-lobe CDI for WT and LGF mutant channels, indicating strong CDI attenuation by LGF mutation. Format as in b. (d) FRET two-hybrid binding curves for Ca^{2+} /CaM pitted against PCI segments, for WT (black) and LGF (red). Each symbol, mean \pm s.e.m. from ~ 9 cells. (e) Bar-graph summary confirming no appreciable reduction of isolated N-lobe CDI, over all alanine scanning mutants across the PCI region (sequence at the top). Schematic of corresponding system under investigation at the left. Green dashed line, WT; red, LGF mutant; gaps, non-expressing configurations. Bars, mean \pm s.e.m. of ~ 5 cells. (f) Bar-graph summary, C-lobe CDI for alanine scan of PCI. Red bar, LGF→AAA mutant showing strong CDI reduction. Rose bar, other loci showing substantial CDI reduction. Hashed, randomly chosen loci for subsequent FRET analysis below. Bars, mean \pm s.e.m. of ~ 5 cells. (e,f) CDI decrease for YLT cluster (Fig. 5e,f) reflects reduced Ca^{2+} entry from 30 mV depolarizing shift in activation, not CDI attenuation *per se*. Shifts for all other loci were at most ± 10 mV (not shown). (g) Association constants for Ca^{2+} /CaM binding to PCI region, with FRET partners as diagrammed on the left. Green dashed line, WT profile. PCI mutations yielding large C-lobe CDI deficits were chosen for FRET analysis (red and rose in f), as well as those chosen at random (hashed in f). Error bars, nonlinear estimates of standard deviation. (h) Plots of N-lobe CDI versus $K_{a,\text{EFF}}$ for Ca^{2+} /CaM binding to PCI deviated from Langmuir. Red, LGF; green, WT. (i) Alternatively, plotting C-lobe CDI revealed Langmuir relation, supporting PCI as C-lobe Ca^{2+} /CaM effector site. Symbols as in h.

proximal Ca^{2+} -inactivation (PCI) domain), because switching these C-terminal segments in chimeric channels sharply influences this type of CDI^{31,43}. For completeness, we initially characterized isolated N-lobe CDI for mutations throughout the PCI and found no appreciable decrement from WT levels (Fig. 5b,e and Supplementary Note S12) as expected. Gaps

indicate non-expressing configurations. By contrast, for isolated C-lobe CDI, the sharp diminution of CDI upon LGF→AAA substitution (Fig. 5c,f, red) exemplifies just one of many newly discovered ‘hotspot’ loci residing in the PCI midsection (Fig. 5f, rose and red; Supplementary Note S12). As a prelude to iTL analysis, we determined the binding of Ca^{2+} /CaM to the PCI

element (Fig. 5g, left cartoon), and indeed the LGF substitution weakens interaction affinity (Fig. 5d). Likewise, binding of the isolated C-lobe of $\text{Ca}^{2+}/\text{CaM}$ to PCI was similarly attenuated by the LGF mutation (Supplementary Note S11), arguing explicitly for disruption of a C-lobe interface. In addition, for loci demonstrating the strongest reduction in C-lobe CDI (Fig. 5f, rose and red), corresponding $\text{Ca}^{2+}/\text{CaM}$ affinities were determined to also attenuate $K_{a,\text{EFF}}$ (Fig. 5g and Supplementary Notes S11 and S12). Importantly, graphing C-lobe CDI versus binding affinity strikingly resolves a Langmuir relation (Fig. 5i), furnishing compelling evidence that the PCI midsection comprises an effector interface for the C-lobe of $\text{Ca}^{2+}/\text{CaM}$. The green symbol corresponds to WT, and the red datum to the LGF mutant. Supplementary Note S1 specifically formulates equation 1 for this case. As expected, plots of N-lobe CDI versus binding affinity deviate from a Langmuir (Fig. 5h), much as in Fig. 2c,e. Overall, the impressive mirror-like inversion of results for NSCaTE (Fig. 4f,l) and PCI (Fig. 5h,i) underscores the considerable ability of iTL analysis to distinguish between effector sites of respective N- and C-lobe CDI.

C-lobe CDI also requires IQ domain interaction with the PCI element. Though the IQ domain alone does not appear to be an effector site for $\text{Ca}^{2+}/\text{CaM}$ (Fig. 3), alanine substitutions in this element nonetheless attenuated the C-lobe CDI^{7,10,11,28,31}, a

result reproduced for reference in Fig. 6a,b. Might the departure of $\text{Ca}^{2+}/\text{CaM}$ to NSCaTE (Fig. 4) and PCI elements (Fig. 5) then allow the IQ domain to rebind elsewhere, in a manner also required for C-lobe CDI? Thus viewed, IQ-domain mutations could diminish C-lobe CDI by weakening this rebinding, but in a way that correlates poorly with IQ-peptide binding to $\text{Ca}^{2+}/\text{CaM}$ in isolation. As C-lobe CDI can be conferred to Ca_v2 channels by substituting PCI and IQ elements from $\text{Ca}_v1^{31,43}$, will the requisite rebinding involve association between these very elements?

Initially disappointing was the existence of only low-affinity binding between IQ and PCI modules (Fig. 6c, left cartoon; Fig. 6d, gray) under conditions of resting intracellular calcium³. By contrast, under elevated Ca^{2+} , robust interaction between the same IQ/PCI FRET pair was observed, with $K_{a,\text{PCI-IQ}} = 4.35 \times 10^{-5} D_{\text{free}} \text{ units}^{-1}$ (Fig. 6d, black). In fact, this Ca^{2+} -dependent interaction accords well with a role in triggering CDI, and likely arises from a requirement for $\text{Ca}^{2+}/\text{CaM}$ to bind the PCI domain before appreciable IQ association occurs (Supplementary Note S13). Beyond mere binding, however, functionally relevant interaction would be decreased by the same IQ-domain mutations that reduced C-lobe CDI. In this regard, IQ peptides bearing I[0]A or Q[1]A substitutions actually demonstrated strong and graded reductions in affinity (Fig. 6e, respective red and blue symbols), coarsely matching observed deficits in C-lobe CDI (Fig. 6b). Figure 6c summarizes the results

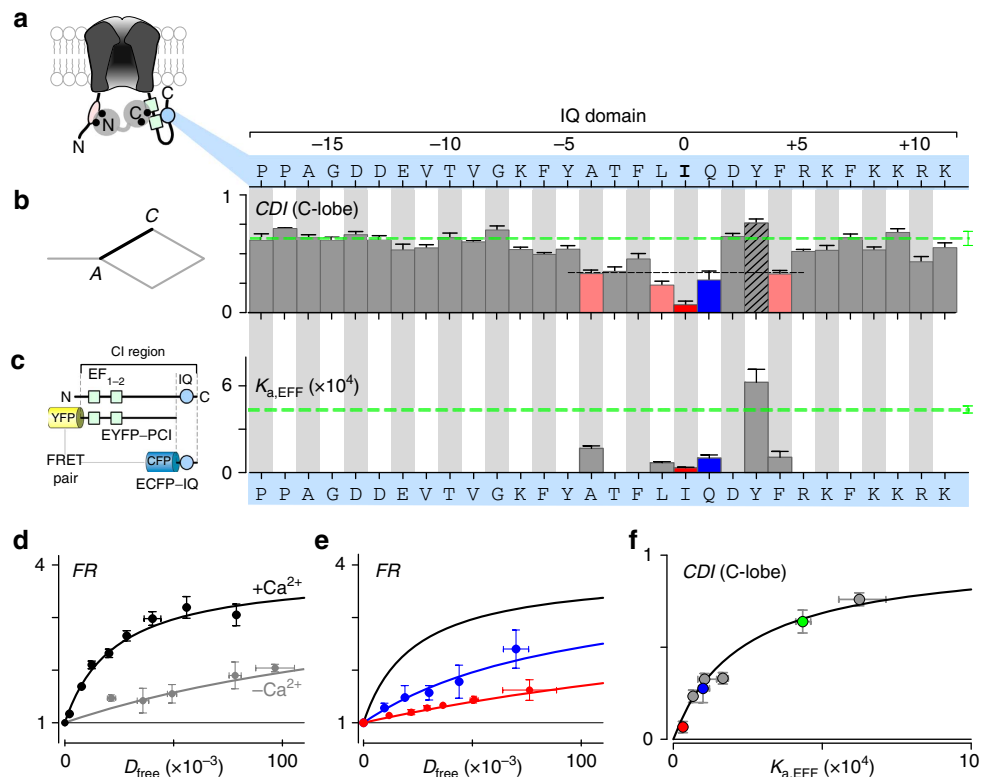


Figure 6 | Role of IQ domain in C-lobe CDI. (a) Cartoon depicting putative binding interaction between IQ domain and PCI segment, which is also required for C-lobe CDI. (b) Bar-graph summary of C-lobe CDI measured for alanine scan of IQ domain, reproduced from Fig. 3b. Strongest CDI reduction for I[0]A mutant (red), followed closely by loci affiliated with rose and blue bars underneath black dashed line. Dashed green line, WT. (c) Association constants $K_{a,\text{EFF}}$ determined for $^3\text{FRET}$ binding between IQ domain and PCI region (partners diagrammed at left), under elevated levels of Ca^{2+} . WT profile, green dashed line. Bars, $K_{a,\text{EFF}}$ for mutants with strongest effects (colored bars in b) or chosen at random (hashed bars in b). Error bars, nonlinear s.d. estimates. (d) Exemplar $^3\text{FRET}$ binding curves for IQ/PCI interaction. Each symbol, mean \pm s.e.m. of ~ 8 cells. Absent Ca^{2+} , the IQ domain associates only weakly with the PCI region (gray). However, elevated Ca^{2+} greatly enhances binding (black). (e) $^3\text{FRET}$ binding curves for I[0]A (red) and Q[1]A (blue) mutations under elevated Ca^{2+} . Each symbol, mean \pm s.e.m. of ~ 5 cells. Fit for WT IQ/PCI interaction reproduced from d in black. (f) Plotting C-lobe CDI versus $K_{a,\text{EFF}}$ under elevated Ca^{2+} unveils a well-resolved Langmuir relation. WT (green), I[0]A (red), and Q[1]A (blue).

of these and other FRET-binding assays (Supplementary Note S14) performed for loci with the strongest effects on C-lobe CDI (Fig. 6b, coloured bars under dashed black threshold). With these data, quantitative iTL analysis could be

undertaken, where the presumed CDI transition in question would be the γ_2 transduction step in Fig. 2a, and the relevant form of equation 1 is specified in Supplementary Note S15. Remarkably, plotting C-lobe CDI (Fig. 6b) versus IQ/PCI-

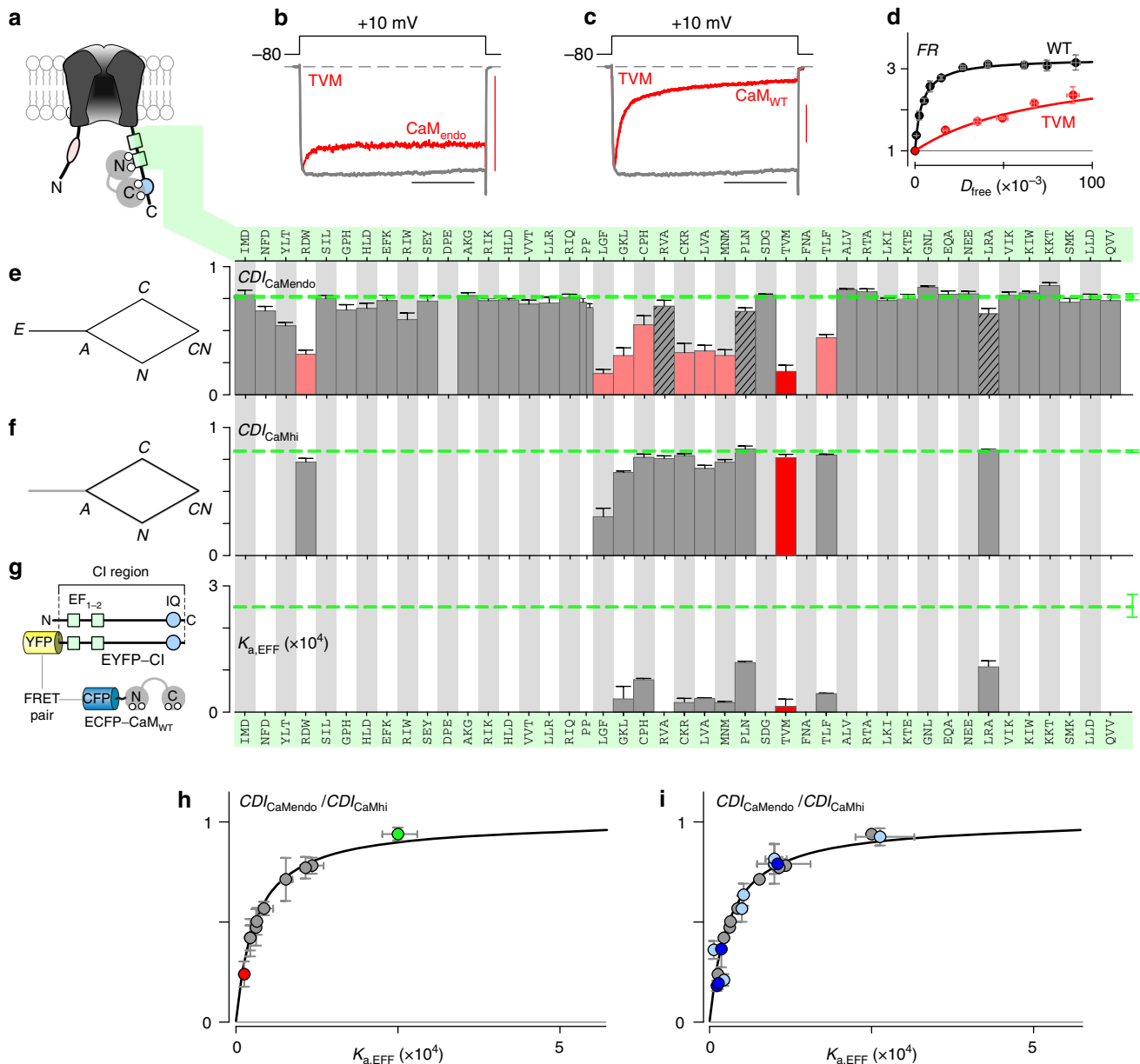


Figure 7 | Footprint of apoCaM preassociation with the PCI segment. (a) Channel cartoon depicting apoCaM preassociated with the CI region, with C-lobe engaging IQ domain, and N-lobe associated with PCI region. (b) Whole-cell currents for TVM→AAA mutant in the PCI segment (Ca^{2+} in red; Ba^{2+} in gray), with only endogenous CaM present. Horizontal scale bar, 100 ms; vertical scale bar, 0.2 nA Ca^{2+} current. (c) Overexpressing CaM_{WT} rescues CDI for TVM→AAA mutation, suggesting that PCI region harbours an apoCaM preassociation locus. Format as in **b**. (d) $^{33}\text{FRET}$ binding curves show strong apoCaM binding to CI region. WT in black; TVM→AAA in red. Each symbol, mean \pm s.e.m. of ~ 7 cells. (e) Bar-graph summary of CDI with only endogenous CaM present ($\text{CDI}_{\text{CaMendo}}$), across alanine scan of PCI region. TVM→AAA (red) shows strongest effect, with rose colored bars also showing appreciable CDI reduction. Bars, mean \pm s.e.m. of ~ 5 cells. Left, schematic of relevant CaM subsystem. (f) Bar-graph summary of CDI rescue upon overexpressing CaM_{WT} ($\text{CDI}_{\text{CaMhi}}$), for mutations showing significant loss of CDI (coloured bars in **e**), or chosen at random (hashed bars in **e**). Bars, mean \pm s.e.m. of ~ 5 cells. Corresponding subsystem of regulation on the left. (g) Bar-graph summary of $K_{a,\text{EFF}}$ for apoCaM binding to CI region, with partners as sketched on the left. Data obtained for nearly all mutants with significant CDI reduction (coloured in **e**), and for some mutants chosen at random (hashed in **e**). Error bars, non-linear estimates of s.d. (h) iTL analysis confirms role of PCI as functionally relevant apoCaM site. Plotting $\text{CDI}_{\text{CaMendo}} / \text{CDI}_{\text{CaMhi}}$ (**e,f**) versus $K_{a,\text{EFF}}$ for apoCaM/CI binding uncovers well-resolved Langmuir relation. TVM→AAA, red; WT, green. (i) Overlaying like data for IQ-domain analysis presented elsewhere⁴² (blue symbols here) displays remarkable agreement, consistent with the same apoCaM binding both PCI and IQ domains. Deep blue symbols, A[-4], I[0], F[+4] hotspots for apoCaM interaction with IQ element.

binding affinity (Fig. 6c) indeed resolves a Langmuir (Fig. 6f). Thus, C-lobe CDI likely requires a tripartite complex of IQ, PCI, and C-lobe $\text{Ca}^{2+}/\text{CaM}$ (Fig. 6a).

ApoCaM preassociation within the PCI domain. Having explored $\text{Ca}^{2+}/\text{CaM}$, we turned to apoCaM interactions. Elsewhere⁴² we have shown that apoCaM preassociates with a surface that at least includes^{2,4,5,20} the IQ element. Furthermore, homology modelling⁴² of a related apoCaM/IQ structure for Na_V channels^{44,45} suggests that the $\text{Ca}_V1.3$ IQ module interacts with the C-lobe of apoCaM. Will the N-lobe of apoCaM then bind the PCI domain (Fig. 7a)? If so, then our earlier PCI mutations could have weakened N-lobe apoCaM interaction, and potentially diminished CDI by favouring configuration *E* channels (Fig. 1a, incapable of inactivation). This effect would not have been apparent thus far, as we invariably overexpressed CaM. However, with only endogenous CaM present in Fig. 7e, CDI reflects the operation of a system that includes configuration *E* (left schematic), and the observed $\text{CDI}_{\text{CaMendo}}$ is indeed strongly attenuated by mutations at many loci (rose and red bars).

We tested for decreased preassociation as the basis of this effect, by checking whether CDI resurged upon strongly overexpressing CaM_{WT} . This manoeuvre should act via mass action to eliminate CaM-less channels²⁰, restrict channels to the subsystem on the left of Fig. 7f and restore CDI. For all loci demonstrating appreciable reduction of $\text{CDI}_{\text{CaMendo}}$ (Fig. 7e, rose and red), CDI was measured under strongly overexpressed CaM_{WT} ($\text{CDI}_{\text{CaMhi}}$), as summarized in Fig. 7f. As the baseline, we confirmed that elevating CaM_{WT} hardly affected CDI of WT channels (compare WT, dashed green lines in Fig. 7e,f). The high apoCaM affinity of WT channels renders configuration *E* channels rare, even with only endogenous apoCaM present²⁰. By contrast, the TVM mutant exhibits an impressive return of CDI upon elevating CaM_{WT} (Fig. 7b,c), as do many other mutants (Fig. 7f and Supplementary Note S16). Critically, scrutiny of the underlying configurations (Fig. 7e,f, left) reveals that $\text{CDI}_{\text{CaMendo}} = \text{CDI}_{\text{CaMhi}} \times F_b$, where F_b is the fraction of channels prebound to apoCaM with only endogenous CaM present. This relation holds true, even with a residual $\text{CDI}_{\text{CaMhi}}$ shortfall compared with WT (for example, Fig. 7f, LGF). This is so, because a $\text{CDI}_{\text{CaMhi}}$ deficit mirrors changes in the diamond subsystem of Fig. 7f (left), which are identically present in $\text{CDI}_{\text{CaMendo}}$ measurements (Fig. 7e).

Thus aware, we tested whether apoCaM binding to the entire CI domain (spanning IQ and PCI modules) mirrors resurgent CDI (Fig. 7g, left cartoon; Supplementary Note S17). The WT pairing showed robust interaction with $K_{a,\text{EFF}} = 2.5 \times 10^{-4} D_{\text{free}}$ units⁻¹ (Fig. 7d, black; Fig. 7g, green dashed line). By contrast, the TVM pairing, corresponding to strong resurgent CDI (Fig. 7b,c), exhibited far weaker affinity (Fig. 7d,g, red; $K_{a,\text{EFF}} = 0.13 \times 10^{-4} D_{\text{free}}$ units⁻¹). Figure 7g tallies the graded decrease of $K_{a,\text{EFF}}$ for these and other pairings (Supplementary Note S16).

Most rigorously, if PCI contacts indeed mediate apoCaM preassociation, then plotting $\text{CDI}_{\text{CaMendo}}/\text{CDI}_{\text{CaMhi}}$ ($= F_b$) versus the $K_{a,\text{EFF}}$ for apoCaM/CI interaction (Fig. 7g) should decorate a Langmuir relation (Supplementary Note S18). Indeed, just such a relation (Fig. 7h) is resolved (Fig. 7e–g), arguing that the N-lobe of apoCaM interfaces with corresponding PCI loci. Notably, this relation is identical to that reported elsewhere for IQ mutations on the same CI module⁴². Figure 7i explicitly overlays PCI and IQ data (in blue), and this striking resolution of a single Langmuir accords with one and the same apoCaM binding PCI and IQ domains.

Discussion

These experiments fundamentally transform the prevailing molecular view of CaM regulation of Ca^{2+} channels. The field has long been dominated by an IQ-centric scheme^{2,5,7,9,10,25,28}, wherein indwelling apoCaM begins preassociated with a C-terminal IQ domain, and remains bound to this element upon CaM interaction with Ca^{2+} . Here our new proposal establishes substantial exchange of CaM to alternate effector loci (Fig. 8a). ApoCaM preassociates with an interface that includes, but is not limited to, the IQ domain (configuration *A*): the C-lobe binds the IQ (cyan circle) and the N-lobe binds the central midsection of the PCI (green box). Ca^{2+} binding to the N-lobe yields configuration I_N , wherein this lobe binds the NSCaTE module on the channel N terminus (pink oval) to trigger the N-lobe CDI. Ensuing Ca^{2+} binding to the C-lobe induces configuration I_{CN} , with C-lobe binding the proximal PCI midsection (green square) and IQ engagement²⁵. If Ca^{2+} only binds the C-lobe, the system adopts configuration I_C , corresponding to C-lobe CDI. Ultimately, $\text{Ca}^{2+}/\text{CaM}$ exchange to effector loci diminishes opening, perhaps via allosteric coupling of carboxy-tail conformation to a contiguous IVS6 segment implicated in activation^{46,47} and inactivation⁴⁸. Only a single CaM is present^{22,23} (Supplementary Note S17).

The structures of many of these configurations are presently unknown, but *ab initio* and homology modelling here confirms the plausibility of these configurations. Concerning the apoCaM/channel complex, Fig. 8b displays a homology model of the C-lobe complexed with the IQ domain⁴² (blue), based on an analogous atomic structure from Na_V channels^{44,45}. Key IQ-domain hotspots for apoCaM preassociation (red) are rationalized by this model⁴². To portray the N-lobe as shown in Fig. 8b, we utilized *ab initio* structural prediction of the CI domain with the *Rosetta* package⁴⁹ (Supplementary Note S19), yielding a PCI domain (green) with two vestigial EF hands, and a protruding helix ('preIQ' subelement). The EF-hand module (EF) resembles the structure of a homologous segment of Na_V channels^{50,51}, and a helical segment has been resolved in atomic structures of analogous $\text{Ca}_V1.2$ segments^{36,37}. Reassuringly, N-lobe apoCaM hotspots adorn the surface of this PCI model (red coloration), within the more C-terminal of the two EF hands. Accordingly, we appose the atomic structure of the N-lobe (1 CFD) to this segment of the PCI model, initially using a shape-complementarity docking algorithm⁵² (*PatchDock*), followed by refinement with docking protocols of *Rosetta* (Supplementary Note S20). Of note, the configuration of the N-lobe explains the outright enhancement of N-lobe CDI by PCI mutations in the region of putative N-lobe contact (compare Figs 5e and 7e, GKL through TLF). Weakening channel binding to the N-lobe (Fig. 2a, state 1) would, through connection to other states, increase state 5 occupancy, thereby boosting N-lobe CDI (Supplementary Note S21). By contrast, no N-lobe CDI enhancement was observed for IQ substitutions at the central isoleucine (I[0]) and downstream⁴², consistent with IQ binding the C-lobe of apoCaM.

Figure 8c displays a model of $\text{Ca}^{2+}/\text{CaM}$ complexed with the channel. The N-lobe bound to NSCaTE is an NMR structure³³, and functional N-lobe CDI hotspots correspond well with intimate contact points (red). C-lobe CDI hotspots also adorn the surface of the upstream EF-hand region of an alternative *ab initio* model of the PCI (Fig. 8c, red; Supplementary Note S19). The IQ domain and atomic structure of the C-lobe of $\text{Ca}^{2+}/\text{CaM}$ (3BXL) were then computationally docked (Supplementary Note S22), yielding a rather canonical CaM/peptide complex where the channel contributes a surrogate lobe of CaM. Overall, this framework promises to set the table for future structural biology and structure–function work.

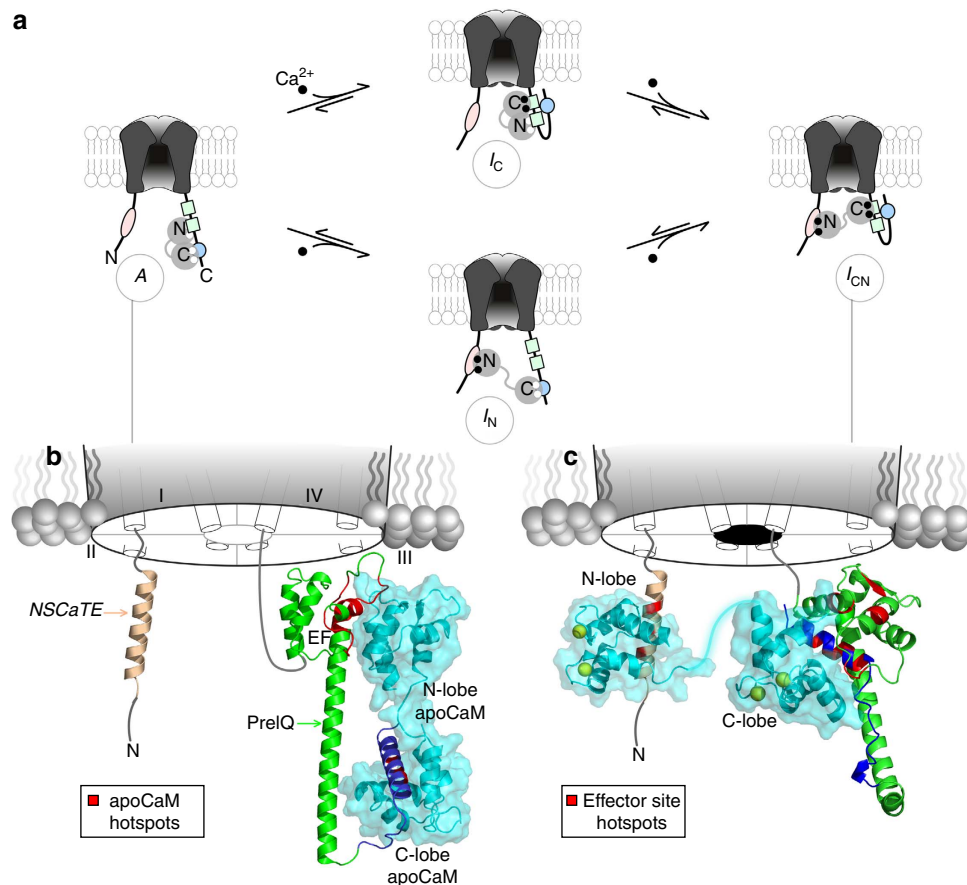


Figure 8 | New view of CaM regulatory configurations of Ca_v1.3 channels. (a) Molecular layout of configurations A, I_C, I_N and I_{CN} for conceptual scheme in Fig. 1a. ApoCaM preassociates with CI region: C-lobe articulates IQ domain, and N-lobe engages the PCI segment. Once Ca²⁺ binds CaM, the N-lobe of Ca²⁺/CaM departs to NSCaTE on channel N terminus, eliciting N-lobe CDI (I_N). Alternatively, the C-lobe of Ca²⁺/CaM migrates to PCI segment, recruiting IQ domain to tripartite complex (I_C). Finally, I_{CN} corresponds to channel that has undergone both N- and C-lobe CDI. (b) *De novo* model of Ca_v1.3 CI region docked to apoCaM (PCI region: green; IQ domain: blue). ApoCaM hotspots (Fig. 6e–g) in red. C-lobe of apoCaM contacts IQ, whereas N-lobe binds EF-hand region. (c) Left, atomic structure of NSCaTE bound to N-lobe of Ca²⁺/CaM (2LQC³³). NSCaTE peptide in tan; and N-lobe Ca²⁺/CaM in cyan. Ca²⁺, yellow. N-lobe CDI hotspots on NSCaTE in red. Right, *de novo* model of tripartite IQ-PCI-Ca²⁺/CaM complex (PCI region, green; IQ domain, blue). C-lobe CDI hotspots in red for both PCI and IQ domains.

More broadly, this regulatory scheme may explain paradoxes and open horizons. First, it has been asked how Ca²⁺/CaM could ever leave the IQ domain, when the binding affinity between these elements is so high^{4,5,29,39,53} (for example, $K_{a/CaM-IQ} = 5.88 \times 10^{-4} D_{free}^{-1}$ units in Fig. 3c). The answer may arise from the competing binding affinity for the tripartite complex (Fig. 8a, I_{CN}), which multivalent ligand binding theory⁵⁴ would approximate as $K_{a/CaM-PCI-IQ} \sim K_{a/CaM-PCI} \times K_{a/PCI-IQ} \times (\text{local concentration of IQ}) = (4.35 \times 10^{-5} D_{free}^{-1} \text{ units}^{-1}) \times (3.45 \times 10^{-5} D_{free}^{-1} \text{ units}^{-1}) \times (1.36 \times 10^8 D_{free} \text{ units}) \sim 0.2 D_{free}^{-1} \text{ units}^{-1}$, a value far larger than $K_{a/CaM-IQ}$ (Supplementary Note S23). Second, our scheme offers new interfaces targetable by native modulators and drug discovery. As L-type channel CDI influences cardiac arrhythmogenic potential^{15,18} and Ca²⁺ load in substantia nigral neurons prone to degeneration in Parkinson's⁵⁵, one could envisage a screen for selective modulators of N- or C-lobe CDI¹⁹. Third, our results offer a fine-grained roadmap for Ca_v1-2 splice/editing variants and channelopathies⁵⁶. Indeed, we suspect that the design principles revealed here may generalize widely to other molecules modulated by CaM^{45,50,51,57}.

Methods

Molecular biology. To simplify mutagenesis, the WT construct in this study was an engineered Ca_v1.3 construct $\alpha_{1D\Delta 1626}$, nearly identical to and derived from the native rat brain variant (α_{1D} , AF3070009). Briefly, the $\alpha_{1D\Delta 1626}$ construct, as contained with mammalian expression plasmid pCDNA6 (Invitrogen), features introduction of a silent and unique *KpnI* site at a position corresponding to ~50 amino acid residues upstream of the C-terminal IQ domain (G₁₅₃₈T₁₅₃₉). As well, a unique *BglIII* restriction site is present at a locus corresponding to ~450 amino acid residues upstream of the IQ domain. Finally, a unique *XbaI* and stop codon have been engineered to occur immediately after the IQ domain. These attributes accelerated construction of cDNAs encoding triple alanine mutations of $\alpha_{1D\Delta 1626}$. Point mutations of channel segments were made via QuikChange mutagenesis (Agilent) before PCR amplification and insertion into the full-length $\alpha_{1D\Delta 1626}$ channel construct via restriction sites *BglIII/KpnI*, *KpnI/XbaI* or *BglIII/XbaI*. Some triple alanine mutation constructs included a seven amino acid extension (SRGPAVRR) after residue 1626. For FRET two-hybrid constructs, fluorophore-tagged (all based on enhanced cyan fluorescent protein (ECFP) and enhanced yellow fluorescent protein (EYFP)) CaM constructs were made as described⁴. Other FRET constructs were made by replacing CaM with appropriate PCR-amplified segments, via unique *NotI* and *XbaI* sites flanking CaM⁴. YFP-CaM_C (Supplementary Fig. S10) was YFP fused to the C-lobe of CaM (residues 78–149). To aid cloning, the YFP-tagged CI region was made with a 12 residue extension (SRGPYSIVSPKC) via *NotI/XbaI* sites as above. This linker did not alter apoCaM binding affinity versus WT YFP-tagged CI region (not shown). Throughout, all segments subject to PCR or QuikChange mutagenesis were verified in their entirety by sequencing.

Transfection of HEK293 cells. For whole-cell patch clamp experiments, HEK293 cells were cultured on 10-cm plates, and channels transiently transfected by a calcium phosphate method⁹. We applied 8 μg of complementary DNA encoding the desired channel α_1 -subunit, along with 8 μg of rat brain β_{2a} (M80545) and 8 μg of rat brain $\alpha_2\delta$ (NM012919.2) subunits. We utilized the β_{2a} auxiliary subunit to minimize voltage-dependent inactivation. For experiments involving CaM overexpression, we coexpressed 8 μg of rat CaM_{WT}, CaM₁₂ or CaM₃₄, as described⁹. All of the above cDNA constructs were included within mammalian expression plasmids with a cytomegalovirus promoter. To boost expression, cDNA for simian virus 40T antigen (1–2 μg) was cotransfected. For FRET two-hybrid experiments, HEK293 cells were cultured on glass-bottom dishes and transfected with FuGENE 6 (Roche) before epifluorescence microscope imaging⁴. Electrophysiology/FRET experiments were performed at room temperature 1–3 days after transfection.

Whole-cell recording. Whole-cell recordings were obtained using an Axopatch 200 A amplifier (Axon Instruments). Electrodes were made from borosilicate glass capillaries (World Precision Instruments, MTW 150-F4) yielding 1–3 M Ω resistances, which were in turn compensated for series resistance by >70%. Currents were low-pass filtered at 2 kHz before digital acquisition at several times that frequency. A P/8 leak-subtraction protocol was used. The internal solution contained (in mM): CsMeSO₃, 114; CsCl, 5; MgCl₂, 1; MgATP, 4; HEPES (pH 7.4), 10; and BAPTA (1,2-bis(*o*-aminophenoxy)ethane-*N,N,N',N'*-tetraacetic acid), 10; at 290 mOsm adjusted with glucose. The bath solution was (in mM): TEA-MeSO₃, 102; HEPES (pH 7.4), 10; CaCl₂ or BaCl₂, 40; at 300 mOsm, adjusted with TEA-MeSO₃.

FRET optical imaging. We conducted FRET two-hybrid experiments in HEK293 cells cultured on glass-bottom dishes, using an inverted fluorescence microscope as extensively described by our laboratory⁴. Experiments utilized a bath Tyrode's solution containing either 2 mM Ca²⁺ for experiments probing apoCaM binding or 10 mM Ca²⁺ with 4 μM ionomycin (Sigma-Aldrich, MO) for elevated Ca²⁺ experiments. The 3³-FRET efficiencies (E_A) were computed as elaborated in our prior publications⁴. E-FRET efficiencies (E_D), whose measurement methodology was developed and refined in other laboratories⁴¹, could be determined from the same single-cell 3³-FRET measurements using the following relationship, which expresses E_D in terms of our own calibration metrics and standard measurements:

$$E_D = E_{D,\text{max}} \cdot D_b = \frac{S_{\text{FRET}} - R_{D1} \cdot S_{\text{CFP}} - R_A \cdot S_{\text{YFP}}}{S_{\text{FRET}} - R_{D1} \cdot S_{\text{CFP}} - R_A \cdot S_{\text{YFP}} + G \cdot S_{\text{CFP}}} \quad (2)$$

where G is a constant, defined as

$$G = R_{D1} \frac{\epsilon_{\text{CFP}}(440 \text{ nm})M_A}{\epsilon_{\text{YFP}}(440 \text{ nm})M_D} \approx 1.864 \quad (3)$$

S_{FRET} , S_{YFP} and S_{CFP} correspond to fluorescent measurements from the same cell using FRET, YFP and CFP cubes, whose spectral properties have been detailed previously⁴. R_{D1} and R_A are constants relating to the respective spectral properties of ECFP and EYFP; $\epsilon_{\text{CFP}}(440 \text{ nm})/\epsilon_{\text{YFP}}(440 \text{ nm})$ approximates the ratio of molar extinction coefficients of ECFP and EYFP at 440 nm, respectively; and M_A/M_D is the ratio of optical gain factors and quantum yields pertaining to EYFP and ECFP, respectively. Detailed descriptions of these parameters and their determination appear in our prior publications⁴. For all FRET efficiencies, spurious FRET relating to unbound ECFP and EYFP moieties has been subtracted¹³. For 3³-FRET, spurious FRET is linearly proportional to the concentration of CFP molecules, and the experimentally determined slope $A_{3^3\text{-FRET}}$ was obtained from cells coexpressing ECFP and EYFP fluorophores. Similarly, for E-FRET, the spurious FRET is linearly proportional to the concentration of EYFP molecules. The slope for this relationship $A_{E\text{-FRET}}$ can be obtained from:

$$A_{E\text{-FRET}} = A_{3^3\text{-FRET}} \cdot (R_A/R_{D1})/(M_A/M_D) \quad (4)$$

The methods for FRET two-hybrid binding curves have been extensively described in previous publications^{3,4,41}. Briefly, binding curves were determined by least-squared error minimization of data from multiple cells, utilizing a 1:1 binding model, with adjustment of parameters $K_{d,\text{EFF}}$ and maximal FRET efficiency at saturating donor concentrations. For a small number of interactions involving mutations that strongly disrupted binding, the maximal FRET efficiency was set equal to that of the corresponding WT interaction and $K_{d,\text{EFF}}$ varied to minimize errors. The s.d. error bounds on $K_{d,\text{EFF}}$ estimates were determined by Jacobian error matrix analysis⁵⁸.

Supplementary Note S24 characterizes our FRET two-hybrid constructs, specifying their precise sequence composition, and behaviour via western blot and confocal imaging analysis.

Molecular modelling. *De novo* structural prediction was performed using the Robetta online server⁴⁹ (<http://robetta.bakerlab.org>) as described in Supplementary Notes S19, S20–S22. We used web-based molecular docking

programs, PatchDock⁵² (<http://bioinfo3d.cs.tau.ac.il/PatchDock/>) and FireDock⁵⁹ (<http://bioinfo3d.cs.tau.ac.il/FireDock/>) to obtain preliminary models for molecular docking. Such preliminary models were subsequently used as starting models for further structural modelling and refinement using a customized docking protocol of PyRosetta⁶⁰. A homology model of the C-lobe of apoCaM bound to IQ domain was constructed as described elsewhere⁴². All molecular models and atomic structures were visualized and rendered using PyMOL v1.2r1. (DeLano Scientific, LLC).

References

- Dunlap, K. Calcium channels are models of self-control. *J. Gen. Physiol.* **129**, 379–383 (2007).
- Halling, D. B., Aracena-Parks, P. & Hamilton, S. L. Regulation of voltage-gated Ca²⁺ channels by calmodulin. *Sci. STKE* **2006**, er1 (2006).
- Erickson, M. G., Alseikhan, B. A., Peterson, B. Z. & Yue, D. T. Preassociation of calmodulin with voltage-gated Ca²⁺ channels revealed by FRET in single living cells. *Neuron* **31**, 973–985 (2001).
- Erickson, M. G., Liang, H., Mori, M. X. & Yue, D. T. FRET two-hybrid mapping reveals function and location of L-type Ca²⁺ channel CaM preassociation. *Neuron* **39**, 97–107 (2003).
- Pitt, G. S. *et al.* Molecular basis of calmodulin tethering and Ca²⁺-dependent inactivation of L-type Ca²⁺ channels. *J. Biol. Chem.* **276**, 30794–30802 (2001).
- Chaudhuri, D., Issa, J. B. & Yue, D. T. Elementary mechanisms producing facilitation of Ca_v2.1 (P/Q-type) channels. *J. Gen. Physiol.* **129**, 385–401 (2007).
- DeMaria, C. D., Soong, T. W., Alseikhan, B. A., Alvania, R. S. & Yue, D. T. Calmodulin bifurcates the local Ca²⁺ signal that modulates P/Q-type Ca²⁺ channels. *Nature* **411**, 484–489 (2001).
- Lee, A. *et al.* Ca²⁺/calmodulin binds to and modulates P/Q-type calcium channels. *Nature* **399**, 155–159 (1999).
- Peterson, B. Z., DeMaria, C. D., Adelman, J. P. & Yue, D. T. Calmodulin is the Ca²⁺ sensor for Ca²⁺-dependent inactivation of L-type calcium channels. *Neuron* **22**, 549–558 (1999).
- Zuhlke, R. D., Pitt, G. S., Deisseroth, K., Tsien, R. W. & Reuter, H. Calmodulin supports both inactivation and facilitation of L-type calcium channels. *Nature* **399**, 159–162 (1999).
- Yang, P. S. *et al.* Switching of Ca²⁺-dependent inactivation of Ca_v1.3 channels by calcium binding proteins of auditory hair cells. *J. Neurosci.* **26**, 10677–10689 (2006).
- Lee, A., Scheuer, T. & Catterall, W. A. Ca²⁺/calmodulin-dependent facilitation and inactivation of P/Q-type Ca²⁺ channels. *J. Neurosci.* **20**, 6830–6838 (2000).
- Dick, I. E. *et al.* A modular switch for spatial Ca²⁺ selectivity in the calmodulin regulation of Ca_v channels. *Nature* **451**, 830–834 (2008).
- Tadross, M. R., Dick, I. E. & Yue, D. T. Mechanism of local and global Ca²⁺ sensing by calmodulin in complex with a Ca²⁺ channel. *Cell* **133**, 1228–1240 (2008).
- Alseikhan, B. A., DeMaria, C. D., Colecraft, H. M. & Yue, D. T. Engineered calmodulins reveal the unexpected eminence of Ca²⁺ channel inactivation in controlling heart excitation. *Proc. Natl Acad. Sci. USA* **99**, 17185–17190 (2002).
- Dolmetsch, R. Excitation-transcription coupling: signaling by ion channels to the nucleus. *Sci. STKE* **2003**, PE4 (2003).
- Evans, R. M. & Zamponi, G. W. Presynaptic Ca²⁺ channels--integration centers for neuronal signaling pathways. *Trends Neurosci.* **29**, 617–624 (2006).
- Mahajan, A. *et al.* Modifying L-type calcium current kinetics: consequences for cardiac excitation and arrhythmia dynamics. *Biophys. J.* **94**, 411–423 (2008).
- Anderson, M. E. & Mohler, P. J. Rescuing a failing heart: think globally, treat locally. *Nat. Med.* **15**, 25–26 (2009).
- Liu, X., Yang, P. S., Yang, W. & Yue, D. T. Enzyme-inhibitor-like tuning of Ca²⁺ channel connectivity with calmodulin. *Nature* **463**, 968–972 (2010).
- Findeisen, F. *et al.* Calmodulin overexpression does not alter Ca_v1.2 function or oligomerization state. *Channels (Austin)* **5**, 320–324 (2011).
- Mori, M. X., Erickson, M. G. & Yue, D. T. Functional stoichiometry and local enrichment of calmodulin interacting with Ca²⁺ channels. *Science* **304**, 432–435 (2004).
- Yang, P. S., Mori, M. X., Antony, E. A., Tadross, M. R. & Yue, D. T. A single calmodulin imparts distinct N- and C-lobe regulatory processes to individual Ca_v1.3 channels (abstr.). *Biophys. J.* **92**, 354a (2007).
- Chaudhuri, D., Alseikhan, B. A., Chang, S. Y., Soong, T. W. & Yue, D. T. Developmental activation of calmodulin-dependent facilitation of cerebellar P-type Ca²⁺ current. *J. Neurosci.* **25**, 8282–8294 (2005).
- Kim, J., Ghosh, S., Nunziato, D. A. & Pitt, G. S. Identification of the components controlling inactivation of voltage-gated Ca²⁺ channels. *Neuron* **41**, 745–754 (2004).
- Lee, A., Zhou, H., Scheuer, T. & Catterall, W. A. Molecular determinants of Ca²⁺/calmodulin-dependent regulation of Ca_v2.1 channels. *Proc. Natl Acad. Sci. USA* **100**, 16059–16064 (2003).

27. Linse, S., Helmersson, A. & Forsen, S. Calcium binding to calmodulin and its globular domains. *J. Biol. Chem.* **266**, 8050–8054 (1991).
28. Zuhlke, R. D., Pitt, G. S., Tsiens, R. W. & Reuter, H. Ca^{2+} -sensitive inactivation and facilitation of L-type Ca^{2+} channels both depend on specific amino acid residues in a consensus calmodulin-binding motif in the alpha 1C subunit. *J. Biol. Chem.* **275**, 21121–21129 (2000).
29. Van Petegem, F., Chatelain, F. C. & Minor, Jr. D. L. Insights into voltage-gated calcium channel regulation from the structure of the $\text{Ca}_v1.2$ IQ domain- Ca^{2+} /calmodulin complex. *Nat. Struct. Mol. Biol.* **12**, 1108–1115 (2005).
30. Fallon, J. L., Halling, D. B., Hamilton, S. L. & Quiocho, F. A. Structure of calmodulin bound to the hydrophobic IQ domain of the cardiac $\text{Ca}_v1.2$ calcium channel. *Structure* **13**, 1881–1886 (2005).
31. Mori, M. X., Vander Kooi, C. W., Leahy, D. J. & Yue, D. T. Crystal structure of the Ca_v2 IQ domain in complex with Ca^{2+} /calmodulin: high-resolution mechanistic implications for channel regulation by Ca^{2+} . *Structure* **16**, 607–620 (2008).
32. Kim, E. Y. *et al.* Structures of Ca_v2 Ca^{2+} /CaM-IQ domain complexes reveal binding modes that underlie calcium-dependent inactivation and facilitation. *Structure* **16**, 1455–1467 (2008).
33. Liu, Z. & Vogel, H. J. Structural basis for the regulation of L-type voltage-gated calcium channels: interactions between the N-terminal cytoplasmic domain and Ca^{2+} -calmodulin. *Front. Mol. Neurosci.* **5**, 38 (2012).
34. Chao, S. H., Suzuki, Y., Zysk, J. R. & Cheung, W. Y. Activation of calmodulin by various metal cations as a function of ionic radius. *Mol. Pharmacol.* **26**, 75–82 (1984).
35. Ivanina, T., Blumenstein, Y., Shistik, E., Barzilai, R. & Dascal, N. Modulation of L-type Ca^{2+} channels by $\text{G}_{\beta\gamma}$ and calmodulin via interactions with N and C termini of α_{1C} . *J. Biol. Chem.* **275**, 39846–39854 (2000).
36. Kim, E. Y. *et al.* Multiple C-terminal tail Ca^{2+} /CaMs regulate $\text{Ca}_v1.2$ function but do not mediate channel dimerization. *EMBO J.* **29**, 3924–3938 (2010).
37. Fallon, J. L. *et al.* Crystal structure of dimeric cardiac L-type calcium channel regulatory domains bridged by Ca^{2+} calmodulins. *Proc. Natl Acad. Sci. USA* **106**, 5135–5140 (2009).
38. Pate, P. *et al.* Determinants for calmodulin binding on voltage-dependent Ca^{2+} channels. *J. Biol. Chem.* **275**, 39786–39792 (2000).
39. Asmara, H., Minobe, E., Saud, Z. A. & Kameyama, M. Interactions of calmodulin with the multiple binding sites of $\text{Ca}_v1.2$ Ca^{2+} channels. *J. Pharmacol. Sci.* **112**, 397–404 (2010).
40. Houdusse, A. *et al.* Crystal structure of apo-calmodulin bound to the first two IQ motifs of myosin V reveals essential recognition features. *Proc. Natl Acad. Sci. USA* **103**, 19326–19331 (2006).
41. Chen, H., Puhl, 3rd H. L., Koushik, S. V., Vogel, S. S. & Ikeda, S. R. Measurement of FRET efficiency and ratio of donor to acceptor concentration in living cells. *Biophys. J.* **91**, L39–L41 (2006).
42. Bazazzi, H. X., Ben Johny, M. & Yue, D. T. Continuously tunable Ca^{2+} regulation of RNA-edited $\text{Ca}_v1.3$ channels *in review* (2013).
43. de Leon, M. *et al.* Essential Ca^{2+} -binding motif for Ca^{2+} -sensitive inactivation of L-type Ca^{2+} channels. *Science* **270**, 1502–1506 (1995).
44. Chagot, B. & Chazin, W. J. Solution NMR structure of Apo-calmodulin in complex with the IQ motif of human cardiac sodium channel $\text{Na}_v1.5$. *J. Mol. Biol.* **406**, 106–119 (2011).
45. Feldkamp, M. D., Yu, L. & Shea, M. A. Structural and energetic determinants of apo calmodulin binding to the IQ motif of the $\text{Na}_v1.2$ voltage-dependent sodium channel. *Structure* **19**, 733–747 (2011).
46. Tadross, M. R., Ben Johny, M. & Yue, D. T. Molecular endpoints of Ca^{2+} /calmodulin- and voltage-dependent inactivation of $\text{Ca}_v1.3$ channels. *J. Gen. Physiol.* **135**, 197–215 (2010).
47. Xie, C., Zhen, X. G. & Yang, J. Localization of the activation gate of a voltage-gated Ca^{2+} channel. *J. Gen. Physiol.* **126**, 205–212 (2005).
48. Stotz, S. C., Jarvis, S. E. & Zamponi, G. W. Functional roles of cytoplasmic loops and pore lining transmembrane helices in the voltage-dependent inactivation of HVA calcium channels. *J. Physiol.* **554**, 263–273 (2003).
49. Kim, D. E., Chivian, D. & Baker, D. Protein structure prediction and analysis using the Robetta server. *Nucleic Acids Res.* **32**, W526–W531 (2004).
50. Chagot, B., Potet, F., Balsler, J. R. & Chazin, W. J. Solution NMR structure of the C-terminal EF-hand domain of human cardiac sodium channel $\text{Na}_v1.5$. *J. Biol. Chem.* **284**, 6436–6445 (2009).
51. Wang, C., Chung, B. C., Yan, H., Lee, S. Y. & Pitt, G. S. Crystal structure of the ternary complex of a Na_v C-terminal domain, a fibroblast growth factor homologous factor, and calmodulin. *Structure* **20**, 1167–1176 (2012).
52. Schneidman-Duhovny, D., Inbar, Y., Nussinov, R. & Wolfson, H. J. PatchDock and SymmDock: servers for rigid and symmetric docking. *Nucleic Acids Res.* **33**, W363–W367 (2005).
53. Black, D. J. *et al.* Calmodulin interactions with IQ peptides from voltage-dependent calcium channels. *Am. J. Physiol. Cell Physiol.* **288**, C669–C676 (2005).
54. Jencks, W. P. On the attribution and additivity of binding energies. *Proc. Natl Acad. Sci. USA* **78**, 4046–4050 (1981).
55. Chan, C. S. *et al.* ‘Rejuvenation’ protects neurons in mouse models of Parkinson’s disease. *Nature* **447**, 1081–1086 (2007).
56. Adams, P. J. & Snutch, T. P. Calcium channelopathies: voltage-gated calcium channels. *Subcell. Biochem.* **45**, 215–251 (2007).
57. Sarhan, M. F., Van Petegem, F. & Ahern, C. A. A double tyrosine motif in the cardiac sodium channel domain III-IV linker couples calcium-dependent calmodulin binding to inactivation gating. *J. Biol. Chem.* **284**, 33265–33274 (2009).
58. Johnson, K. J. *Numerical Methods in Chemistry* (Marcel Dekker, 1980).
59. Mashich, E., Schneidman-Duhovny, D., Andrusier, N., Nussinov, R. & Wolfson, H. J. FireDock: a web server for fast interaction refinement in molecular docking. *Nucleic Acids Res.* **36**, W229–W232 (2008).
60. Chaudhury, S., Lyskov, S. & Gray, J. J. PyRosetta: a script-based interface for implementing molecular modeling algorithms using Rosetta. *Bioinformatics* **26**, 689–691 (2010).

Acknowledgements

We thank Paul Adams, Ivy Dick and other members of the Ca^{2+} signals lab for valuable comments. This work was supported by grants from the NIMH (to D.T.Y.), NIDCD (to P.S.Y. and Paul Fuchs) and NIMH (to M.B.J.). Michael Tadross furnished early insights regarding the potential differences of mutation effects on C- and N-lobe forms of CDI. Wanjun Yang contributed substantial technical support, including western blots in Supplementary Figure S9

Author contributions

M.B.J., P.S.Y. and H.B. created mutant channels, performed electrophysiology and FRET experiments, and undertook extensive data analysis. M.B.J. pioneered and conducted many of the FRET binding assays, performed molecular modelling and undertook extensive software development. D.Y. conceived and supervised the project; and helped formalize iTL theory and translation of 3^3 -FRET to E-FRET methodologies. All authors refined hypotheses, wrote the paper and created figures.

Additional information

Supplementary Information accompanies this paper at <http://www.nature.com/naturecommunications>

Competing financial interests: The authors declare no competing financial interests.

Reprints and permission information is available online at <http://npg.nature.com/reprintsandpermissions/>

How to cite this article: Ben Johny, M. *et al.* Dynamic switching of calmodulin interactions underlies Ca^{2+} regulation of $\text{Ca}_v1.3$ channels. *Nat. Commun.* **4**:1717 doi: 10.1038/ncomms2727 (2013).

Supplementary Information**Dynamic switching of calmodulin interactions underlies Ca²⁺ regulation of Ca_v1.3 channels**

Manu Ben Johny, Philemon S. Yang, Hojjat Bazzazi, and David T. Yue (2013).

*Nature Communications***Table of Contents**

Supplementary Note 1	Specific Langmuir equations for C- and N-lobe CDI subsystems.
Supplementary Note 2	Uniqueness of the Langmuir equation outcome for two conditions.
Supplementary Note 3	Hypothetical case of secondary effector sites detected by iTL analysis.
Supplementary Note 4	Generalization of iTL analysis to schemes of arbitrary architecture.
Supplementary Note 5	Extended data for Ca ²⁺ /CaM interaction with IQ domain.
Supplementary Note 6	Rationale for FRET constructs probing Ca ²⁺ /CaM interactions with IQ domain.
Supplementary Note 7	Extended data for Y[+3]D construct.
Supplementary Note 8	Rationale for FRET analysis of Ca ²⁺ /CaM interaction with NSCaTE.
Supplementary Note 9	Extended data for N-lobe CDI and NSCaTE.
Supplementary Note 10	Extended data for C-lobe CDI and NSCaTE.
Supplementary Note 11	Rationale for FRET analysis of Ca ²⁺ /CaM interaction with PCI.
Supplementary Note 12	Extended data for PCI hotspots.
Supplementary Note 13	Dependence of IQ/PCI interaction on Ca ²⁺ /CaM.
Supplementary Note 14	Extended data for IQ interaction with PCI.
Supplementary Note 15	Explicit Langmuir form of IQ interaction with PCI.
Supplementary Note 16	Extended data for apoCaM interaction with CI module.
Supplementary Note 17	Rationale for FRET constructs for apoCaM versus CI interaction.
Supplementary Note 18	Explicit Langmuir form for apoCaM interaction with channel CI region.
Supplementary Note 19	<i>De novo</i> prediction of CI region structures.
Supplementary Note 20	Docking of apoCaM to CI region.
Supplementary Note 21	Enhanced N-lobe CDI with decreased channel affinity for N-lobe of apocaM.
Supplementary Note 22	Docking of Ca ²⁺ /CaM to CI region.
Supplementary Note 23	Aggregate association constant for IQ-PCI-Ca ²⁺ /CaM tripartite complex.
Supplementary Note 24	Design and characterization of FRET 2-hybrid interaction pairs.

Supplementary Note 1. Specific Langmuir equations for C- and N-lobe CDI subsystems

For the five-state scheme in main text Fig. 2a, we derive the explicit Langmuir form appropriate for mutations selectively affecting γ_1 , as follows.

For N-lobe CDI, the rapid (un)binding of Ca^{2+} relating to this lobe of CaM permits the rapid CaM approximation¹⁴, which allows the equivalent reaction scheme below (Supplementary Fig. S1a). Here, states 2 and 3 of main text Fig. 2a merge into a single compound 2-3 state, with corresponding adjustments to adjacent association constants. Accordingly, the following specific Langmuir equation arises

$$CDI / CDI_{\max} = \frac{CDI}{\underbrace{CDI_m \cdot \gamma_2 / (1 + \gamma_2)}_{CDI_{\max}}} = \frac{K_{a,\text{EFF}}}{K_{a,\text{EFF}} + \underbrace{(1 + \varepsilon \cdot (1 - P_O)) / (s \cdot P_O \cdot (1 + \gamma_2))}_{\Lambda}} \quad (\text{S1})$$

where P_O is the channel open probability, CDI_m is the CDI strength that would be observed if all channels ended up in state 5 at steady state, and other terms are given in main text Fig. 2a and Eq. 1 (where $\gamma_1 = \underline{s} \cdot K_{a,\text{EFF}}$, and s is a constant of proportionality).

For C-lobe CDI, the slow unbinding of Ca^{2+} from the C-terminal lobe of CaM permits the slow-CaM approximation as derived in our previous publication¹⁴. This allows the time-varying rate constants between states 2 and 3 of main text Fig. 2a to assume their time-invariant analogs as diagrammed below in Supplementary Fig. S1b. Accordingly, the following specific Langmuir equation arises

$$CDI / CDI_{\max} = \frac{CDI}{\underbrace{CDI_m \cdot \gamma_2 / (1 + \gamma_2)}_{CDI_{\max}}} = \frac{K_{a,\text{EFF}}}{K_{a,\text{EFF}} + \underbrace{[1 + (1 + \varepsilon) \cdot k_{\text{off}} / (P_O \cdot C_{\text{spike}}^2 \cdot k_{\text{on}})] / [s \cdot (1 + \gamma_2)]}_{\Lambda}} \quad (\text{S2})$$

where C_{spike} is the free Ca^{2+} concentration in the channel nanodomain, as sensed by the C-terminal lobe of CaM. Experimental estimates of C_{spike} approximate 50-100 μM ⁶¹.

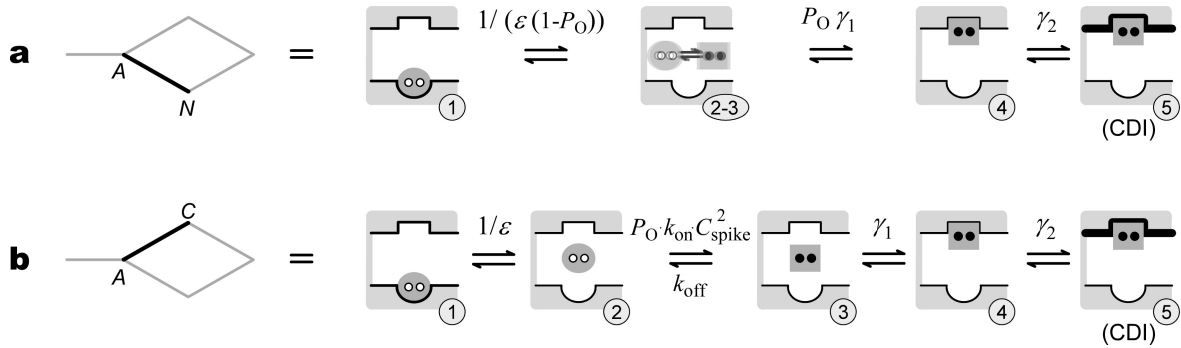


Figure S1. Explicit formulation of Langmuir equation for reaction system in main text Fig. 2a, assuming selective mutational perturbation of Ca^{2+} /CaM binding to effector site (γ_1 step). **(a)** N-lobe CDI case, pertaining to subsystem as diagrammed on left (cf., main text Fig. 2e). Rapid Ca^{2+} binding and unbinding in relation to N-terminal lobe of CaM enables rapid-equilibrium approximation, where states 2 and 3 merge into a single compound 2-3 state. As well, approximation makes adjustments to association constants on the left and right of state 2-3, where adjustments involve functions of open probability P_O . **(b)** C-lobe CDI case, pertaining to subsystem as diagrammed on left (cf., main text Fig. 2d). Slow Ca^{2+} unbinding from C-terminal lobe of CaM permits ‘slow CaM approximation,’ where the rate constant for transitions from states 2 to 3 can be approximated by $P_O \cdot k_{\text{on}} \cdot C_{\text{spike}}^2$. Here, C_{spike} is the free concentration of Ca^{2+} at C-terminal lobe of CaM.

Supplementary Note 2. Uniqueness of the Langmuir equation outcome for two conditions

The derivations in Supplementary Note 1 indicate that a Langmuir equation will result if two conditions are met. (1) Point mutations only affect one transition within the system, assumed to be γ_1 in these derivations. (2) $K_{a,\text{EFF}}$, the association constant measured from channel-peptide experiments, is proportional to the corresponding association constant within the holochannel ($\gamma_1 = s \cdot K_{a,\text{EFF}}$, and s is a constant). Is this outcome (of data following a Langmuir equation) unique to these two conditions? By

carefully considering Eqs. S1 and S2, we can argue for such uniqueness. For example, if mutations were to affect more than one transition (γ_1 in the considerations of Supplementary Note 1), then Λ would not be a constant with respect to $K_{a,EFF}$, and a Langmuir equation (defined with Λ being a constant) would not result. As another example, suppose that $K_{a,EFF}$ (measured from peptide experiments) does not maintain a strict constant of proportionality with γ_1 (pertaining to holochannels), so that s is no longer a constant in the relationship $\gamma_1 = s \cdot K_{a,EFF}$. Inspection of Eqs. S1 and S2 again reveals that Λ will no longer be a constant with respect to $K_{a,EFF}$, and a Langmuir equation will no longer result. Hence, to the extent that a Langmuir equation is resolved by experimental data (main text Fig. 4f, 5i, 6f, and 7i), we would argue that conditions 1 and 2 above are indeed being satisfied.

Supplementary Note 3. Hypothetical case of secondary effector sites detected by iTL analysis

Another potentially important scenario concerns the possible existence of an additional effector site for a lobe of CaM, which is not addressed by our alanine scan. For example, consider a configuration with two effector sites for the Ca^{2+} -bound N-lobe of CaM (N_1 and N_2 in Fig. S2a below). For simplicity, assume CDI to be proportional to the steady-state occupancy of states N_1 and N_2 . Under overexpression of CaM_{34} to restrict channels to configurations A, N_1 , and N_2 , CDI would then be proportional to $(K_1 + K_2) / (1 + K_1 + K_2)$, with equilibrium constants as shown.

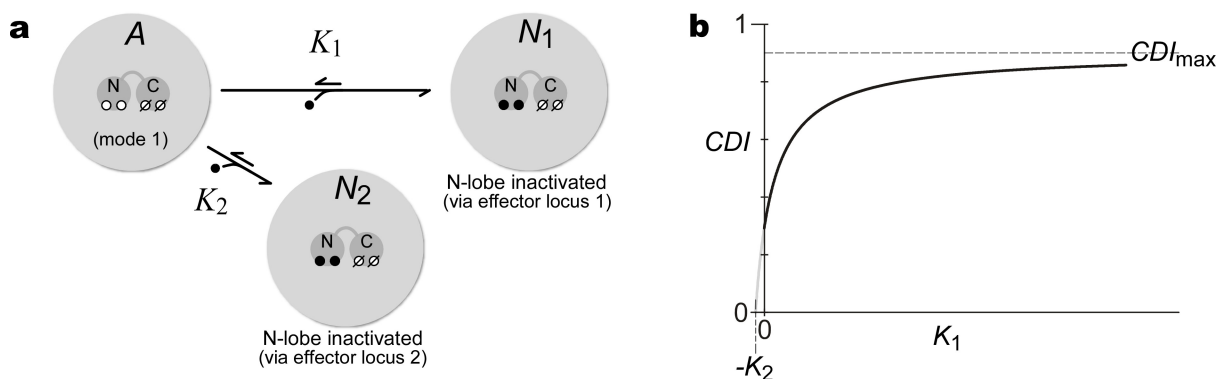


Figure S2. Variation of baseline iTL predictions for a hypothetical system featuring two effector sites for a given lobe of CaM. (a) Subsystem as isolated by strong overexpression of CaM_{34} . (b) Modified Langmuir function produced by this variant system. CDI_{max} is the maximum CDI seen when all channels are in N_1 or N_2 .

Suppose our alanine scan only touches on site N_1 , such that our peptide binding assays with Ca^{2+}/CaM only pick up mutation effects on K_1 . Plotting this in Supplementary Fig. S2b would still reveal a Langmuir function, but with a non-zero y intercept. No clear results of this sort were observed experimentally, so there was no overt indication of additional effector sites in our data.

Supplementary Note 4. Generalization of iTL analysis to schemes of arbitrary architecture

This section generalizes the iTL postulates to calmodulatory regulation systems of any architecture as schematized in Supplementary Fig. S3b, not just those in Supplementary Fig. S1. States are denoted as nodes, and transitions between them as interconnecting segments. For purposes of argument, occupancy of state m corresponds to a channel that has undergone CDI. We assume that the system satisfies the constraints of thermodynamic equilibrium, a presumption that will be defended later on. According to thermodynamics, we can represent the behavior of this general system as a branched network without any cycles, as shown in Supplementary Fig. S3b. Completing the cycles would not change the steady-state solution to the systems, because of thermodynamic cycle constraints⁶². Will perturbation of a single transition within this general scheme also yield a Langmuir equation?

Consider first the simplest scenario, a linear scheme that connects states 1 to m (Supplementary Fig. S3a), which we call the ‘forward path.’ It is simple to show that the equilibrium probability of occupying state m (assumed tantamount to the CDI state) is given by the general form:

$$P_m = \frac{K_{12} \cdot K_{23} \cdot \dots \cdot K_{m-2, m-1} \cdot K_{m-1, m}}{1 + K_{12} + K_{12} \cdot K_{23} + \dots + K_{12} \cdot K_{23} \cdot \dots \cdot K_{m-2, m-1} \cdot K_{m-1, m}} = \frac{F_{1m}}{F_{11} + F_{12} + \dots + F_{1m}} \quad (\text{S3})$$

Suppose we are interested in the effects of alterations in the transition from state i to state $i+1$ in the forward path. This would alter the equilibrium constant $K_{i, i+1}$. Algebraic manipulation of Equation S3 demonstrates that P_m can always be transformed into a Langmuir-like form, regardless the value of i . This algebraic process is shown below.

$$P_m = \frac{\left[F_{1m} / K_{i, i+1} \right] K_{i, i+1}}{\left[(1 / K_{i, i+1}) \sum_{n=i+1}^m F_{1n} \right] \left[\sum_{n=1}^i F_{1n} \right] \cdot \left[K_{i, i+1} / \sum_{n=i+1}^m F_{1n} \right] + K_{i, i+1}} \quad (\text{S4})$$

Noting that none of the terms in square brackets contain the $K_{i, i+1}$ term, we can rewrite Equation S4 as a genuine Langmuir function

$$P_m = A \cdot \frac{K_{i, i+1}}{\Lambda + K_{i, i+1}} \quad (\text{S5})$$

where the definitions of A and Λ are obvious by comparison of Equations S4 and S5.

What happens if the system also contains states connected by branching paths (shown as black segments in Supplementary Fig. S3b) that emanate from various states in the forward path? The added complexity turns out to be easily accommodated, because it is straightforward to show that Equation S3 becomes the closely similar form below.

$$P_m = \frac{F_{1m}}{F_{11}(1 + \Omega_1) + F_{12}(1 + \Omega_2) + \dots + F_{1m}(1 + \Omega_m)} \quad (\text{S6})$$

where Ω_n is comprised of various products of equilibrium constants relating to branches emanating from state n . Importantly, none of the equilibrium constants in the forward path are contained within Ω_n . Algebraic manipulation analogous to that in Equation S4 then demonstrates that Equation S6 can be transformed into a Langmuir function in terms of $K_{i, i+1}$ as follows.

$$P_m = \frac{\left[F_{1m} / K_{i, i+1} \right] K_{i, i+1}}{\left[(1 / K_{i, i+1}) \sum_{n=i+1}^m F_{1n} (1 + \Omega_n) \right] \left[\sum_{n=1}^i F_{1n} (1 + \Omega_n) \right] \cdot \left[K_{i, i+1} / \sum_{n=i+1}^m F_{1n} (1 + \Omega_n) \right] + K_{i, i+1}} \quad (\text{S7})$$

$$P_m = A \cdot \frac{K_{i, i+1}}{\Lambda + K_{i, i+1}} \quad (\text{S8})$$

What if we are concerned about changes in an equilibrium constant within one of the branches, not in the given forward path? The insight here is that there is nothing special about the particular forward path used thus far, as portrayed in Supplementary Fig. S3a. We might as well redefine the forward path to include the new transition of interest, as portrayed in Supplementary Fig. S3c. Then, the proof would proceed identically for the new forward path, and an appropriate Langmuir function could again be formulated for P_m .

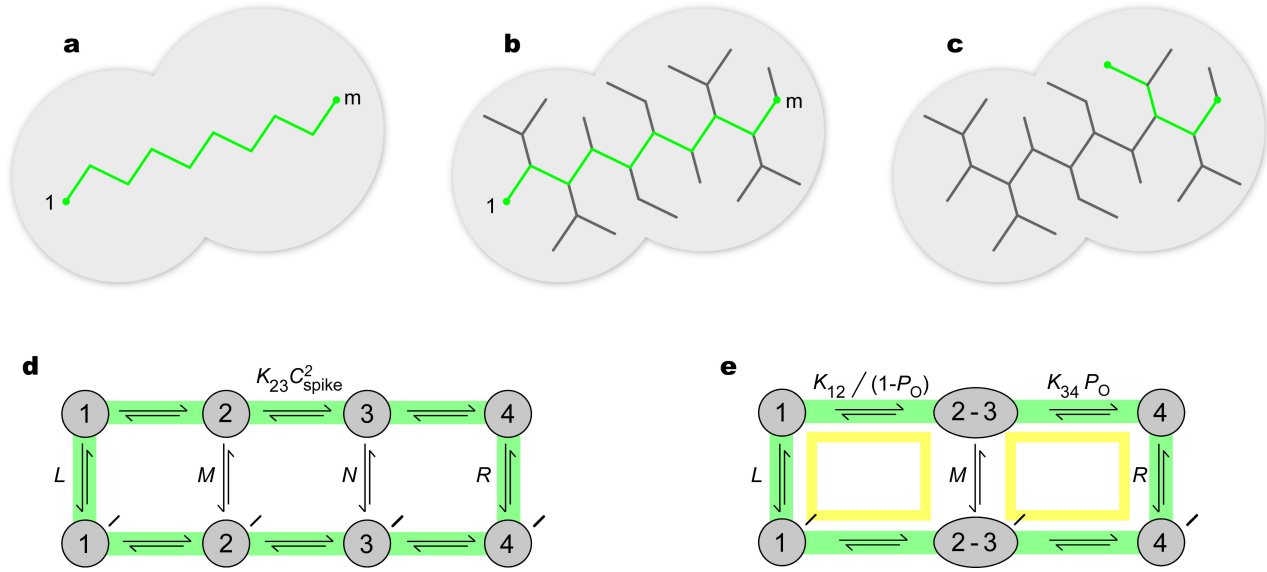


Figure S3. Derivation of iTL theory. (a) In general, a calmodulin regulatory system may be represented by a branched network without cycles, where nodes denote states and branches diagram transitions between states. The green pathway in a, consisting of a single ‘forward path,’ illustrates the simplest type of network. iTL analysis posits that the equilibrium occupancy of state m depends on K_{i+1} via a Langmuir relationship. (b) Adding branches to the forward pathway spares the ability to represent state m equilibrium occupancy as a Langmuir relation incorporating K_{i+1} . (c) For alterations to a transition outside the ‘forward path,’ we may redefine the ‘forward path’ to include this transition. (d) ‘Slow CaM approximation’ for C-lobe CDI satisfies thermodynamic cycle constraints, enabling iTL analysis. L , equilibrium constant from states 1 to 1’. M , N , and R defined similarly for transitions from upper to lower rows. (e) ‘Rapid-CaM approximation’ for N-lobe CDI also satisfies thermodynamic cycle mandates.

One may worry that for the actual CDI process, the system is not in true thermodynamic equilibrium⁶², as assumed for the deductions above. Instead, the system achieves a steady state⁶² that arises in response to millisecond-long pulses reaching Ca^{2+} concentration C_{spike} . These pulses are tightly synchronized with individual stochastic openings of the channel¹⁴. No sustained, global Ca^{2+} inputs need be considered because all experiments are performed with 10 mM BAPTA as Ca^{2+} chelator in the whole-cell dialyzate. This concern may be dealt with in two phases.

First, consider the situation when we need only account for Ca^{2+} binding to the C-lobe of CaM, as in our experiments characterizing C-lobe CDI in isolation. In general, the forward binding reaction of Ca^{2+} to CaM is given by a stochastically varying rate constant: when Ca^{2+} is zero during channel closures, this rate constant is also zero; when Ca^{2+} is equal to C_{spike} during channel openings, this rate constant is approximately equal to $k_{\text{on}} \cdot C_{\text{spike}}^2$. The unbinding rate constant is always approximately equal to k_{off} . We use the term ‘approximate’ because the binding and unbinding of two Ca^{2+} ions to a lobe of CaM is highly cooperative^{27,63}, but not infinitely so. With specific reference to the C-lobe of CaM, the unbinding of Ca^{2+} is slow compared to surrounding transitions, so a ‘slow-CaM approximation’ may be invoked, as proved in our previous publication¹⁴. In this slow-CaM regime, the time-varying on rate constant may be replaced by the time-invariant entity $k_{\text{on}} \cdot C_{\text{spike}}^2 \cdot P_0$, where P_0 is the steady-state open probability of non-inactivated channels. Hence, we have an equivalent slow-CaM system, where the Ca^{2+} binding transition in question is characterized by the time-invariant equilibrium constant $k_{\text{on}} \cdot C_{\text{spike}}^2 \cdot P_0 / k_{\text{off}}$. Will this equivalent system satisfy all thermodynamic cycle constraints? It turns out that the answer is yes, as follows. The actual system, being physically realizable without external energy consumption, certainly satisfies all thermodynamic cycle constraints at any steady value of C_{spike} (say $C_{\text{spike/original}}$), where the equilibrium constant for Ca^{2+} binding and unbinding equals $k_{\text{on}} \cdot C_{\text{spike/original}}^2 / k_{\text{off}}$. Now suppose we change the level of C_{spike} to $C_{\text{spike/new}} = C_{\text{spike/original}} \cdot (P_0)^{1/2}$. The original system will of course also satisfy all thermodynamic cycle constraints, with the equilibrium constant in question now equal to $k_{\text{on}} \cdot C_{\text{spike/original}}^2 \cdot P_0 / k_{\text{off}}$. But this equilibrium constant

is now the same as for the equivalent system obtained with the slow-CaM approximation. Thus, the equivalent system with the slow-CaM approximation will always satisfy all thermodynamic cycle constraints.

Second, consider the situation where only Ca^{2+} binding to the N-lobe of CaM need be considered, as in our experiments characterizing N-lobe CDI in isolation. The full spectrum of concerns in regard to potential violations of thermodynamics is embodied by the generic layout shown in Fig. S3d. The four main states (1, 2, 3, and 4) correspond to those shown in main text Fig. 1a, and the equilibrium constants L , M , N , and R may represent the product of equilibrium constants for multiple interconnected transitions. For example, if states 1 and 1' in Supplementary Fig. S3d were connected by an intermediate state x , where K_{1x} would be the equilibrium constant from state 1 to state x , and $K_{x1'}$ the constant from state x to state 1', then L would equal $K_{1x} \cdot K_{x1'}$. In this sense, transitions affiliated with L , M , N , and R allow representation of all classes of potential thermodynamic cycles containing the Ca^{2+} binding and unbinding steps between states 2 and 3 (lobe of CaM in channel alcove undergoing Ca^{2+} binding and unbinding). The 'primed' states represent the original calmodulatory states under a different configuration of the channel (e.g., hypothetically something akin to an alternate configuration of auxiliary subunit modulation of the apoCaM preassociation surface). In this N-lobe scenario, the binding and unbinding of Ca^{2+} to the N-lobe is rapid enough to track the millisecond stochastic gating of channels. Accordingly, a 'rapid-CaM approximation' may be invoked, as argued in our previous publication¹⁴. Under this approximation, the system morphs into the equivalent time-invariant system shown in Fig. S3e, where certain equilibrium constants now incorporate P_0 , the steady-state open probability of a non-inactivated channel. Does this equivalent system also satisfy thermodynamic cycle mandates? Certain constraints on this question may be deduced from the original system in Fig. S3d, specifically by considering the green-shaded cycle. From consideration of this loop, we have the thermodynamic constraint⁶² that

$$1 = \frac{K_{12} \cdot K_{23} \cdot C_{\text{spike}}^2 \cdot K_{34} \cdot R}{K_{12}' \cdot K_{23}' \cdot C_{\text{spike}}^2 \cdot K_{34}' \cdot L} = \frac{K_{12} \cdot K_{23} \cdot K_{34} \cdot R}{K_{12}' \cdot K_{23}' \cdot K_{34}' \cdot L} \quad (\text{S9})$$

Evaluating the corresponding green-shaded loop in the equivalent system of Fig. S3e, we can check whether the thermodynamic cycle constraint will also be satisfied, as follows.

$$\text{cycle constraint parameter} = \frac{(K_{12}/(1-P_0)) \cdot K_{34} \cdot P_0 \cdot R}{(K_{12}'/(1-P_0)) \cdot K_{34}' \cdot P_0 \cdot L} = \frac{K_{12} \cdot K_{34} \cdot R}{K_{12}' \cdot K_{34}' \cdot L} \quad (\text{S10})$$

If we make the reasonable assumption that channel configuration does not influence Ca^{2+} binding and unbinding to a lobe of CaM that is *free* in the channel alcove, then $1 = K_{23} / K_{23}'$ in Equation S9, and the cycle constraint parameter in Equation S10 for the equivalent system becomes unity. Thus the equivalent calmodulin regulatory system in Fig. S3e will satisfy thermodynamic cycle constraints in regard to the green-shaded loop. If we assume that $1 = K_{23} / K_{23}'$ in Fig. S3d, then thermodynamic constraints mandate that $M = N$. Accordingly, the middle vertical transition from compound state 2-3 in Fig. S3e is specified by M . The yellow loops in Fig. S3e will then also satisfy thermodynamic constraints. Hence, all classes of loops in the rapid-CaM approximation for N-lobe CDI satisfy thermodynamic cycling constraints, if we make the reasonable assumption that $1 = K_{23} / K_{23}'$. In conclusion, iTL analysis may be applied to CDI, even as driven by pulsatile Ca^{2+} driving either C- or N-lobe of CaM.

Supplementary Note 5. Extended binding and electrophysiological data for Ca^{2+} /CaM interaction with IQ domain

Supplementary Fig. S4 (leftmost column) explicitly displays further FRET binding curves relating to mutant IQ domains (red symbols and fit). For reference, the curve for the wild-type IQ domain is reproduced from main text Fig. 3c as a gray relation. T[-10]A (Supplementary Fig. S4a) and V[-9]A (Supplementary Fig. S4b), D[+2]A (Supplementary Fig. S4h), and F[4]A (Supplementary Fig. S4j) all weaken binding of Ca^{2+} /CaM to the IQ peptide. Alanine substitutions at other loci did not appreciably alter Ca^{2+} /CaM interaction with the IQ domain, as shown in the remaining panels.

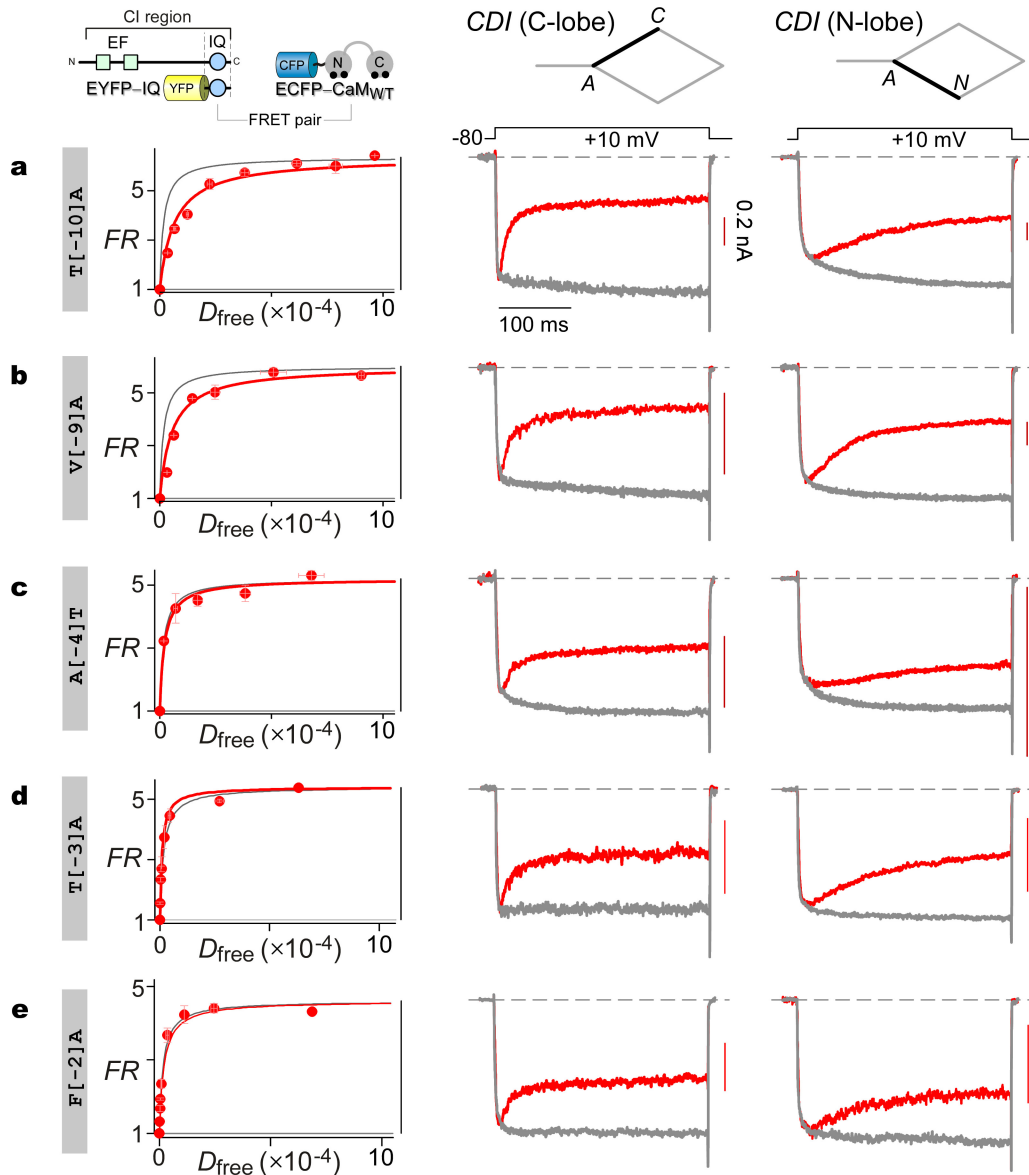


Figure S4. Ca^{2+} /CaM binding and electrophysiological data for various point substitutions within the $\text{Ca}_v1.3$ IQ domain (labelled at far left). Leftmost column shows 3^3 -FRET binding curves in red, with constructs diagrammed at top. For ease of visual comparison, the gray trace reports the wild-type interaction relation (derived from main text Fig. 2j) scaled to a common maximal FR amplitude (bar at far right). Single-cell FRET measured binned into symbols averaging ~ 6 cells for respective panels a–j. Middle column, isolated C-lobe CDI, corresponding to subsystem schematized at the top. Red trace with Ca^{2+} as charge carrier, with corresponding 0.2 nA scale bar at right. Gray trace with Ba^{2+} as charge carrier, amplitude scaled to facilitate comparison of decay kinetics. Rightmost column, isolated N-lobe CDI.

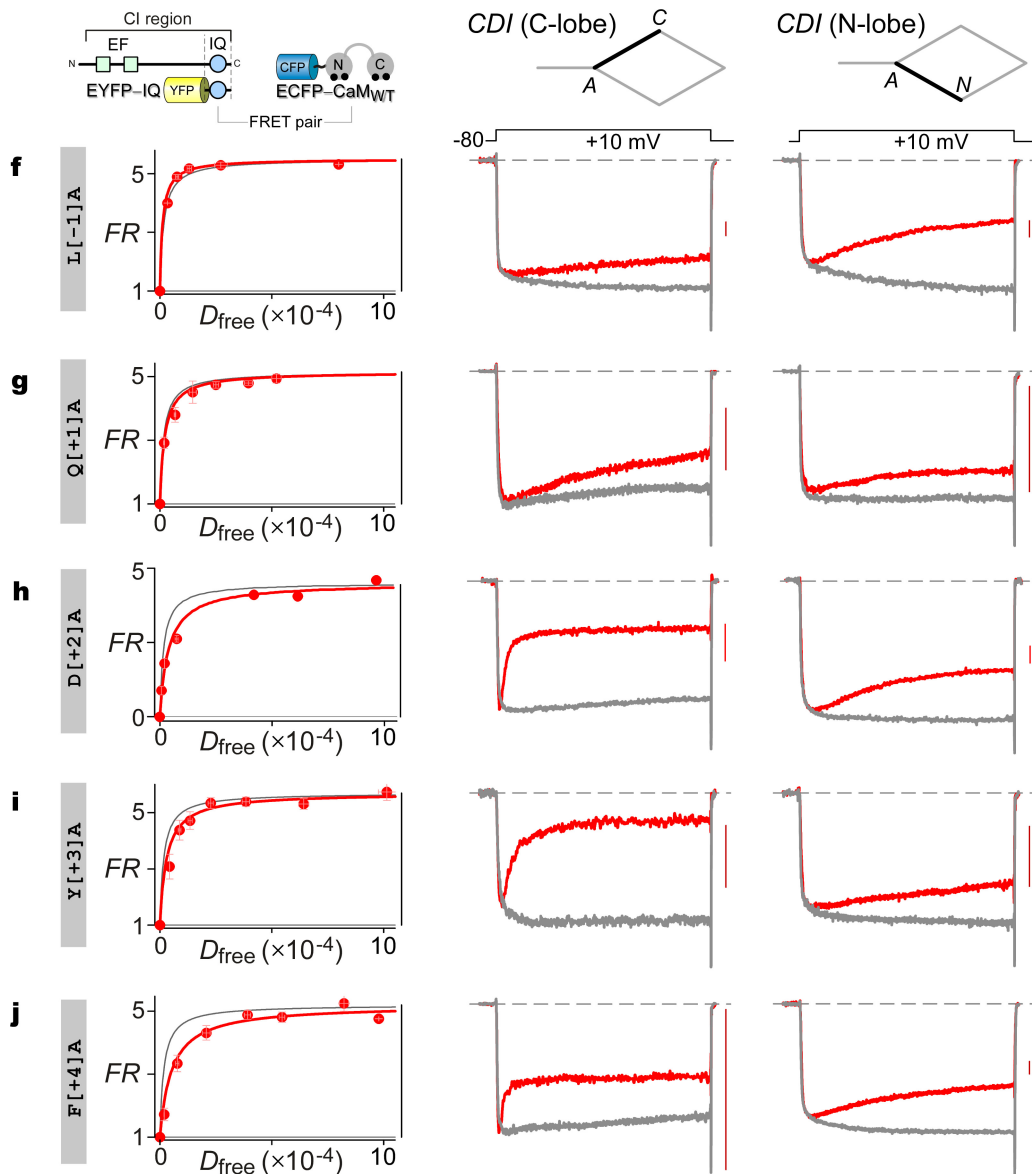


Figure S4 (continued). Format as in Fig S2.1 above.

These variable changes in binding correlated poorly with alterations in CDI, as shown in the remaining columns. The profile of isolated C-lobe CDI is shown in the middle column of Supplementary Fig. S4. It is telling that C-lobe CDI remained essentially unchanged for T[-10]A (Supplementary Fig. S4a) and V[-9]A (Supplementary Fig. S4b) constructs, despite significant attenuation of $\text{Ca}^{2+}/\text{CaM}$ interaction. By contrast, C-lobe CDI was appreciably weaker within A[-4]T (Supplementary Fig. S4c), T[-3]A (Supplementary Fig. S4d), F[-2]A (Supplementary Fig. S4e), L[-1]A (Supplementary Fig. S4f), and Q[+1]A (Fig. S4e) constructs, in the face of unchanged $\text{Ca}^{2+}/\text{CaM}$ interaction with corresponding IQ elements. These incongruencies argue against the IQ domain alone as an effector site for the C-lobe of $\text{Ca}^{2+}/\text{CaM}$.

Likewise, for the isolated N-lobe form of CDI shown in the rightmost column of Supplementary Fig. 4, CDI was not significantly reduced for nearly all of the constructs. This outcome argues against the IQ domain as effector site for the N-lobe of $\text{Ca}^{2+}/\text{CaM}$. Only the Q[+1]A construct exhibited some decrease in N-lobe CDI, potentially via higher-order effects to increase apoCaM affinity. Altogether, these results and those in the main text Fig. 3 provide compelling support that the effector interfaces for $\text{Ca}^{2+}/\text{CaM}$ extend somewhere beyond the IQ domain itself.

Supplementary Note 6. Rationale for FRET constructs probing $\text{Ca}^{2+}/\text{CaM}$ interactions with IQ domain

We utilized $\text{Ca}^{2+}/\text{CaM}$ as the FRET partner with IQ, to afford a convenient test for effector function. This FRET pairing yielded well-resolved binding curves as shown in main text Fig. 3c. These curves can be understood within the context of iTL analysis as follows.

Consider first the generic 4-state scheme of $\text{CaM}/\text{peptide}$ binding⁵⁴, with forward equilibrium constants as diagrammed (Supplementary Fig. S5a). This configuration pertains to a ‘canonical’ CaM binding site where both lobes of CaM may bind well. K_C is the constant for initial C-lobe binding to the unbound peptide binding site, and K_N is the constant for initial N-lobe binding to the unbound site. Once one lobe of CaM is bound (forming states C or N), the other lobe may (in the generic case) also bind to the peptide site to create the doubly bound state (CN), usually with considerable positive cooperativity signified by a large value of λ . Note that this system of equilibrium constants is constrained by thermodynamic-cycle rules. Typically, λ is large enough that the main bound state is CN, with very little occupancy of C or N states⁶⁴. Hence, the overall binding reaction can be well approximated by the two-state scheme in Supplementary Fig. S5b, where the total equilibrium constant for the reaction is $K_T = K_C \cdot K_N \cdot \lambda$, with respective binding terms $\Delta G_T = \Delta G_C + \Delta G_N + \Delta G_{CN}$ (recall that $\Delta G = -R \cdot T \cdot \ln(K)$).

That said, IQ mutations are unlikely to change λ , an entity that reflects CaM interlobe geometry as specified by its linker region. Furthermore, as we mainly undertook FRET characterization of IQ mutations that strongly affected C-lobe CDI, we were investigating only those mutations that could potentially affect the C-lobe interface and K_C , rather than K_N . Importantly, then, the fold change in K_T produced by mutations, which we measured by FRET assays, would therefore be proportional to the fold-change in K_C , which is precisely the relevant entity for iTL analysis.

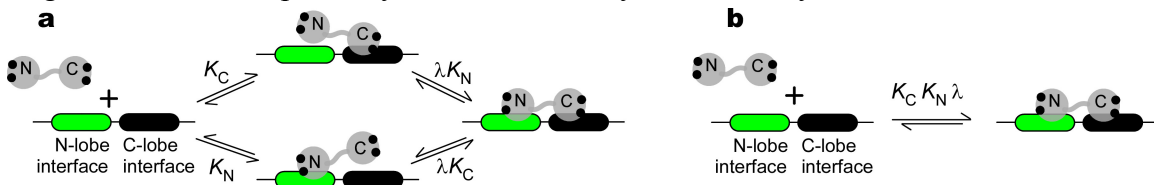


Figure S5. Rationale for FRET pair probing IQ domain. (a) Generic scheme for $\text{Ca}^{2+}/\text{CaM}$ interaction with peptide site. (b) Approximate scheme if cooperativity λ is positive and large.

Supplementary Note 7. Extended data for Y[3]D construct

Supplementary Fig. S4a, b described extensive data that T[-10]A and V[-9]A substitution within the $\text{Ca}_v1.3$ IQ domain disrupted $\text{Ca}^{2+}/\text{CaM}$ interaction with the IQ element; yet, there was no appreciable reduction in either C-lobe or N-lobe CDI. These results argue against the IQ domain as effector site for $\text{Ca}^{2+}/\text{CaM}$. As a further extreme, we experimentally investigated the effects of Y[+3]D substitution, within the heart of the contact region between $\text{Ca}^{2+}/\text{CaM}$ and the IQ element. This perturbation would be anticipated to enormously disrupt $\text{Ca}^{2+}/\text{CaM}$ binding to the IQ element.

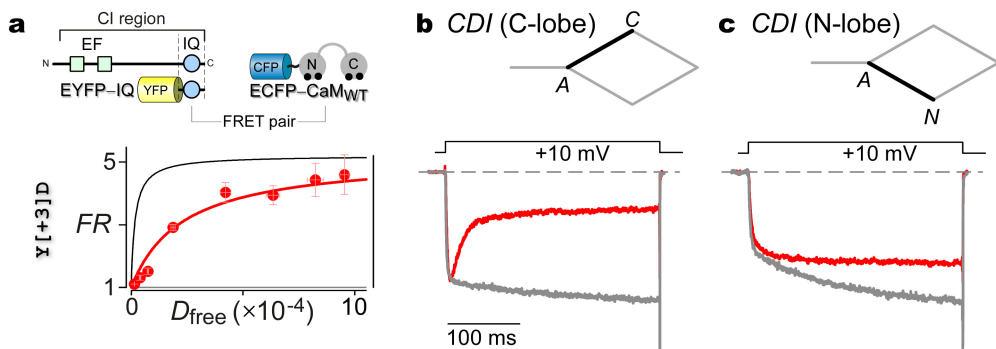


Figure S6. $\text{Ca}^{2+}/\text{CaM}$ binding and electrophysiology data for Y[+3]D substitution in the $\text{Ca}_v1.3$ IQ domain. Format as in Fig. S4. Symbols in panel a average ~ 10 cells each.

Indeed, FRET assays (Supplementary Fig. S6a) experimentally confirm a drastic reduction in affinity. Neither isolated C- or N-lobe CDI (Supplementary Fig. S6b, c) exhibited appreciable decrease from wild-type. In all, results with the Y[+3]D substitution furnish very strong evidence against an effector role of the IQ domain.

Supplementary Note 8. Rationale for FRET analysis of Ca^{2+} /CaM interaction with NSCaTE

For FRET experiments relating to the NSCaTE motif, we utilized fluorophore-labelled versions of CaM_{34} or CaM_{12} (mutants with selective Ca^{2+} binding at respective N- and C-terminal lobes of CaM⁹, main text Fig. 2c, i). We believe that this configuration best approximates the anticipated layout at the holochannel level, as follows.

When fluorophore-labelled, single-lobes of Ca^{2+} /CaM are pitted against NSCaTE in FRET assays (Supplementary Fig. S7a), the affinity is considerably higher than found with fluorophore-labelled Ca^{2+} /CaM (with both lobes present). Moreover, comparison of 3³-FRET analysis^{4,65} (yielding acceptor-centric FRET efficiency) to E-FRET analysis^{41,66} (yielding donor-centric FRET efficiency) furnishes binding curves with the same saturating FRET efficiency. The calibration between *FR* units and efficiency E_A is given in main text Fig. 3c (right). By these criteria⁶⁷, the stoichiometry of reaction is such that one lobe of CaM interacts with one NSCaTE peptide³³. The implication of these results is that the NSCaTE site can only bind well one lobe of CaM at a time (all that is required of NSCaTE in current concepts of N-lobe CDI; see main text Fig. 2a).

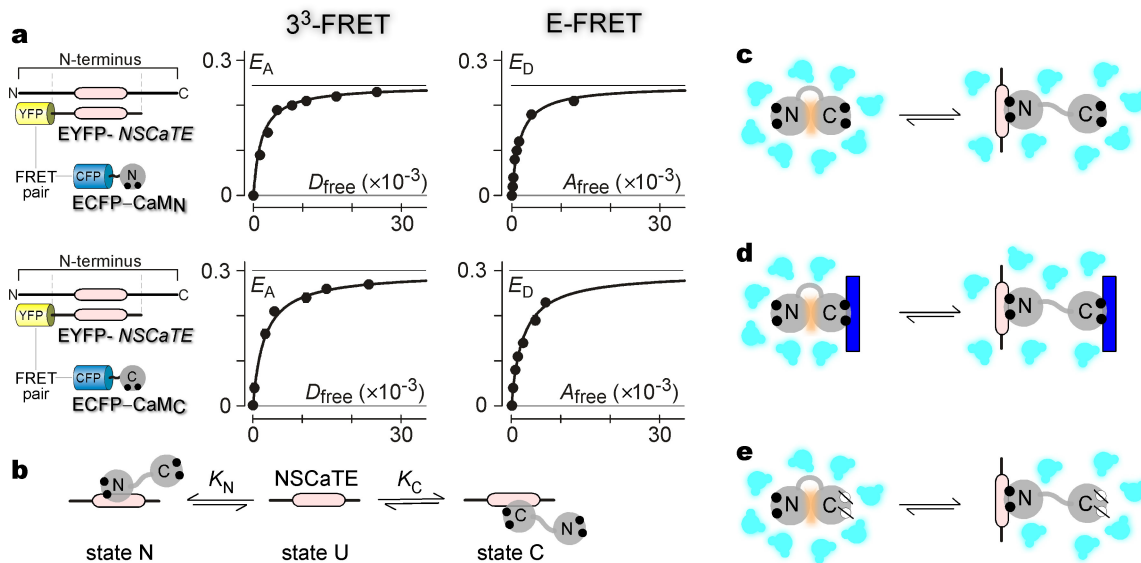


Figure S7. Rationale for FRET pairs probing NSCaTE. (a) NSCaTE peptide binds to both C- and N-lobes of Ca^{2+} /CaM with 1:1 stoichiometry. The relative binding affinities of NSCaTE for single lobes of CaM are significantly higher than that for Ca^{2+} /CaM. (b) Accordingly, either N- or C-terminal lobes of CaM may bind NSCaTE at one time. (c) Upon Ca^{2+} -binding, CaM adopts an open conformation exposing its hydrophobic core. When the N-lobe of Ca^{2+} /CaM binds to NSCaTE, the N-lobe is stabilized; however, the C-lobe of Ca^{2+} /CaM remains in a high energy configuration. (d) In the context of a holochannel, the C-lobe of CaM may remain bound to a channel target (blue rectangle). (e) By using CaM_{34} , we stabilize the C-lobe of CaM, allowing us to probe interaction of N-lobe of Ca^{2+} /CaM with NSCaTE peptide. Analogous logic rationalizes the use of CaM_{12} , while probing binding of the C-lobe of Ca^{2+} /CaM to NSCaTE.

That said, the choice of CaM species (C-lobe CaM, N-lobe CaM, CaM_{34} , CaM_{12} , or CaM_{WT}) used to probe interaction with NSCaTE becomes critical. By contrast to the generic 4-state scheme of CaM/peptide binding⁵⁴ (Supplementary Fig. S5), where both lobes of CaM may bind well, only one lobe of CaM can bind well at a time in the case of NSCaTE. This yields the three-state scheme shown in Supplementary Fig. S7b. If we were to probe this binding scheme with Ca^{2+} /CaM, an unfavorably complex scenario might arise, for two reasons. First, counting both states C and N as bound yields total fractional binding $B = (K_C + K_N) \cdot [\text{CaM}] / (1 + (K_C + K_N) \cdot [\text{CaM}])$. However, NSCaTE mutations might affect K_C and K_N in different ways in the FRET binding assays, whereas only the mutational effects on K_N are relevant for iTL analysis of N-lobe CDI. Hence, the measured changes in aggregate

binding affinity might belie the sought-after alterations in binding for a single lobe of CaM. Second, the values of K_N (and K_C) in the NSCaTE reaction with $\text{Ca}^{2+}/\text{CaM}$ are likely to underestimate the corresponding values relevant to the holochannel context. Supplementary Fig. S7c diagrams the likely chemical events involved in binding of the N-lobe of $\text{Ca}^{2+}/\text{CaM}$. Prior to binding, both lobes of $\text{Ca}^{2+}/\text{CaM}$ adopt a rather open conformation, which would be energetically unfavorable but for inter-lobe stabilization (tan cloud) and cloaking by water (cyan cloud puffs). Upon binding, the N-lobe adopts a lower energy state (yielding a favorable negative free energy change for the N-lobe, $\Delta G_{N/N\text{-lobe-binding}}$), but the C-lobe adopts a high-energy configuration having lost its inter-lobe stabilization (yielding an unfavorable positive free energy change for the C-lobe, $\Delta G_{C/N\text{-lobe-binding}}$). The total change in free energy upon N-lobe binding, $\Delta G_N = \Delta G_{N/N\text{-lobe-binding}} + \Delta G_{C/N\text{-lobe-binding}}$, is therefore considerably less negative than the $\Delta G_{N/N\text{-lobe-binding}}$ term itself, so that K_N is diminished. In the holochannel, the C-lobe of CaM presumably remains bound throughout the reaction of the N-lobe with NSCaTE (Fig. S7d) so that $\Delta G_{C/N\text{-lobe-binding}} \sim 0$ and $\Delta G_N \sim \Delta G_{N/N\text{-lobe-binding}}$. By the same logic ΔG_C is likely to be less negative than if the N-lobe were stabilized throughout.

Accordingly, we have used fluorophore-tagged versions of CaM_{34} and CaM_{12} in our FRET assays with NSCaTE. The purported chemical events relating to the binding of the N-lobe of $\text{Ca}^{2+}/\text{CaM}_{34}$ are shown in Fig. S7e. Here, the C-lobe (with mutated Ca^{2+} binding sites) adopts a near closed conformation throughout, so it is energetically stable in solution ($\Delta G_{C/N\text{-lobe-binding}} \sim 0$). The N-lobe is energetically unfavorable in solution, but for some stabilization by the closed C-lobe (lighter tan). Upon N-lobe binding to NSCaTE, it enjoys considerable energy stabilization, so that $\Delta G_{N/N\text{-lobe-binding}}$ is quite negative. Thus, $\Delta G_N \sim \Delta G_{N/N\text{-lobe-binding}}$ from the FRET assay approximates that envisioned for the holochannel context. Similar logic applies to the use of CaM_{12} in our FRET assays.

Single lobes of CaM might also be used in FRET assays with NSCaTE, but the binding reactions here would occur without the context of a linker and nearby partner lobe of CaM, as would be relevant to holochannels. Hence, we favored the use of CaM_{34} and CaM_{12} in our FRET assays with NSCaTE.

Supplementary Note 9. Extended data for N-lobe CDI and NSCaTE

The display below explicitly elaborates upon binding and electrophysiological data arguing that the NSCaTE segment on the amino terminus of channel serves as an effector site of the N-lobe of $\text{Ca}^{2+}/\text{CaM}$.

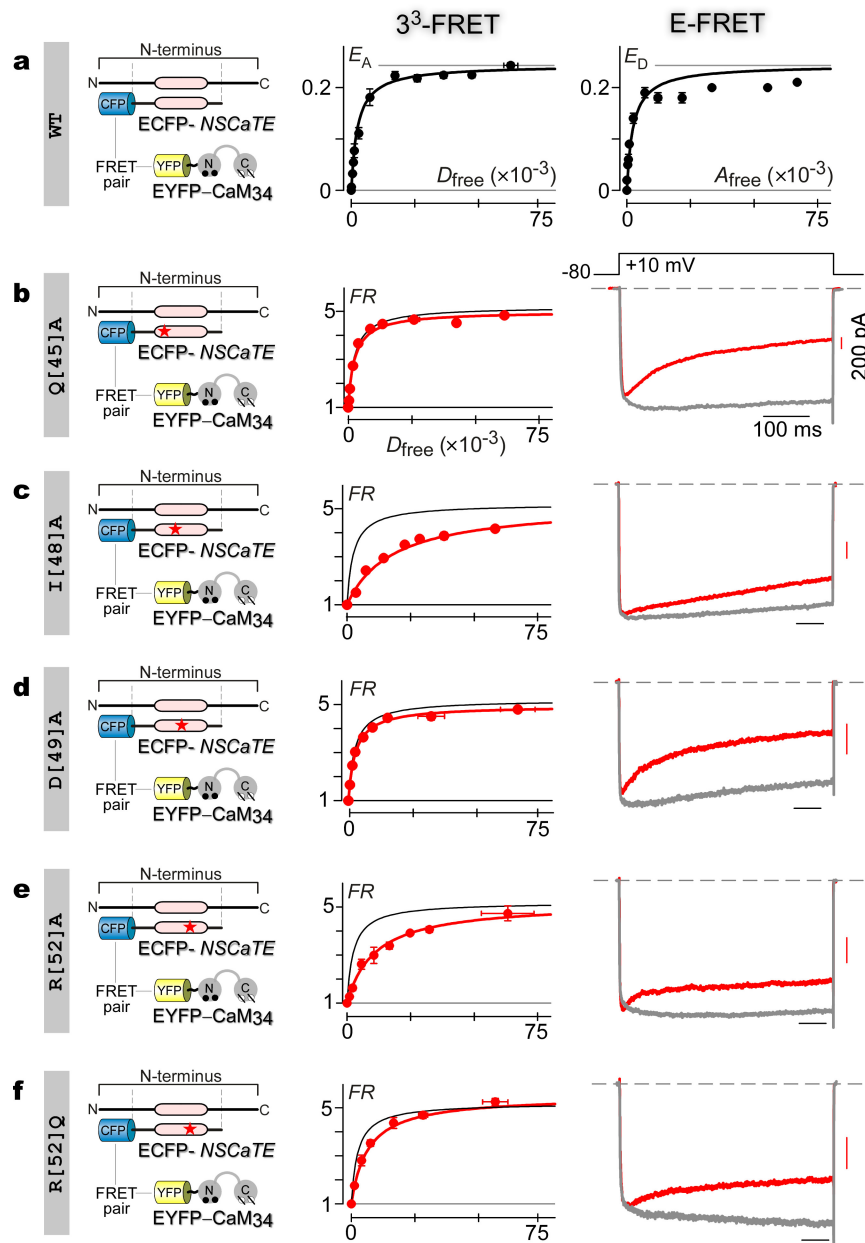


Figure S8. Extended investigation of the NSCaTE element as an effector site for N-lobe CDI. **(a)** FRET efficiencies between YFP-tagged $\text{Ca}^{2+}/\text{CaM}_{34}$ and CFP-tagged WT NSCaTE peptide as characterized with 3^3 -FRET (left) and E-FRET (right) metrics. Reassuringly, the maximal FRET efficiencies both approximated $E_{\max} = 0.24$, arguing for a 1:1 stoichiometry of binding between $\text{Ca}^{2+}/\text{CaM}_{34}$ and the NSCaTE peptide. **(b – f, left and middle)** Exemplar FRET 2-hybrid binding curves delineating relative $K_{a,\text{EFF}}$ for mutations in the NSCaTE element (red star). 3^3 -FRET efficiencies measured from single cells were binned into symbols averaging ~ 5 cells. In comparison to WT (black fit), mutations such as I[48]A, R[52]A, and R[52]Q (red symbols and fit) weakened $\text{Ca}^{2+}/\text{CaM}_{34}$ binding. **(b – f, right)** N-lobe CDI for NSCaTE mutants was characterized by co-expressing CaM_{34} (whole-cell Ca^{2+} currents in red, and Ba^{2+} currents in black). Indeed mutations that weaken $\text{Ca}^{2+}/\text{CaM}_{34}$ binding also disrupted N-lobe CDI.

Supplementary Note 10. Extended data for C-lobe CDI and NSCaTE

Analogous reasoning to that developed in Supplemental Note 8 furnishes the rationale for using a CaM_{12} FRET partner to test for a potential role of the NSCaTE as a C-lobe CDI effector site. Accordingly, the following FRET interaction curves and electrophysiological CDI results expand on the data arguing against the NSCaTE module as a C-lobe $\text{Ca}^{2+}/\text{CaM}$ effector site.

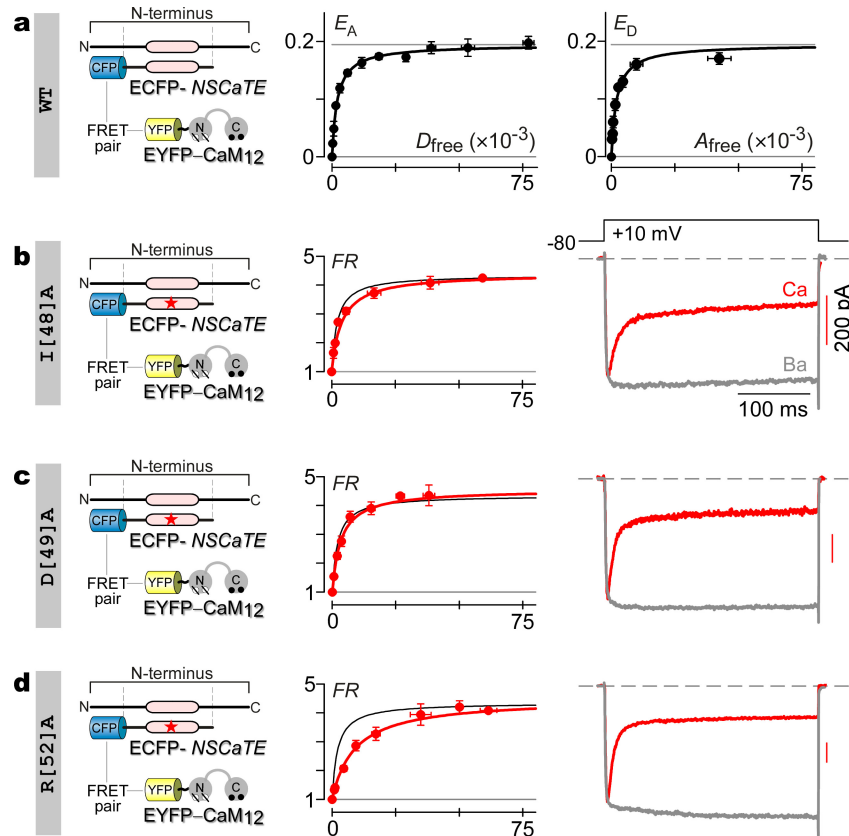


Figure S9. Extended analysis of NSCaTE element and C-lobe CDI. (a) FRET efficiencies between YFP- CaM_{12} and CFP-NSCaTE peptide measured by 3^3 -FRET and E-FRET metrics under elevated Ca^{2+} conditions. $E_A \sim E_D \sim 0.19$, suggesting a 1:1 binding stoichiometry. (b – d, left and middle) Changes in $K_{a,\text{EFF}}$ of NSCaTE binding to $\text{Ca}^{2+}/\text{CaM}_{12}$ are characterized by FRET 2-hybrid assay. WT fits from panel a (middle) reproduced in black. 3^3 -FRET ratios (FR) measured in single cells were binned into symbols averaging ~ 4 cells each, and fit to a 1:1 binding model (red fit). (b – d, right) Exemplar whole-cell currents for NSCaTE mutant channels with CaM_{12} coexpressed to isolate C-lobe form of CDI. Ca^{2+} currents are shown in red, and Ba^{2+} currents in black.

Supplementary Note 11. Rationale for FRET analysis of $\text{Ca}^{2+}/\text{CaM}$ interaction with PCI

For probing C-lobe CDI in relation to the PCI region, the prototypic FRET partner might have been $\text{Ca}^{2+}/\text{CaM}_{12}$, much in the way that analogous constructs were utilized in studying NSCaTE (Supplementary Note 8). However, the binding assays between PCI and $\text{Ca}^{2+}/\text{CaM}_{12}$ proved experimentally challenging.

Accordingly, we utilized $\text{Ca}^{2+}/\text{CaM}$ as the FRET partner with PCI, which yielded well-resolved binding curves. These curves can be understood within the context of iTL analysis as follows. The dominant binding events can be well approximated by a 2-state scheme as in Supplementary Fig. S5b. It follows that the aggregate affinity of FRET interaction is given by $K_T = K_C \cdot K_N \cdot \lambda$. PCI mutations are unlikely to change λ , an entity that mainly reflects CaM interlobe geometry as specified by its linker region. As we only undertook FRET characterization of PCI mutations that affected C-lobe CDI, we were likely investigating only those mutations that could potentially affect the C-lobe interface and K_C , rather than K_N . Importantly, the fold change in K_T produced by mutations, which we measured by FRET assays, would therefore be proportional to the fold-change in K_C , which is precisely the relevant entity for iTL analysis. As confirmation, FRET 2-hybrid experiments confirm that the C-lobe of $\text{Ca}^{2+}/\text{CaM}$ alone can bind to the PCI region (Supplementary Fig. S10, WT in black). Moreover, triple-alanine substitution of the LGF locus, which strongly diminished C-lobe CDI (main text Fig. 5c), also suppressed this binding interaction (Supplementary Fig. S10, LGF in red). Reassuringly, a similar disruption is observed for the binding of $\text{Ca}^{2+}/\text{CaM}$ (with both lobes) to the PCI region (main text Fig. 5d).

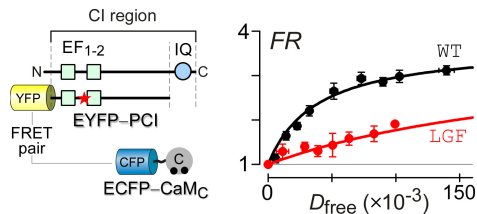


Figure S10. The C-lobe of $\text{Ca}^{2+}/\text{CaM}$ alone can bind to the PCI region. FRET ratio between YFP-tagged PCI region peptide and CFP-tagged C-lobe of CaM were measured using 3^3 -FRET. In comparison to WT, triple alanine substitution at the LGF locus significantly weakened this binding interaction.

Supplementary Note 12. Extended electrophysiological and binding data for PCI hotspots

Biochemical and structural studies of the PCI region of the homologous $\text{Ca}_v1.2$ channels point to the possibility of multiple $\text{Ca}^{2+}/\text{CaMs}$ binding to this segment^{36,37}. To exclude this possibility, we probed for FRET between YFP- CaM_{WT} and CFP- CaM_{WT} in the presence of a PCI segment, all under conditions of elevated cytosolic Ca^{2+} . If multiple CaMs could bind to the PCI region, we would expect these CaMs to be in sufficient proximity to permit FRET between the attached fluorophores. In contrast, we observed no FRET between the two CaMs, suggesting that only one $\text{Ca}^{2+}/\text{CaM}$ can bind to the PCI region. In the PCI segment here, a fluorescently inert analog of YFP (Amber⁶⁸) was precisely substituted into the EYFP-PCI construct used in main text Fig. 3g (left), so as to closely mimic the configuration used for EYFP-PCI versus ECFP- CaM_{WT} FRET experiments.

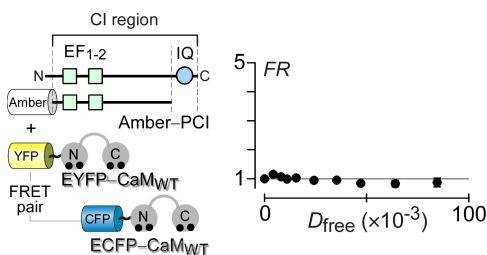


Figure S11. Establishing 1:1 stoichiometry of binding between $\text{Ca}^{2+}/\text{CaM}$ and PCI region peptide. To test whether multiple CaM molecules may bind to PCI region, we probed for FRET between YFP- and CFP-tagged CaM in presence of PCI region, all under elevated Ca^{2+} conditions. The fluorophore on the PCI region peptide was mutated to be non-fluorescent (Amber).

Supplementary Fig. S12 explicitly elaborates upon binding and electrophysiological data arguing that the PCI serves as an effector site of the C-lobe of $\text{Ca}^{2+}/\text{CaM}$, but not the N-lobe.

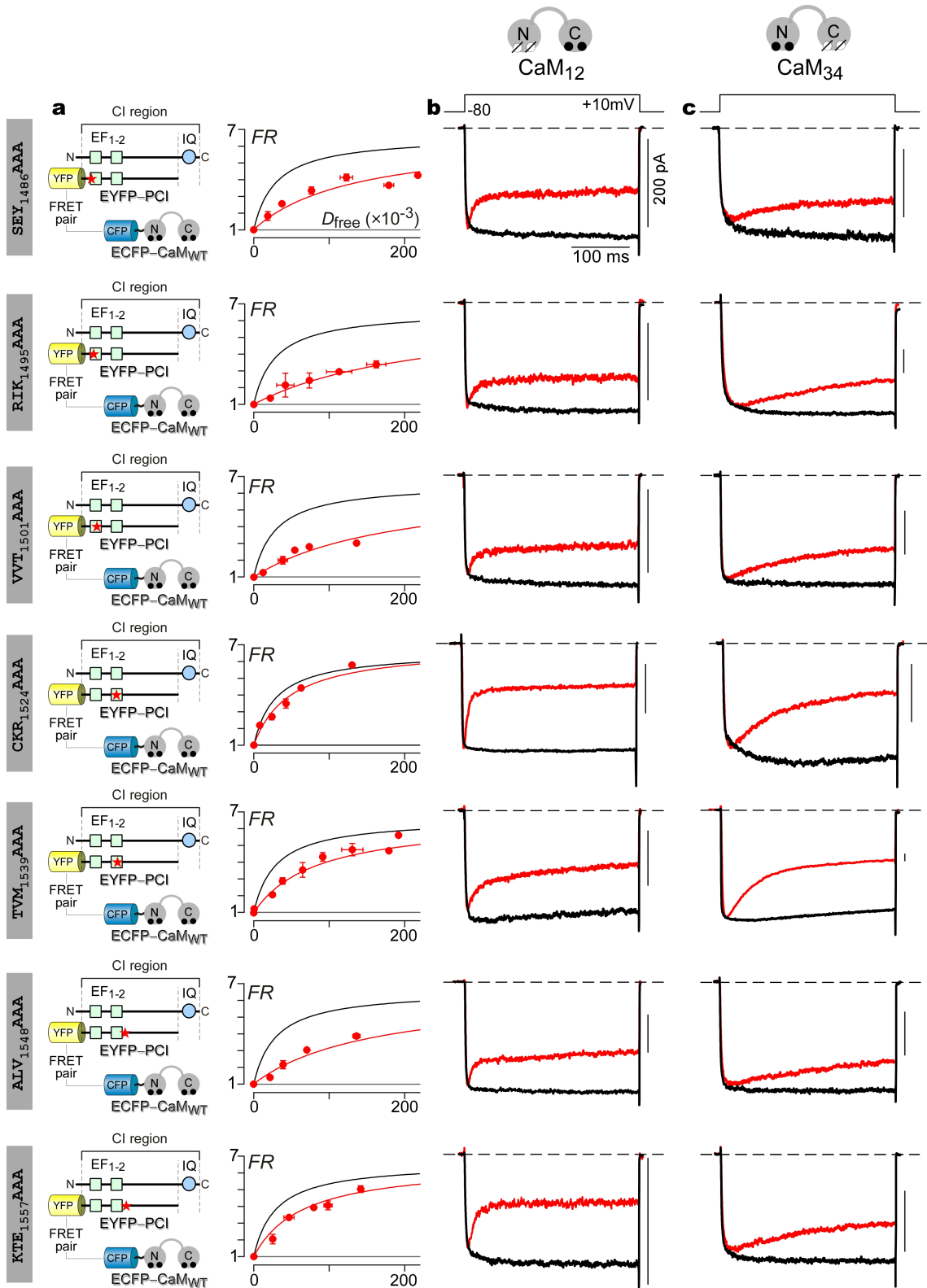


Figure S12. Extended analysis of PCI region as C-lobe $\text{Ca}^{2+}/\text{CaM}$ effector site. (a) FRET 2-hybrid assay used to systematically characterize changes in $K_{a,\text{EFF}}$ of $\text{Ca}^{2+}/\text{CaM}$ binding to mutant PCI region (red star). For reference, fits for wild-type YFP-PCI peptide binding to $\text{Ca}^{2+}/\text{CaM}$ is reproduced in black from main text Fig. 5d. For each construct, 3^3 -FRET ratios measured from single cells were binned into symbols averaging ~ 5 cells (red circles). (b) For each mutation, C-lobe CDI was characterized by co-expressing CaM_{12} with mutant $\text{Ca}_v1.3$ channels. Whole-cell Ca^{2+} currents in red, Ba^{2+} currents in black. In comparison to wild-type channels (main text Fig. 1d), mutations in PCI region disrupt C-lobe CDI. (c) Whole-cell currents from mutant channels coexpressed with CaM_{34} showed no appreciable deficit in N-lobe CDI; format as in b.

Supplementary Note 13. Dependence of IQ/PCI interaction on $\text{Ca}^{2+}/\text{CaM}$

The binding interaction between IQ domain and PCI region (main text Fig. 6d) was found to be strongly dependent on cytosolic Ca^{2+} . Before we explore the origin of this Ca^{2+} -dependence, we note that the PCI region of Ca_V and Na_V channels contain two vestigial EF-hand domains. However, the ability of these EF-hands to coordinate Ca^{2+} ions remains controversial^{69,70}. In $\text{Ca}_V1.2$ channels, these EF-hands have been argued to be incapable of binding Ca^{2+} ions^{71,72}. An alternative possibility is that $\text{Ca}^{2+}/\text{CaM}$ could mediate the IQ/PCI binding interaction, thus forming a tripartite complex. If so, depletion of free $\text{Ca}^{2+}/\text{CaM}$ by co-expressing a CaM ‘sponge’ would inhibit the IQ/PCI interaction. Indeed, using FRET 2-hybrid assays, we found that co-expression of a $\text{Ca}^{2+}/\text{CaM}$ chelator (the IQ domain from neuromodulin²⁰) significantly weakened the IQ/PCI interaction of $\text{Ca}_V1.3$ channels.

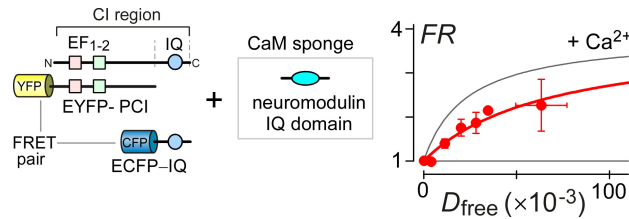


Figure S13. Origin of Ca^{2+} -dependence for IQ/PCI interaction. Left, FRET 2-hybrid assay probing Ca^{2+} -dependent interaction between IQ domain and PCI segment. Right, For reference, the black fit shows binding curve for IQ/PCI binding in presence of Ca^{2+} , as reproduced from main text Fig 6d. Coexpression of a $\text{Ca}^{2+}/\text{CaM}$ chelator, the IQ domain of neuromodulin, significantly weakened this interaction (red symbols and fit). This weakening is fully consistent with $\text{Ca}^{2+}/\text{CaM}$ facilitating the Ca^{2+} -dependence of IQ/PCI interaction. 3³-FRET measured from single cells were binned into symbols averaging ~ 6 cells each.

Supplementary Note 14. Extended data for IQ interaction with PCI.

Main text Figure 6b shows that various mutations within the IQ domain attenuate C-lobe CDI. Here, we furnish FRET 2-hybrid analysis substantiating altered Ca^{2+} -dependent binding between the IQ and PCI domains, upon introduction of corresponding mutations.

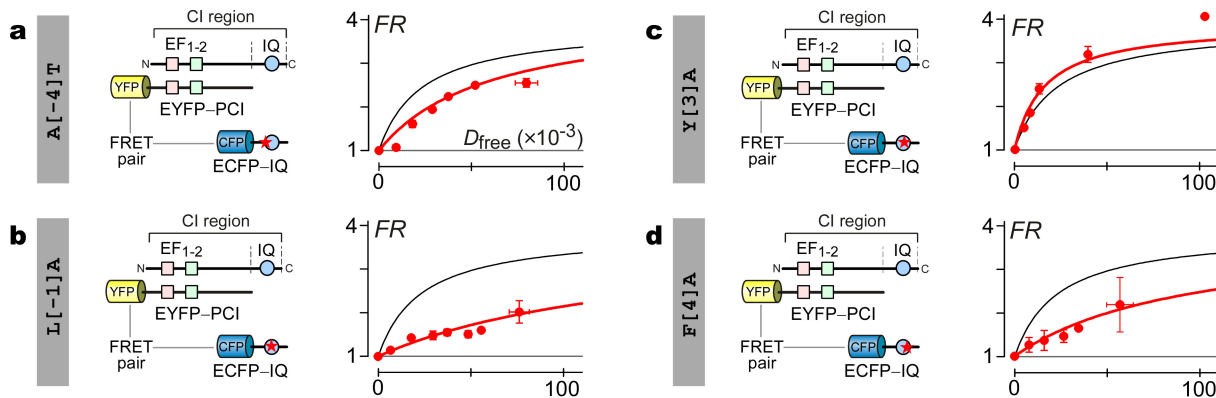


Figure S14. Extended binding analysis of effects of IQ-domain mutations on IQ/PCI interaction. (a – d) FRET 2-hybrid assays probe interaction between IQ domain and PCI segment under elevated Ca^{2+} conditions for various IQ domain mutants. Symbols average FRET measurements from ~ 4 cells each. In comparison to the wild-type IQ domain (black fit), mutations like A[-4]T (a), L[-1]A (b), and F[4]A (d) weakened IQ/PCI interaction in accord with diminished C-lobe CDI in these mutants (main text Fig. 6b). In contrast, the mutation Y[3]A resulted in a slight increase in the binding affinity (c), rationalizing in this case the slight increase in C-lobe CDI (main text Fig. 6b). FRET data were fit (red curves) with the same maximal FRET efficiencies ($FR_{\text{max}} = 3.9$).

Supplementary Note 15. Explicit Langmuir form for IQ interaction with PCI

To formulate concretely the Langmuir equation for the IQ interaction with the complex of the C-lobe of $\text{Ca}^{2+}/\text{CaM}$ with the PCI domain, we start with the reaction scheme in Supplementary Fig. S1b in Supplementary Note 1. Instead of forming the Langmuir equation on γ_1 as done in Supplementary Note 1, we here formulate the Langmuir equation on γ_2 , corresponding to the IQ/PCI binding step. This procedure yields

$$CDI / CDI_{\max} = \frac{K_{a,\text{EFF}}}{K_{a,\text{EFF}} + \underbrace{\frac{1 + (1/\varepsilon) + (1/\varepsilon) \cdot (P_O \cdot C_{\text{spike}}^2 \cdot k_{\text{on}} / k_{\text{off}}) + (1/\varepsilon) \cdot (P_O \cdot C_{\text{spike}}^2 \cdot k_{\text{on}} / k_{\text{off}}) \cdot \gamma_1}{s \cdot (1/\varepsilon) \cdot (P_O \cdot C_{\text{spike}}^2 \cdot k_{\text{on}} / k_{\text{off}}) \cdot \gamma_1}}}_{\lambda}} \quad (\text{S11})$$

where P_O is the channel open probability, CDI_{\max} is the CDI strength that would be observed if $K_{a,\text{EFF}}$ were to become infinite, C_{spike} is the free nanodomain Ca^{2+} concentration at the indwelling CaM during a channel opening (\sim always constant and the same during openings), and other terms are given in main text Fig. 2a and Eq. 1 (where $\gamma_2 = s \cdot K_a$, and s is a constant of proportionality).

Supplementary Note 16. Extended data for apoCaM interaction with CI module

The PCI region harbors novel apoCaM preassociation sites. Alanine substitutions at such loci may weaken apoCaM binding to channels, leading to decreased CDI under endogenous levels of CaM. FRET 2-hybrid analysis of the FRET pairs CFP–CaM and YFP–CI region explicitly demonstrates this decreased apoCaM binding affinity (Supplementary Figs. S15a and S16a) for several mutations in the PCI region. Whole-cell exemplar currents for channel bearing these mutations depict a corresponding loss in CDI under endogenous levels of CaM (Supplementary Figs. S15b and S16b). Overexpressing CaM_{WT} rescues CDI (Supplementary Figs. S15c and S16c) for these mutants, confirming apoCaM preassociation at these sites.

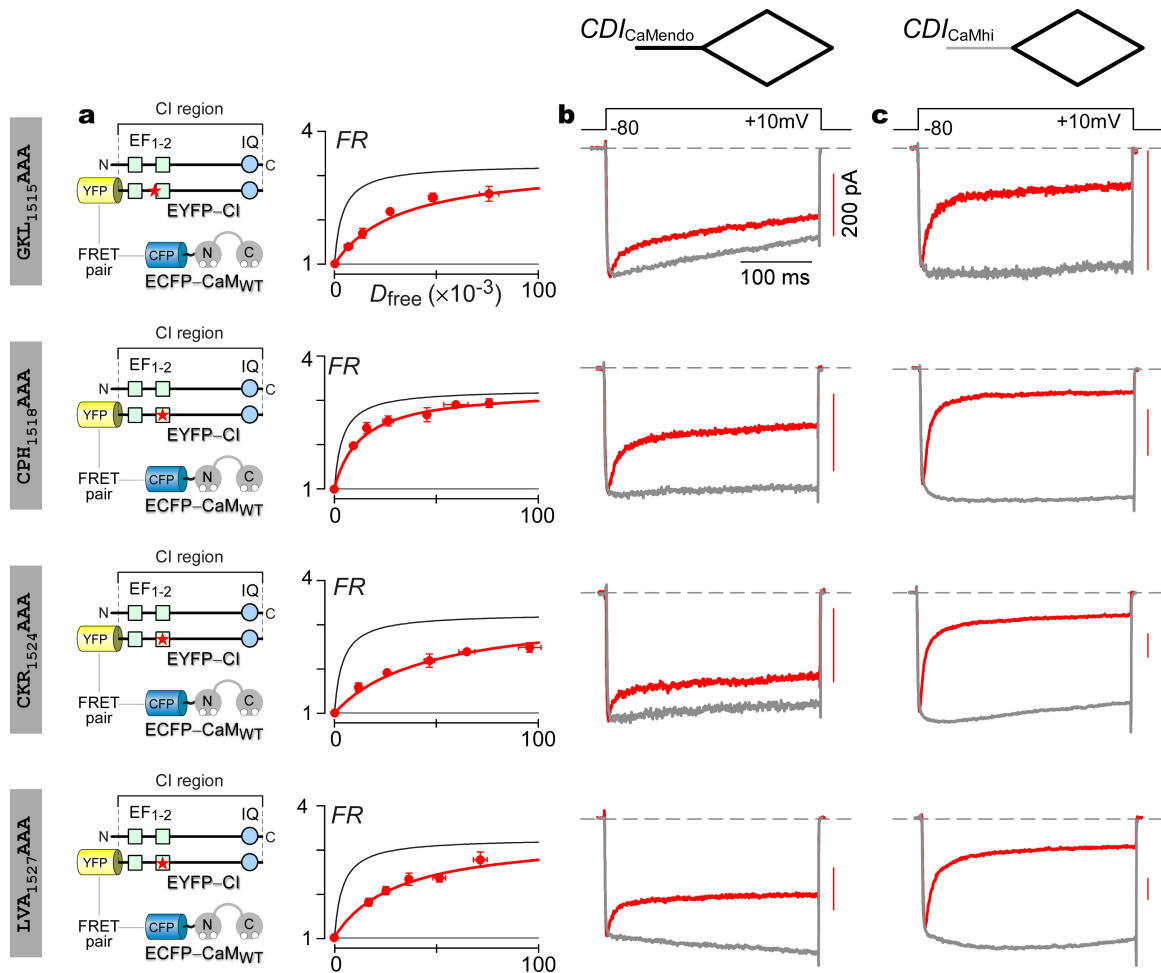


Figure S15. Extended analysis of PCI region as an apoCaM pre-association site, with further data display below in next figure. (a) FRET 2-hybrid assay systematically characterizes effects of PCI-region mutations (red star) on $K_{a,EFF}$ of apoCaM binding to the CI region. For reference, fits for wild-type YFP-CI region binding to CFP-apoCaM (main text Fig. 7d) are reproduced in gray. For each construct, 3FRET ratios measured from single cells were binned into symbols averaging ~ 5 cells each (red circles). (b) Exemplar whole-cell currents from HEK293 cells expressing mutant channels are shown. Note that cells contained only endogenous levels of apoCaM. (c) Overexpression of CaM_{WT} rescued CDI in channels with weakened apoCaM preassociation, arguing that the PCI segment harbors functionally relevant apoCaM preassociation sites.

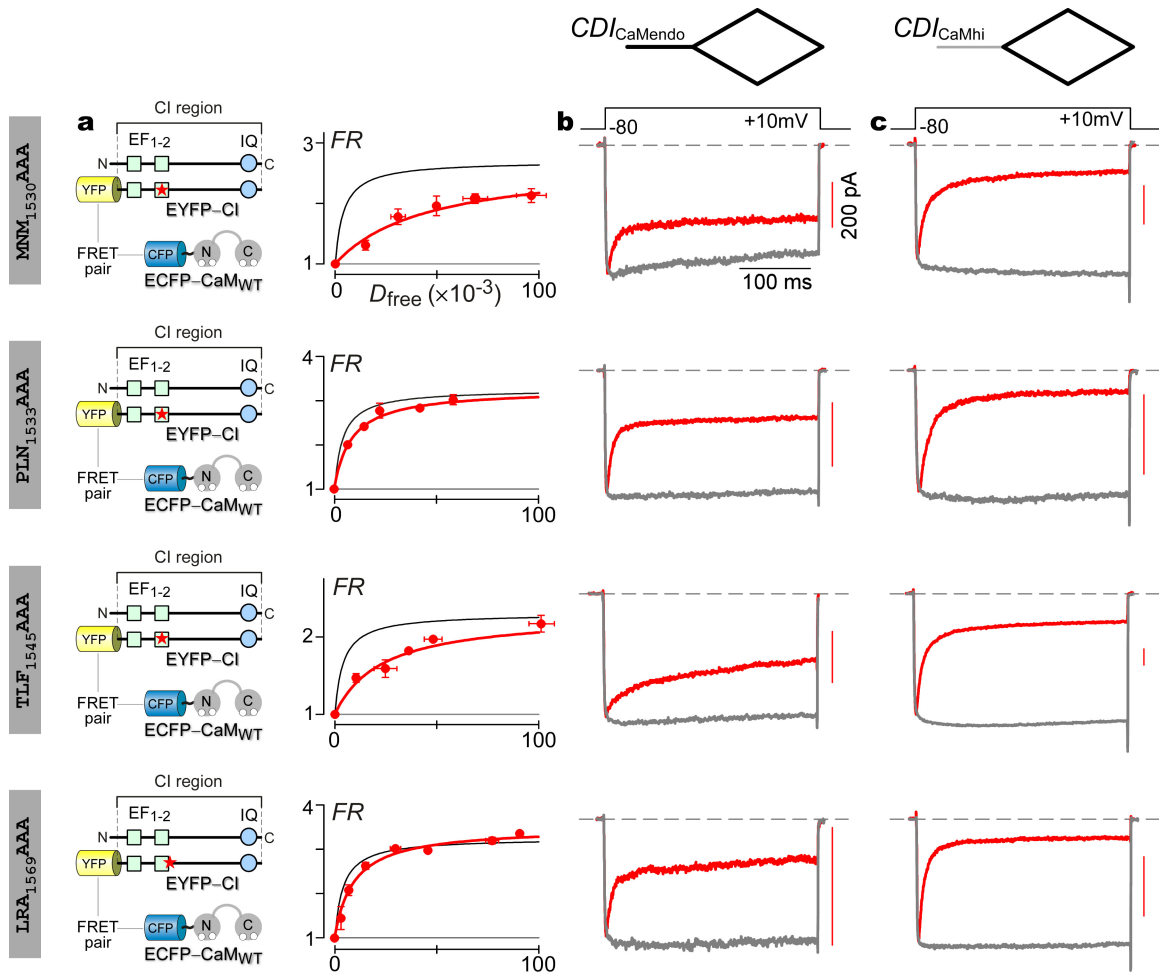


Figure S16. Additional exemplars confirming that PCI region harbors functionally relevant apoCaM preassociation sites. Format as in Supplementary Fig. S15.

Supplementary Note 17. Rationale for FRET constructs for apoCaM versus CI interaction

Before entertaining detailed considerations of apoCaM interaction with the CI region, we confirmed a simple 1:1 stoichiometry of binding, utilizing two methods. In the first, we utilized the equivalence of $E_{A,max}$ and $E_{D,max}$ (plateau levels for FRET 2-hybrid binding curves obtained by 3^3 -FRET and E-FRET analysis, Supplementary Fig. S17a). In the second approach, we substituted a non-fluorescent analog of YFP (Amber⁶⁸) into our initial YFP-CI FRET pair. We then tested for FRET between YFP-CaM_{WT} and

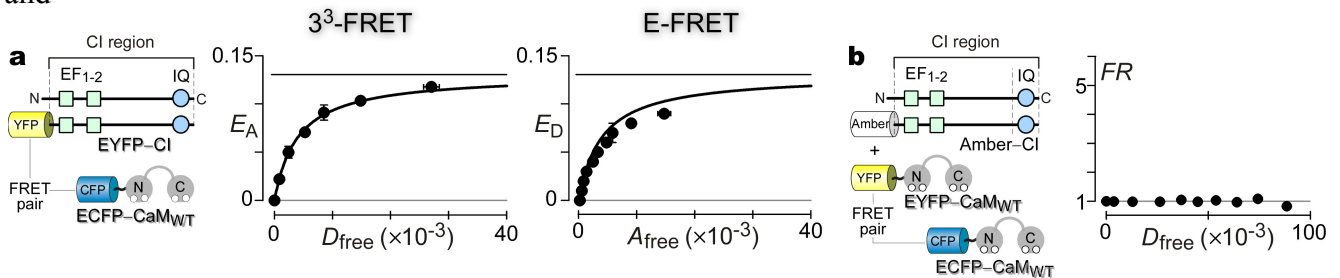


Figure S17. Single apoCaM binds to channel CI region. (a) FRET efficiencies between CFP-CaM and YFP-CI peptide (cartoon at left) measured by 3^3 -FRET (middle) and E-FRET (right) metrics. $E_{A,max} \sim E_{D,max} \sim 0.13$, arguing for 1:1 binding stoichiometry. (b) As an added test, we tested for FRET between YFP-CaM and CFP-CaM, both in the presence of non-fluorescent CI region. No FRET was detected, further substantiating a 1:1 stoichiometry of apoCaM binding to CI region.

CFP–CaM_{WT}, both in the presence of Amber-CI. If more than one CaM could bind the CI region, it is likely that some FRET would be detected. However, experiments revealed no appreciable FRET (Supplementary Fig. S17b), again supporting a 1:1 stoichiometry of apoCaM binding to the CI region.

The binding of apoCaM to the CI region may be conceptualized by the same scheme as shown in Fig. S5a, here with all species applying to the interaction with apoCaM rather than Ca²⁺/CaM. By the same logic, the aggregate process of apoCaM preassociation with the CI binding reaction can be well approximated by an analog to the two-state scheme in Fig. S5b, where the total forward equilibrium constant for the reaction would now become $\varepsilon_T = \varepsilon_C \cdot \varepsilon_N \cdot \lambda$, where ε_T is measured in FRET assays, ε_C and ε_N are forward equilibrium constants for initial CI interaction with C- or N-lobe of apoCaM, respectively; and λ is a cooperativity factor having much to do with the linker geometry between lobes of apoCaM. Similarly, the respective binding energy terms are given by $\Delta G_T = \Delta G_C + \Delta G_N + \Delta G_{CN}$, where the subscripts now refer to lobes of apoCaM. As CI mutations are unlikely to perturb something related to apoCaM linker geometry like λ , these mutations probably affect ε_C or ε_N alone, depending upon whether the mutation occurs at a C- or N-lobe contact point. That said, mutation-induced, fold changes in ε_T likely equal to fold changes in ε_C or ε_N .

Supplementary Note 18. Explicit Langmuir form for apoCaM interaction with channel CI region

For purposes of deducing the Langmuir form of CDI dependence upon channel affinity for apoCaM, a variant configuration of iTL analysis must be considered. For concreteness we start with the 5-state model in Fig. S1b. Because the exchange of apoCaM with the channel is slow²⁴, (≥ 10 s of secs) most of the exchange occurs while intracellular Ca²⁺ is exceedingly low, during 20-30 second rest periods between brief depolarizing pulses with 10 mM BAPTA as intracellular dialyzate. Accordingly, for purposes of deducing the fraction of channels with apoCaM preassociated, we need only consider bulk exchange with states 1 and 2 (relevant to Ca²⁺-free conditions) of the 5-state model. This yields the configuration shown in Fig. S18 below, where state 2' is a channel lacking CaM in its alcove; ε is an aggregate entity equal to $\varepsilon_{N\text{-lobe}} \cdot \varepsilon_{C\text{-lobe}} \cdot \lambda$ from above; and C_{bulk} is the concentration of free apoCaM in bulk cytoplasm. Note that there is no meaning to an interconnection between states 1 and 2' because a channel can only directly release apoCaM into its alcove.

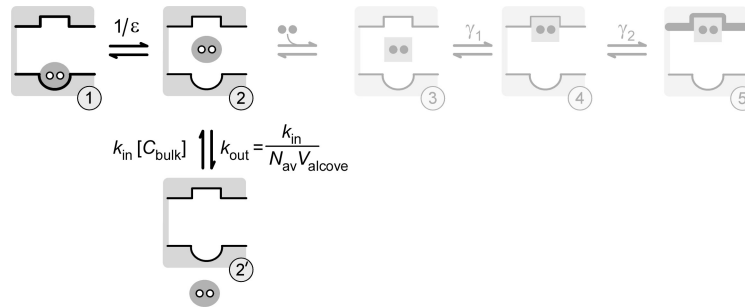


Figure S18. Model configuration for understanding exchange of apoCaM with channels. Since, apoCaM preassociation occurs under Ca²⁺-free conditions, we consider only states 1 and 2 in our 5-state model. To account for exchange of apoCaM from cytosol into the alcove of a Ca_v channel, we introduce a new state 2' where apoCaM resides outside the channel alcove. Here, the rate constants k_{in} and k_{out} will account for diffusion of apoCaM. N_{av} , Avogadro's number. V_{alcove} , effective volume of channel alcove for apoCaM.

Based on this configuration, it is straightforward to calculate the equilibrium value for the fraction of channels with onboard CaM, which turns out to equal:

$$F_{\text{bound}} = \Pr\{\text{state 1}\} + \Pr\{\text{state 2}\} = \frac{\varepsilon}{\varepsilon + 1 + k_{\text{out}}/k_{\text{in}} \cdot [C_{\text{bulk}}]} + \frac{1}{\varepsilon + 1 + k_{\text{out}}/k_{\text{in}} \cdot [C_{\text{bulk}}]} \quad (\text{S12})$$

When $\varepsilon \rightarrow 0$, channels exhibit negligible CDI as observed experimentally in our previous publication²⁰. Hence, it must be that

$$0 \sim \lim_{\varepsilon \rightarrow \infty} F_{\text{bound}} = \frac{1}{1 + k_{\text{out}}/k_{\text{in}} \cdot [C_{\text{bulk}}]} \Rightarrow k_{\text{out}}/k_{\text{in}} \cdot [C_{\text{bulk}}] \gg 1 \quad (\text{S13})$$

With this knowledge, we obtain the simplified Langmuir form

$$F_{\text{bound}} \sim \frac{\varepsilon}{\varepsilon + k_{\text{out}} / (k_{\text{in}} \cdot [C_{\text{bulk}}])} \quad (\text{S14})$$

In the main text, we can experimentally gauge F_{bound} for a given construct by measuring CDI strength with only endogenous CaM present (CDI_{CaMendo} , seen with control levels of $[apoCaM_{\text{bulk}}]$), and normalizing by CDI strength measured during CaM_{WT} overexpression with the same construct (CDI_{CaMhigh}). By performing this normalization, the metric $CDI_{\text{CaMendo}} / CDI_{\text{CaMhi}}$ approximates F_{bound} , even though changes in ε for a given construct could in principle change the absolute strength of CDI.

Supplementary Note 19. *De novo* prediction of CI region structures

The structural correlates for the molecular states we have identified here have yet to be determined. Nonetheless, to evaluate the structural plausibility of these states, we turn to *de novo* structural prediction using *Rosetta*⁵². We used the *Robetta* online server (<http://robetta.bakerlab.org>), to obtain plausible molecular models of the CI region spanning GPH_{1474} (in the PCI region) through residue K_{1620} in the IQ domain⁵². Supplementary Fig. S19 displays the top 5 predicted models furnished by the server. Coarsely, the IQ domain (blue) is linked to the PCI segment (green) through a flexible linker, and thus adopts variable orientations. The PreIQ region forms a distinctive uninterrupted helix, similar to that observed in crystal structures of the homologous region in $Ca_v1.2$ channels ($3OXQ^{28}$ and $3G43^{29}$). The EF-hand region in model I is structurally similar to homologous segments of Na_v channels, namely EF-hand-like domains ($2KBI^{50}$ or $2KAV^{51}$). In general, the EF-hand region adopted either a closed conformation reminiscent of N-lobe of apoCaM (models I & IV), or an open conformation like the N-lobe of Ca^{2+}/CaM (models II, III, or V). For subsequent docking simulations, we focused on models I and III, representing the two best respective closed and open conformations identified by *Rosetta*.

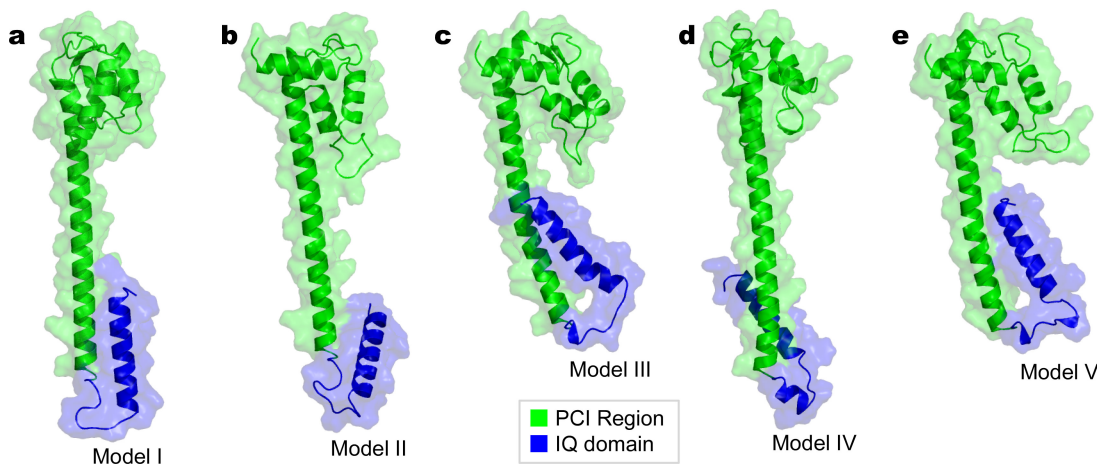


Figure S19. (a–e) *De novo* structural prediction of $Ca_v1.3$ CI region. Models I–V are top models outputted from the *Robetta* online server. The PCI segment was shaded in green. The IQ domain is shaded in blue.

Supplementary Note 20. Docking of apoCaM to CI region

To build a molecular model of apoCaM bound to the CI region of $Ca_v1.3$ channels, we drew upon insight from recent structural studies of the homologous Na_v channel CI region. Firstly, a crystallographic structure of the $Na_v1.5$ CI region, complexed with apoCaM and FGF13, shows that the EF-hand-like domain of these channels adopts a closed conformation with high structural similarity to model I of our predictions⁵⁶ (Supplementary Fig S19). Secondly, multiple structures have demonstrated that the IQ domain of these channels bind to the C-lobe of apoCaM^{41,42,56}. Thirdly, the N-lobe of apoCaM in these latter Na_v structures seem to adopt variable conformations. At the same

time, our own functional studies of Ca_v1.3 channels point to the N-lobe of apoCaM binding to the downstream EF-hand segment of the PCI region (EF₂).

That said, we incorporated these trends into the development of a custom multi-step docking algorithm to model apoCaM interaction with the Ca_v1.3 carboxy terminus (main text Fig. 8b). To do so, we first used MODELLER⁷³ to build a homology model of the Ca_v1.3 IQ domain interaction with the C-lobe of apoCaM, based on the NMR structures of Na_v1.5⁴¹ and Na_v1.2⁴² IQ domains complexed with the C-lobe of apoCaM. Reassuringly, this model of the Ca_v1.3 IQ domain emphasizes contacts at the functionally relevant hotspots A[-4], I[0], and F[4] in the IQ domain (f, Fig. 8b). Next, we utilized a shape complementarity docking algorithm, PatchDock⁵³, to coarsely dock the N-lobe of apoCaM (1CFD) to the PCI region, as suggested from our iTL analysis. The top ten resulting docking models were then refined by FireDock⁵⁹. We then turned to RosettaDock and Loop refinement protocols of the PyRosetta⁶⁰ package to perform high-resolution docking of the N-lobe to the PCI segment. Out of 8000 decoys generated using PyRosetta, we identified the lowest energy complex as our top model. To combine these distinct structural models (PCI region bound to the N-lobe of apoCaM, and IQ domain bound to the C-lobe of apoCaM), we used PyRosetta to develop a custom minimization and refinement protocol, as follows. We optimized the position of the IQ domain/C-lobe apoCaM complex with respect to the PCI region by altering the conformation of the linker between N- and C-lobes of apoCaM, and simultaneously minimizing both the energetics and distance between the IQ domain and QVV₁₅₉₀ in the PreIQ region. Finally, the flexible linker between the PreIQ segment and the IQ domain was built and optimized via multiple rounds of energy minimization.

Supplementary Note 21. Enhanced N-lobe CDI with decreased channel affinity for the N-lobe of apoCaM

From Equation S1 of Supplementary Note 1, the steady-state strength of N-lobe CDI can indeed be influenced by decreases in ε (to be precise, ε for the N-lobe). Specifically, as ε decreases, so too does Λ (Eq. S1). Thus, all things being equal, N-lobe CDI should be enhanced. Such enhancement in CDI maybe observed in N-lobe CDI of TVM₁₅₃₉AAA mutant in Supplementary Fig. S12.

Supplementary Note 22. Docking of C-lobe of Ca²⁺/CaM to CI region

To build a structural model of the tripartite C-lobe CDI effector complex (IQ/PCI/C-lobe Ca²⁺/CaM in main text Fig. 8c, right), we employed a custom, multi-step docking algorithm similar to the one above. As the starting point for the PCI segment, we chose model III (Supplementary Fig. S19) because its open EF-hand conformation permitted simultaneous interactions with the IQ segment and the C-lobe of Ca²⁺/CaM (3BXL). First, we used PatchDock⁵³ to obtain a coarse model of the IQ domain bound to the EF-hand segments of Ca_v1.3 channels. Subsequently, we refined this model initially with FireDock, and then with the RosettaDock protocol of PyRosetta for a systematic second stage of refinement. Next, we coarsely docked the structure of the C-lobe of Ca²⁺/CaM to the above complex using PatchDock, followed by structural refinement with FireDock⁵⁹ and RosettaDock⁵³. Finally, we optimized the conformation of the flexible PreIQ-IQ linker using PyRosetta⁶⁰. These molecular models highlight the structural plausibility of the functionally relevant molecular states that we have identified.

Supplementary Note 23. Aggregate association constant for IQ–PCI–Ca²⁺/CaM tripartite complex

Binding studies of the Ca_v1.2 channel IQ domain have reported a high Ca²⁺/CaM affinity (e.g., ~50 nM in main text Fig. 3c, giving reason to wonder how CaM, already preassociated with the IQ domain (Supplementary Fig. S20, state 1), could ever leave upon Ca²⁺ binding. To address this concern, we reconsider the state transition diagram from Supplementary Fig. S1b, but with the PCI/IQ interaction explicitly represented in state 5, and with a state 6 where Ca²⁺/CaM could potentially rebind to the IQ domain (Supplementary Fig. S20).

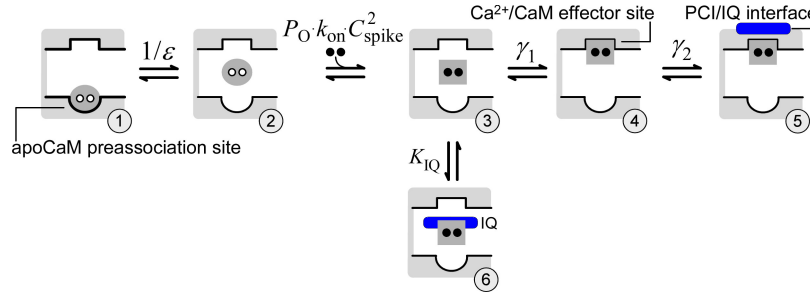


Figure S20. Estimating the propensity of Ca²⁺/CaM to leave the IQ domain. We add an additional state (state 6) to the reaction diagram of Supplementary Fig. S1b, where the IQ domain can potentially rebind Ca²⁺/CaM. K_{IQ} , association constant for IQ domain binding to Ca²⁺/CaM. To study the possibility of CaM departing from the IQ domain, we consider the probability of occupying state 5 versus state 6.

The propensity of Ca²⁺/CaM to reside in the tripartite complex (state 5, IQ–PCI–Ca²⁺/CaM) versus the IQ–Ca²⁺/CaM configuration (state 6) can be estimated as:

$$\frac{\Pr\{\text{state 5}\}}{\Pr\{\text{state 6}\}} = \frac{\gamma_1 \cdot \gamma_2 \cdot \Pr\{\text{state 3}\}}{K_{IQ} \cdot \Pr\{\text{state 3}\}} = \frac{\gamma_1 \cdot \gamma_2}{K_{IQ}} \quad (\text{S15})$$

It turns out that the *product* of equilibrium constants in the numerator of this expression renders this ratio far greater than unity, as follows. Given that Ca²⁺/CaM resides within the alcove of the channel (Supplementary Note 18), the equilibrium constants γ_1 and K_{IQ} includes the local concentration of Ca²⁺/CaM, as given by:

$$\begin{aligned} \gamma_1 &= \hat{\gamma}_1 \cdot [\text{Ca}^{2+}/\text{CaM}]_{\text{local}} \\ K_{IQ} &= \hat{K}_{IQ} \cdot [\text{Ca}^{2+}/\text{CaM}]_{\text{local}} \end{aligned} \quad (\text{S16})$$

The redefined constants $\hat{\gamma}_1$ and \hat{K}_{IQ} are proportional to the relative association constants estimated in our FRET 2-hybrid assays (main text Fig. 4d and Fig. 3c, respectively).

Substituting these relations into Equation S15,

$$\frac{\Pr\{\text{state 5}\}}{\Pr\{\text{state 6}\}} = \frac{\hat{\gamma}_1 \cdot [\text{Ca}^{2+}/\text{CaM}]_{\text{local}} \cdot \gamma_2}{\hat{K}_{IQ} \cdot [\text{Ca}^{2+}/\text{CaM}]_{\text{local}}} = \frac{\hat{\gamma}_1 \cdot \gamma_2}{\hat{K}_{IQ}} \quad (\text{S17})$$

Given that a single calmodulin resides in the alcove of the channel, and the intramolecular proximity of the IQ and PCI domains, the local concentration of CaM near these domains would be approximately equal. This simplification allows us to cancel out local concentration terms in numerator and denominator, yielding the rightmost expression in Equation S17.

Lastly, the transition between states 4 and 5 is an intramolecular reaction. As such, estimating the equilibrium constant γ_2 requires deduction of the entropic factors associated with this transition. One approach⁷⁴ is to represent γ_2 as:

$$\gamma_2 = \hat{\gamma}_2 \cdot [\text{IQ}]_{\text{local}} \quad (\text{S18})$$

Here, $\hat{\gamma}_2$ is proportional to the association constant estimated from our FRET 2-hybrid assay from main text Fig. 4d, and $[\text{IQ}]_{\text{local}}$ is the local concentration of the IQ domain near the PCI segment.

$$\frac{\Pr\{\text{state 5}\}}{\Pr\{\text{state 6}\}} = \frac{\hat{\gamma}_1 \cdot \hat{\gamma}_2 \cdot [\text{IQ}]_{\text{local}}}{\hat{K}_{IQ}} \quad (\text{S19})$$

A first-order approximation for the concentration $[\text{IQ}]_{\text{local}}$ is given by:

$$[\text{IQ}]_{\text{local}} = \frac{1}{N_{\text{Avogadro}} \cdot V_{\text{local, IQ}}} \quad (\text{S20})$$

From our molecular model in main text Fig. 8b, we estimate a maximal distance of 45 Å between the IQ and PCI domains, resulting in $[\text{IQ}]_{\text{local}} \sim 4.4 \text{ mM}$ ($1.36 \times 10^8 D_{\text{free}}$ units). Thus, we can compute the value of Equation S19 numerically as:

$$\frac{\text{Pr}\{\text{state 5}\}}{\text{Pr}\{\text{state 6}\}} = \frac{\hat{\gamma}_1 \cdot \hat{\gamma}_2 \cdot [\text{IQ}]_{\text{local}}}{\hat{K}_{\text{IQ}}} = \frac{(3.45 \times 10^{-5} D_{\text{free}}^{-1})(4.35 \times 10^{-5} D_{\text{free}}^{-1})(1.36 \times 10^8 D_{\text{free}})}{5.9 \times 10^{-4} D_{\text{free}}^{-1}} \approx 350 \quad (\text{S21})$$

Thus by thermodynamic reasoning, the formation of the C-lobe CDI effector complex (state 5) is far more likely than simple binding of the IQ domain to $\text{Ca}^{2+}/\text{CaM}$, despite the high affinity of the latter. This outcome underscores the plausibility of switching CaM interactions as the mechanistic basis for CDI.

Importantly, nature and drug design exploit such enhancement of binding affinity through multivalent ligand mechanisms^{54,74}. Empirically speaking, the improvement in binding may involve far larger local concentrations (10^2 - 10^5 M versus our 4.4 mM estimate) such as seen in peptide-elastase interactions⁷⁵ and succinic anhydride formation⁷⁶. Thus, our coarse estimate of a 4.4 mM local concentration (Equation S20) could well understate the actual propensity for tripartite complex formation (Supplementary Fig. S20, state 5). Of note, in ITC calorimetry studies of single lobes of $\text{Ca}^{2+}/\text{CaM}$ binding to the $\text{Ca}_v1.2$ IQ domain, even higher affinities of 2 nM have been reported for the C-lobe²⁹. Even so, formation of the tripartite complex formation (Supplementary Fig. S20, state 5) would still be favored by a factor of ~ 15 . More relevant may be the conditions under which the ITC calorimetry experiments were conducted. To aid solubility of the IQ domain, low salt concentrations (5 mM KCl) were employed. However, it has been found that low-ionic-strength conditions artificially increase $\text{Ca}^{2+}/\text{CaM}$ binding to P-57 protein⁷⁷. Even greater low-salt enhancement has been found for the interaction of single lobes of $\text{Ca}^{2+}/\text{CaM}$ to IQ domains of myosin V⁷⁸. Under physiological salt concentrations, then, one might still expect that a boost factor ~ 350 would hold true (Equation S21).

Supplementary Note 24. Design and characterization of FRET 2-hybrid interaction pairs

For FRET 2-hybrid assays of functional CaM/channel interactions, various channel segments were tagged with YFP or CFP fluorophores on their amino termini. The design for such peptides is depicted in Supplementary Fig. S21a. Briefly, the NSCaTE segment was composed of residues 35-94 of Ca_v1.3 channels, including the signature 'WxxxIxxxR' sequence. The CI region was defined as the channel carboxy-terminal segment, starting downstream of domain IV S6, and including the IQ domain (residues 1459-1626). The CI segment was subdivided into PCI (residues 1459-1589) and IQ domain (1590-1626).

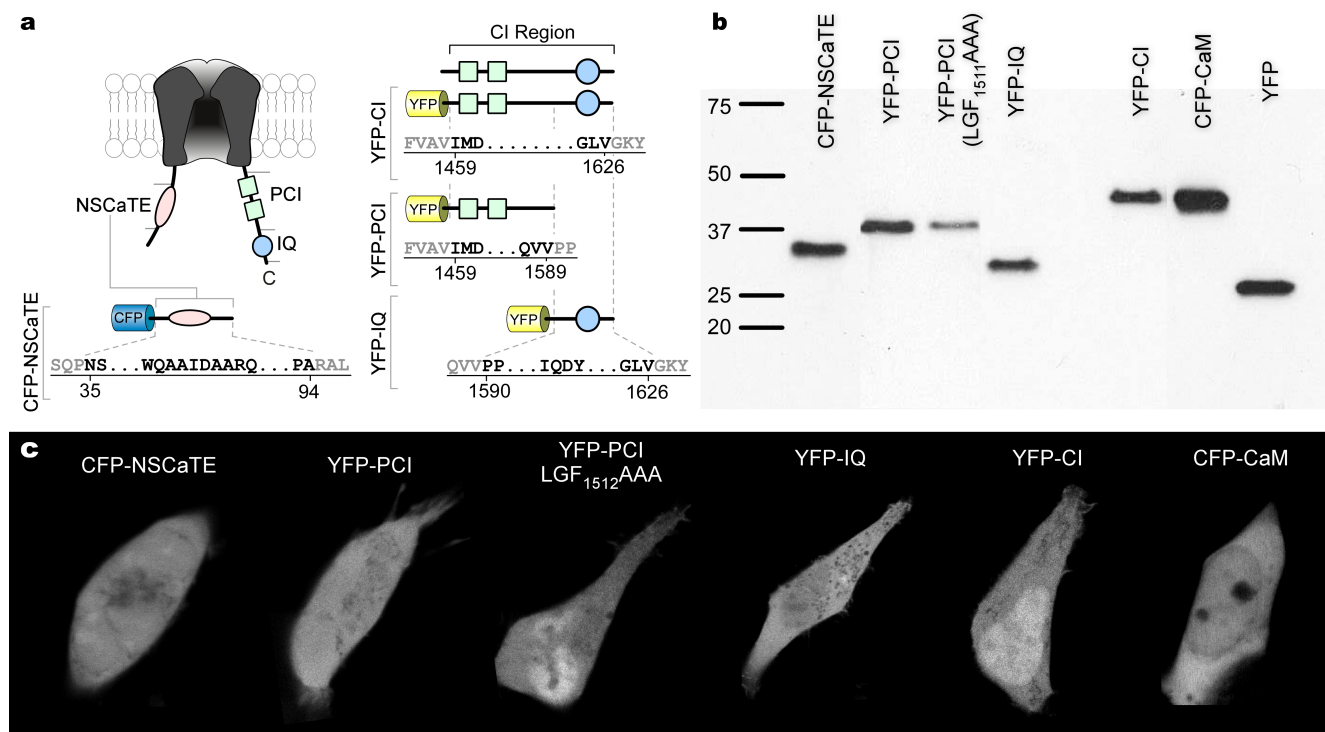


Figure S21. Robust expression of channel segments in HEK cells. (a) Design of fluorophore tagged peptides of various channel segments utilized in FRET 2-hybrid assays. For each peptide, the exact sequence and corresponding locations on the Ca_v1.3 holochannel are highlighted. (b) Immunoblots of HEK293 cell lysates probed with anti-GFP antibody. From left, CFP-NSCaTE at ~33 kDa; YFP-PCI (both WT and LGF₁₅₁₂AAA mutation) at ~42 kDa; YFP-IQ at ~31 kDa; YFP-CI at ~46 kDa; CFP-CaM at ~44 kDa; and YFP at ~27 kDa. (c) Confocal images of HEK293 cells shows smooth expression of various fluorophore-tagged peptides.

Historically, Ca_v channel segments, particularly of the carboxy-terminus, have been viewed as poorly behaving peptides when expressed and purified from bacterial expression systems. Often, such peptides undergo proteolytic cleavage. Here, we used immunoblotting to assess the stability of our fluorophore-tagged channel peptides expressed in HEK293 cells, reflecting experimental conditions in FRET 2-hybrid assay. HEK293 cells expressing fluorophore-tagged channel segments were washed and collected with PBS, centrifuged and resuspended in lysis buffer (20 mM Tris-HCl [pH 7.5], 300 mM sucrose, 1 mM DTT and protease inhibitor cocktail (Roche)). The resuspended solution was then subjected to centrifugation (16,000g × 10 min at 4 °C), yielding cytosolic proteins in the supernatant. The proteins were denatured (95 °C × 1 min) on dilution with TGS buffer (Bio-Rad), and resolved by 5% SDS-PAGE with no CaCl₂ added to the gel. Proteins were transferred to nitrocellulose membranes (Bio-Rad) by cooled transfer (Tris/Glycine transfer buffer/pH 8.3 × 19 h). After blocking, membranes were sequentially incubated with rabbit polyclonal anti-GFP antibody (Abcam, 1:5,000 dilution) and HRP-conjugated secondary antibody (Sigma, 1:2400 dilution). Supplementary Fig. S21 displays protein bands visualized with enhanced chemiluminescence (Pierce ECL, Thermo Scientific). Reassuringly, each peptide appears as a solitary band at the respective sizes (CFP-NSCaTE, ~33 kDa; YFP-PCI WT and mutant, ~42 kDa; YFP-IQ, ~31 kDa; YFP-CI, ~46 kDa; CFP-CaM, ~44 kDa; and YFP, ~27 kDa). Moreover, confocal images of these peptides (Supplementary Fig. S21c) show smooth expression in HEK293 cells, highlighting the robustness of these peptides for FRET 2-hybrid assay.

Supplementary References

61. Tay, L. H. *et al.* Nanodomain Ca^{2+} of Ca^{2+} channels detected by a tethered genetically encoded Ca^{2+} sensor. *Nature Communications* **3**:778, DOI: 10.1038/ncomms1777 (2012).
62. Hill, T. L. *Free energy transduction in biology: the steady-state kinetic and thermodynamic formalism.* (Academic Press, 1977).
63. Martin, S. R., Andersson Teleman, A., Bayley, P. M., Drakenberg, T. & Forsen, S. Kinetics of calcium dissociation from calmodulin and its tryptic fragments. A stopped-flow fluorescence study using Quin 2 reveals a two-domain structure. *Eur J Biochem* **151**, 543-550 (1985).
64. Byrne, M. J., Putkey, J. A., Waxham, M. N. & Kubota, Y. Dissecting cooperative calmodulin binding to CaM kinase II: a detailed stochastic model. *J Comput Neurosci* **27**, 621-638 (2009).
65. Erickson, M. G., Moon, D. L. & Yue, D. T. DsRed as a potential FRET partner with CFP and GFP. *Biophys. J.* **85**, 599-611 (2003).
66. Zal, T. & Gascoigne, N. R. Photobleaching-corrected FRET efficiency imaging of live cells. *Biophys J* **86**, 3923-3939 (2004).
67. Ben Johny, M., Yue, D. N. & Yue, D. T. A novel FRET-based assay reveals 1:1 stoichiometry of apocalmodulin binding across Ca_v and Na_v ion channels (abstr.). *Biophys J* **102**, 125a-126a (2012).
68. Koushik, S. V., Chen, H., Thaler, C., Puhl, H. L., 3rd & Vogel, S. S. Cerulean, Venus, and VenusY67C FRET reference standards. *Biophys J* **91**, L99-L101 (2006).
69. Shah, V. N. *et al.* Calcium-dependent regulation of the voltage-gated sodium channel hH1: intrinsic and extrinsic sensors use a common molecular switch. *Proc Natl Acad Sci U S A* **103**, 3592-3597 (2006).
70. Kim, J. *et al.* Calmodulin mediates Ca^{2+} sensitivity of sodium channels. *J Biol Chem* **279**, 45004-45012 (2004).
71. Zhou, J. *et al.* Feedback inhibition of Ca^{2+} channels by Ca^{2+} depends on a short sequence of the C terminus that does not include the Ca^{2+} - binding function of a motif with similarity to Ca^{2+} - binding domains. *Proc.Natl.Acad.Sci.U.S.A.* **94**, 2301-2305 (1997).
72. Peterson, B. Z. *et al.* Critical determinants of Ca^{2+} -dependent inactivation within an EF-hand motif of L-type Ca^{2+} channels. *Biophysical Journal* **78**, 1906-1920 (2000).
73. Sali, A. & Blundell, T. L. Comparative protein modelling by satisfaction of spatial restraints. *J Mol Biol* **234**, 779-815 (1993).
74. Krishnamurthy, V. M., Estroff, L. A. & Whitesides, G. M. in *Fragment-based approaches in drug discovery* eds W. Jahnke & D.A. Erlanson) 11-53 (Wiley-VCH, 2006).
75. Thompson, R. C. Binding of peptides to elastase: implications for the mechanism of substrate hydrolysis. *Biochemistry* **13**, 5495-5501 (1974).
76. Page, M. I. & Jencks, W. P. Entropic contributions to rate accelerations in enzymic and intramolecular reactions and the chelate effect. *Proc Natl Acad Sci U S A* **68**, 1678-1683 (1971).
77. Alexander, K. A., Cimler, B. M., Meier, K. E. & Storm, D. R. Regulation of calmodulin binding to P-57. A neurospecific calmodulin binding protein. *J Biol Chem* **262**, 6108-6113 (1987).
78. Martin, S. R. & Bayley, P. M. Regulatory implications of a novel mode of interaction of calmodulin with a double IQ-motif target sequence from murine dilute myosin V. *Protein Sci* **11**, 2909-2923 (2002).